

**VALIDATION OF GAMMA RAY SPECTROMETRY PROCESS USED TO
DETERMINE THE RADIONUCLIDES AND RADIOACTIVITY LEVELS IN
DECORATIVE GRANITE COUNTERTOPS.**

KUTULLO FREEDOM MAIBANE

A Thesis presented in fulfilment of the requirements for the degree of
Master of Sciences in the Department of Physics at the University of the
Western Cape, South Africa.

*The financial assistance of the National Research Foundation (NRF) towards this research is
hereby acknowledged. Opinions expressed and conclusions arrived at, are those of the author and
are not necessarily to be attributed to the NRF.*



Supervisors:

Dr P. P. Maleka,

Department of Nuclear Physics,
iThemba LABS.

Prof R. Lindsay,

Department of Physics,
University of the Western Cape.

2016

DECLARATION

I, the undersigned, declare that the work contained in this thesis, **Validation of gamma ray spectrometry process used to determine the radionuclides and radioactivity levels in decorative granite countertops**, is my original work and has not previously in its entirety or part been submitted at any University for a degree.

KUTULLO FREEDOM MAIBANE

Date:

Signature:



UNIVERSITY *of the*
WESTERN CAPE

KEYWORDS

- Gamma radiation
- Gamma-ray spectrometry
- HPGe gamma-ray detector
- Granite countertops
- Detection efficiency
- Density effect
- Coincidence summing
- Activity concentration
- Secular equilibrium
- Radiological hazards



UNIVERSITY *of the*
WESTERN CAPE

Validation of gamma ray spectrometry process used to determine the radionuclides and radioactivity levels in decorative granite countertops

KUTULLO FREEDOM MAIBANE

Department of Physics, University of the Western Cape, Private Bag X17, Bellville, South Africa.

ABSTRACT

Humans are continuously exposed to low level of ionizing radiation, sources include soil, medical treatment and as well as radiation emissions from natural materials like granite rocks. The radiation levels present in these granite rocks varies depending on the mineral properties and their origins. The aim of this study is to assess the radiation levels in various granite countertops available commercially in South Africa. The radiation levels present in the granite countertop samples were determined using the available low-background HPGe gamma-ray detector system at iThemba LABS. Initially, the study focused on the optimisation of the photopeak efficiencies of the detector system to match the samples, i.e. 'box-like' geometry as opposed to the traditionally used Marinelli beaker geometry. A soil sample with known activity (^{238}U series: 940 ± 30 Bq/kg; ^{232}Th series: 660 ± 20 Bq/kg and ^{40}K : 153 ± 8 Bq/kg) determined with Marinelli beaker geometry was used to prepare an artificial reference material for the new box geometry.

The new-efficiency parameters determined were used to calculate the activity concentrations present in the 5 granite countertop samples. The range of activity concentration levels determined in all granite counter samples are 3 – 610 Bq/kg, 50 – 170 Bq/kg and 1400 – 2000 Bq/kg for ^{238}U , ^{232}Th and ^{40}K , respectively. These levels are higher than the world mean values reported by UNSCEAR of 40 Bq/kg, 40 Bq/kg and 370 Bq/kg for ^{238}U (2 samples), ^{232}Th (4 samples) and ^{40}K (all samples), respectively. The estimated absorbed dose rates range from 194(4) to 790(30) nGy/h. The radionuclides ^{226}Ra , ^{232}Th and ^{40}K contributes approximately 44%, 52% and 4%, respectively, of the total absorbed dose rate in all granite countertop samples.

ACKNOWLEDGEMENTS

This thesis would not have been possible without the support of many people. I am abundantly grateful for their support and I would like to express my deepest gratitude to the following people:

Dr P. P. Maleka, supervisor at iThemba LABS, special thanks for his guidance, encouragement, active involvement and support. He has outstanding, cut above the rest.

Prof R. Lindsay, supervisor at UWC, massive thanks for his advice and supervision into scientific research. He has been an excellent supervisor and a teacher, patience and motivating.

Mr S. Tshingana, for his contribution towards the preparation and measurement of the samples, and for technical support.

Dr Joash Ongori, many thanks for his support, advice, guidance, suggestions and motivation during this study. He has indeed been a wonderful friend and a mentor.

Dr R. Nchodu, HOD for Department of Nuclear Physics at iThemba LABS, for his support and making Environmental Radioactivity Laboratory available throughout the study at all times. I am deeply indebted and forever grateful.

Foremost, I would like to express my sincere gratitude to the former Mr Andrew Esau and the current Mr Masimba Paradza course co-ordinators for the support of my study, for their patience, motivation, enthusiasm and immense knowledge.

iThemba LABS, for Environmental Physics Resource Material, UWC Department of Physics, mainly office of secretary for resolving administration challenges, and NRF, extra special thanks for financial support.

A book like this depends greatly on the research material available and I am particularly grateful to the UWC and iThemba LABS Research Libraries.

Fellow MANUS/MatSci postgraduate students, namely: Mathews Makhubela, Vusimuzi Masondo, Tshepo Shibambu, Immanuel Mulaudzi and Albert Ramashia for their advices and encouragements.

My family and friends, my beloved daughter, Bonolo Maibane, who gives me courage and strength and I'm deeply sorry for the time we spent apart, deserve endless thanks for their patience and support.

In Loving Memory of my near and dear friend Junior Maila. Always on my mind and forever in my heart. Ecclesiastes 3:1 "To everything there is a season, and a time to every purpose under the heaven".

Finally, I would like to express my sincere gratitude to all personnel who have engaged in this study and taking their time to make this study successful.

Table of Contents

Chapter 1.....	1
INTRODUCTION.....	1
1.1 Overview	1
1.2 Aims of the study	4
1.3 Scope of this Dissertation	5
Chapter 2.....	6
NUCLEAR DECAYS AND GAMMA DETECTION.....	6
2.1 Radioactive decay.....	6
2.2 Interaction of γ radiation with matter.....	8
2.3 Gamma-ray attenuation.....	11
2.4 Natural γ radiation	12
2.4.1 ^{40}K	12
2.4.2 The natural decay series of ^{232}Th and ^{238}U	13
2.5 Detectors.....	17
2.5.1 General characteristics of γ detectors	17
Chapter 3.....	21
METHODOLOGY	21
3.1 HPGe Detector system.....	21
3.1.1 Instrumentation.....	21
3.1.2 Spectrometer Calibration	24
3.1.3 Marinelli beaker geometry	26
3.1.4 Granite countertops geometry	32
3.1.5 KCl mass and activity relation	33
3.2 Sample Preparation.....	36
3.2.1 Sand Sample.....	37
3.2.2 Granite Countertops.....	38
3.2.3 KCl Sample	41
3.3 Data analysis.....	41
3.3.1 Activity concentration.....	42
3.3.2 Coincidence summing	45
Chapter 4.....	50
RESULTS AND DISCUSSION.....	50
4.1 ^{232}Th and ^{238}U	50
4.1.1 ^{232}Th	50
4.1.2 ^{238}U	54

4.2	Testing secular equilibrium.....	57
4.3	Correlation between $^{238}\text{U}/^{232}\text{Th}$ and ^{238}U	59
4.4	Comparison of ^{238}U , ^{232}Th and ^{40}K	60
4.5	Assessment of radiation dose.....	64
4.5.1	Radium equivalent activity.....	64
4.5.2	External hazard index	65
4.5.3	Internal hazard index.....	65
4.5.4	Absorbed dose rate	66
4.5.5	Effective dose.....	66
4.6	Assessment of radiological hazards.....	67
Chapter 5.....		69
SUMMARY AND OUTLOOK		69
5.1	Introduction.....	69
5.2	Summary	69
5.3	Outlook.....	72
APPENDICES.....		74
A.	References	74
B.	Certified reference	80
C.	Spectrum analysis	82
D.	List of symbols.....	84



List of figures

Figure 2.1: The relative importance of the three major interaction processes between γ radiation and matter. The solid lines indicate the value of Z and E_γ for which the cross sections for two neighbouring effects are equal [Knoll 2010].	8
Figure 2.2: Diagrammatic representation of Compton scattering. The momentum of the incoming gamma-ray is shared between the scattered gamma-ray and a recoil electron, and the scatter angles are symbolized by ϑ and ϕ respectively.	9
Figure 2.3: Angular distribution of Compton scattered gamma radiation. Each contour line gives the probable scatter angle ϑ for the denoted incoming E_γ . Figure from [Tavernier, 2010].	10
Figure 2.4: Diagrammatic representation of the decay of ^{40}K showing two decay modes, β^- decay to ^{40}Ca (89.3%) and electron capture to an excited state of ^{40}Ar (10.7%) [Firestone, 1996].	13
Figure 2.5: Diagrammatic representation of the decay series of the natural radionuclide ^{232}Th . The initial and final nuclides are indicated by a bold square. The downward arrows represent α radiation and the diagonal arrows represent β^- radiation. Each box also indicates $t_{1/2}$ (a for years, m for months, d for days, h for hours and s for seconds). The highlighted squares indicate the prominent γ -ray emitters that are measured in this study [Firestone, 1996].	14
Figure 2.6: Diagrammatic representation of the decay series of the natural radionuclide ^{238}U . The initial and final nuclides are indicated by a bold square. The downward arrows represent α radiation and the diagonal arrows represent β^- radiation. Each box also indicates $t_{1/2}$ (a for years, m for months, d for days, h for hours and s for seconds). The highlighted squares indicate the prominent γ -ray emitters that are measured in this study [Firestone, 1996]. ^{234}Pa is used but has a weak γ -ray.	16
Figure 2.7: Electron energy levels in various materials. The band-gap literally represents the energy difference between the levels of the two bands.	18
Figure 2.8: A spectrum plotted in comparison between Ge semiconductor detector and NaI scintillation detector using ^{60}Co source [Leo, 1987].	19
Figure 3.1: Photographs of (a) the ERL HPGe detector system, (b) Marinelli beakers used for samples and (c) the top view showing Marinelli beaker inside the castle.	22
Figure 3.2: Block diagram showing how the components of the high resolution ERL HPGe gamma ray spectrometry experimental system interlink.	23
Figure 3.3: Peak energy as a function of channel number.	25
Figure 3.4: MCNPX simulated (solid line) and measured (points) full-energy peak (FEP) detection efficiencies for the ERL HPGe detector system in the 1.3 L screw-top Marinelli beaker geometry filled to the 1 L mark by [Maleka, 2012].	27
Figure 3.5: The photo-peak spectrum from NMISA liquid standard showing the energies of the gamma-ray lines.	29
Figure 3.6: Absolute efficiency curve simulated using the standard a liquid source. The points are associated with the gamma-ray energies from ^{152}Eu , ^{137}Cs and ^{60}Co in the CSIR measurement.	31
Figure 3.7: Absolute efficiency curve simulated using the standard liquid source. The points are associated with the gamma-ray energies from ^{152}Eu , ^{137}Cs and ^{60}Co in the NMISA source.	31
Figure 3.8: Efficiency curve deduced from the prepared reference sand material.	33
Figure 3.9: A spectrum of the count rate (cps) versus energy (keV) showing a 1461 (keV) photo-peak from ^{40}K .	35
Figure 3.10: The Marinelli geometry used for measurement and a cross-section view indicating the dimensions.	37

Figure 3.11: A typical photograph of a sealed Marinelli beaker with the soil sample inside.	38
Figure 3.12: A photograph showing the granite countertops on top of each other, namely; Namib Green, Santa Cecelia, African Red, Indiana Dakota and Golden Beach in that order from top to bottom.	40
Figure 3.13: A photograph of the soil sample in a new measuring geometry on a mass scale sealed using tape.	40
Figure 3.14: Photographs showing the ERL EcoTherm oven (left-side) used in this study to dry the samples and the KCl sample in a container (right-side).	41
Figure 3.15: Typical measured spectra (Santa Cecelia, Namib Green, African Red, Golden Beach and Indiana Dakota) superimposed over a background spectrum to indicate relative count rates of the samples to the environmental background.	43
Figure 3.16: This figure depicts the simplified decay scheme of ^{152}Eu . The gamma-rays and the branching ratios are extracted from [Firestone, 1996].....	46
Figure 3.17: Efficiency calibration curve following Maleka's (2012) efficiency fit for 1 L Marinelli beaker geometry and the measured efficiencies from different standard sources for ^{152}Eu measured with 1 L Marinelli beaker geometry. The effect of coincidence summing is clear for several of the peaks.	48
Figure 3.18: Figure showing the calculated activity concentration (Bq/L) as a function of Energy (keV) for the ^{152}Eu radionuclide found in reference sources from CSIR. Unc+ and Unc- indicate 1σ deviation from the expected values.	49
Figure 3.19: Figure showing the calculated activity concentration (Bq/L) as a function of Energy (keV) for the ^{152}Eu radionuclide found in reference sources from NMISA. Unc+ and Unc- indicate 1σ deviation from the expected values.	49
Figure 4.1: Activity levels of ^{232}Th as measured from the AR sample. These activity levels were calculated using individual γ lines from ^{228}Ac , ^{212}Pb , ^{212}Bi and ^{208}Tl in the ^{232}Th decay chain. The weighted mean is indicated by the line.	51
Figure 4.2: Activity levels of ^{232}Th as measured from the GB sample. These activity levels were calculated using individual γ lines from ^{228}Ac , ^{212}Pb , ^{212}Bi and ^{208}Tl in ^{232}Th decay chain. The weighted mean is indicated by the line.	51
Figure 4.3: Activity levels of ^{232}Th as measured from the NG sample. These activity levels were calculated using individual γ lines from ^{228}Ac , ^{212}Pb , ^{212}Bi and ^{208}Tl in ^{232}Th decay chain. The weighted mean is indicated by the line.	52
Figure 4.4: Activity levels of ^{232}Th as measured from the SC sample. These activity levels were calculated using individual γ lines from ^{228}Ac , ^{212}Pb , ^{212}Bi and ^{208}Tl in ^{232}Th decay chain. The weighted mean is indicated by the line.	52
Figure 4.5: Activity levels of ^{232}Th as measured from the ID sample. These activity levels were calculated using individual γ lines from ^{228}Ac , ^{212}Pb , ^{212}Bi and ^{208}Tl in ^{232}Th decay chain. The weighted mean is indicated by the line.	53
Figure 4.6: Activity levels of ^{238}U as measured from the AR sample. These activity levels were calculated using individual γ lines from ^{234}Pa , ^{226}Ra , ^{214}Pb , and ^{214}Bi in ^{238}U decay chain. The weighted mean is indicated by the line.	54
Figure 4.7: Activity levels of ^{238}U as measured from the GB sample. These activity levels were calculated using individual γ lines from ^{234}Pa , ^{226}Ra , ^{214}Pb , and ^{214}Bi in ^{238}U decay chain. The weighted mean is indicated by the line.	55
Figure 4.8: Activity levels of ^{238}U as measured from the NG sample. These activity levels were calculated using individual γ lines from ^{234}Pa , ^{226}Ra , ^{214}Pb , and ^{214}Bi in ^{238}U decay chain. The weighted mean is indicated by the line.	55

Figure 4.9: Activity levels of ^{238}U as measured from the SC sample. These activity levels were calculated using individual γ lines from ^{234}Pa , ^{226}Ra , ^{214}Pb , and ^{214}Bi in ^{238}U decay chain. The weighted mean is indicated by the line. 56

Figure 4.10: Activity concentration (Bq/kg) of interest radionuclides from ^{238}U before radon escape and after radon escape in the SC sample..... 58

Figure 4.11: Activity concentration (Bq/kg) of radionuclides from the ^{238}U decay series before radon escape and after radon escape in the AR sample..... 59

Figure 4.12: A linear function fitted between $^{238}\text{U}/^{232}\text{Th}$ and ^{238}U (Bq/kg) that indicates a linear relationship..... 60

Figure 4.13: Comparison of ^{238}U activity concentration (Bq/kg) of various granite countertop samples..... 61

Figure 4.14: Comparison of ^{232}Th activity concentration (Bq/kg) of various granite countertop samples..... 62

Figure 4.15: Comparison of ^{40}K activity concentration (Bq/kg) of various granite countertop samples..... 62

Figure 5.1: Components of the worldwide annual average individual radiation dose. The pie chart shows the annual average dose to the representative individual from the different radiation sources [McColl, 2015]. 71



List of tables

Table 3.1: Summary of the electronic components and equipment used for gamma-ray spectroscopy in this study.	22
Table 3.2: Activity concentrations of the certified reference materials CSIR and NMISA at the time they were characterized by the supplier. (All uncertainties are at the 1σ level).	27
Table 3.3: Current activity concentrations of radionuclides in the certified reference materials CSIR and NMISA at the time of measurement. (All uncertainties are at the 1σ level)	28
Table 3.4: Gamma-ray lines and associated branching ratios (Firestone, 1996) for the given radionuclides present in the liquid standard sources.	29
Table 3.5: Gamma-ray lines in the ^{238}U -series, ^{232}Th -series and ^{40}K with absolute emission probabilities extracted from [Firestone, 1996] and the branching ratio for ^{226}Ra was adopted from [Newman, 2008].	36
Table 3.6: Granite countertop samples physical properties; dimensions (cm), mass (kg) and their calculated bulk densities (g cm^{-3}).	39
Table 3.7: Z scores commonly used confidence interval [Kirkup, 1994].	44
Table 3.8: Calculated efficiencies of the coincidence summing from different standard sources for ^{152}Eu measured with 1 L Marinelli beaker geometry.	47
Table 4.1: Average thorium activity concentration available in each granite countertop sample, with respective low and high activity levels measured. The uncertainties indicated are at the 1σ level.	53
Table 4.2: Average uranium activity concentration in each granite countertop sample, with respective low and high activity levels measured.	54
Table 4.3: Activity concentration (Bq/kg) of radionuclides from ^{238}U series before radon decay and after radon decay.	57
Table 4.4: Average activity concentrations for the five granite countertop samples	61
Table 4.5: Average values of the activity concentrations of ^{226}Ra , ^{232}Th and ^{40}K in granite samples from the different countries and earth crust.	64
Table 4.6: The values of the R_{eq} , the H_{ex} , the H_{in} and the absorbed dose rate (D) evaluated for the samples of the granite countertops.	66
Table 4.7: Estimated indoor annual effective dose E_{D} (mSv), calculated from the corresponding absorbed dose rate D (nGy/h).	67

Chapter 1

INTRODUCTION

1.1 Overview

Radiation and radioactivity in the environment have natural and anthropogenic sources. Exposure to natural radiation represents the most significant fraction of the total exposure to radiation in the environment [Tso and Leung, 2000; UNSCEAR, 2008]. Radioactivity is hazardous by its ionizing effect on human cells, for instance, its potential to discharge electrons out of orbit by the process of ionization. The ionizing effect depends on a complex series of actions that is determined by the charge, type of radiation, and energy. Many factors such as free-radical mutagenic DNA damage, which is the most common dangerous biological effect, may result in biological effects such as DNA repair deficiency [Cooke, 2003; Lobo, 2010].

Radiation is a natural phenomenon to which humans have always been exposed. Natural radioactive substances on earth such as rocks and minerals, as well as cosmic rays and radioactive materials in the earth's crust are responsible for what is known as background radiation. Radiation penetrates and damages cells in the human body, including DNA molecules. The human body repairs damaged cells, however occasionally cells are not repaired, and they eventually do not survive.

Background radiation is emitted from both anthropogenic and natural sources. Humans are constantly exposed or irradiated by internal and external sources. The source of internal exposure could be in the food and water that is ingested and the air breathed, but consequently this class of radiation will be neglected. The external radiation comes from the atmosphere due to cosmic radiation, and our home planet Earth is also the source of some of the naturally occurring radiation. In the Earth crust, radioactivity is mainly incorporated in mineral crystals present in rocks and sediments. The radionuclide concentrations depend on the mineral properties and their origin. Human activities like, nuclear power plants used to generate electricity (e.g. Koeberg nuclear power station in South Africa) and other medical procedures that use radionuclides (e.g.

radionuclides produced at iThemba LABS) and X-rays, contribute to the radiation that is present in our environment.

Humans may also be exposed to radiation within the homes they live in such as radiation from the soil beneath the floor, as well as radiation from the building material, for example granite countertops. Granite is a naturally occurring igneous rock, which is formed when a molten rock cools down. It is extracted and processed to manufacture commercial products such as countertops. The amount of radiation emitted from granite countertops can differ depending on the amount of natural radionuclides (^{238}U , ^{232}Th and ^{40}K) present in the sample [Llope, 2011] which depends on the location of the rock where it was found. Diverse granite samples contains varying concentrations of natural uranium (that is about 99.3% ^{238}U) [Llope, 2011] that subsequently results in the production of radon (^{222}Rn) gas and emission of alpha particles. The largest fraction of the exposure comes from natural radiation, radon and its associates, external radiation e.g. cosmic and terrestrial radiation make up virtually 2/3 of the total exposure [ERSSFOPH, 2005]. Granite countertops used in household, kitchens and bathrooms, may contribute significantly to indoor radon levels and gamma-radiation.

Granites are extremely durable and scratch resistant; granites are mechanically polished to a high gloss finish due to its solidity. Their variety of colour, unique heat and scratch resistant properties makes them ideal for use as work-surfaces, flooring etc. Typical granites are chemically composed of 75% silica, 12% aluminium, less than 5% potassium oxide, less than 5% soda and many other elements in smaller quantities. In terms of natural radioactivity, some granites exhibit a greatly enhanced elemental concentration of uranium and thorium compared to the very low abundance of these elements in the mantle and the crust of the Earth [Tzortzis, 2003]. This enhancement has led to worries about possible risks due to gamma-radiation from granite as building materials.

Mohamed (2015) studied 60 samples of different marble and granite tiles used as building materials, from local and foreign origins, collected from different factories in the Al-Madinah Al-Munawarah region of Saudi Arabia. They concluded that the use of these marble and granite samples under investigation in the construction of dwellings is considered to be safe for inhabitants. In order of increasing activity for marble, the preference is 1st Omani marble, then Turkish marble, and finally Egyptian marble. For

granite, the preference is 1st Chinese granite, then Saudi granite, and finally Indian granite. Recently, there has been a great increase in the utilization of granite tiles as kitchen-counter, and vanity-tops and flooring tiles for home interiors. As a result, prominent efforts have been made to determine the radioactivity in granite tiles used in various countries [Myatt, 2015; Anjos, 2011; Llope, 2011; Righi, 2006; Tzortzis, 2003]. Several studies [McColl, 2015; Pacheco-Torgal, 2012; BEIR VI, 1999] have already demonstrated that indoor exposure to radon and its decay products is an important cause of lung cancer.

As stated by the World Health Organization [WHO, 2009] radon constitutes the second most important cause of lung cancer in the general population. Moreover, lung cancer spread quickly based on the accumulated inhaled dose. Following WHO (2009), there is no lower radon level below which the risk from exposure disappears. Recent studies carried out in Portugal show that of the 8514 lung cancer deaths observed, from 18% to 28% could be associated with indoor radon exposure [Velooso, 2012]. However, some studies show that most of the public seems to regard the health risks involved in radon exposure as being negligible. For this reason, most countries do not require the use of protection measures for buildings located in radon-affected areas.

Radon gas (^{222}Rn) is a natural constituent of the environment and a risk factor for lung cancer. We are exposed to radon as a result of radioactive decay of radium (^{226}Ra) in stone and soil [Allen, 2009]. Radon is an inert noble gas, of which there are three naturally occurring radioactive isotopes, namely ^{219}Rn (half-life = 3.96 s), ^{220}Rn (half-life = 55.6 s) and ^{222}Rn (half-life = 3.82 days). These isotopes arise from the decay series of ^{235}U , ^{232}Th and ^{238}U , respectively. Radon is relatively soluble in water and can migrate from one place to other either by soil air or travel with underground water [Talha, 2009]. Radon decays by alpha emission, and the progeny can couple with dust particles which continue to exist in air. These radioactive dust particles can be inhaled, thereby causing internal contamination in humans and animals, causing irradiation of the bronchi lining in the lung with alpha particles with a potential risk of causing lung cancer [Ongori, 2013; BEIR VI, 1999].

Until very recently it was normally accepted that only 5% of the indoor radon concentration was due to building materials [Lao, 1990]. Several authors Pavlidou et al. [Pavlidou, 2006] state that the majority of granite rocks have low radon exhalation

rates. In the paper “Indoor radon: An overview on a perennial problem” by Pacheco-Torgal (2015), the author reviews the literature on radon as a source of indoor air contamination.

In the past, it was often accepted that only radon levels above 400 Bq/m³ could be a source of concern. Nevertheless, latest studies show that this threshold is far from being safe. Dinua (2009) studied 90 households in Spain with the highest radon concentration of 366 Bq/m³, stating that many cancer related deaths occurred in that area. In this study, the radioactivity levels of ²³⁸U, ²³²Th and ⁴⁰K in selected granite countertops available in South Africa are studied. Essential radiological hazards caused from the utilization of granite materials in South African households were evaluated.

1.2 Aims of the study

We are living in an inherently radioactive world, where humans are constantly exposed to a radioactive environment. Ionizing radiation is environmentally unfriendly because it can alter the chemical composition of many things, which can affect the chemistry of the living organisms. Low level ionizing radiation comes from soil, cosmic rays, and internal sources. Natural rocks such as granite are commonly used in residential settings as countertops in kitchens and bathrooms [Shapiro, 2002; Myatt, 2009; Allen, 2009].

The main aim of this study was to assess the radiation levels of various types of granite countertops available commercially in South Africa. A lead shielded HPGe γ -ray detection system, coupled with suitable electronics is available at iThemba LABS. This high resolution HPGe detector is mainly used with Marinelli beaker and pill-bottle geometries. In order to measure natural γ -radiation precisely and accurately, a calibration standard source of the same geometry as the sample to be counted is required. For the purpose of this study, in order to achieve this aim, the following evaluations were done:

- Efficiency calibrations of the detector system for the granite sample geometry; i.e. geometry and density effects. The density effect also validates the self-absorption of gamma-rays in the sample matrix.

- Validation of the efficiency of the detector system by investigating the effect of coincidence summing using certified reference sources containing the ^{152}Eu radionuclide, only for Marinelli beaker geometry.
- Assessment of radiological hazards from the measured activity concentration levels of the 3 main primordial radionuclides (^{238}U , ^{232}Th and ^{40}K) in the granite countertop samples.

1.3 Scope of this Dissertation

The main focus of this study is the determination of radioactivity levels present in granite countertops using a HPGe gamma-ray detector system. To describe the processes involved in the gamma-ray spectrometry method, chapter 2 will introduce basic practical understanding of interaction of γ -radiation with matter and describe the types of detectors that could be used to study these processes.

Chapter 3 will explore the setup of the available HPGe γ -ray detector system, sample preparations, energy and efficiency calibrations for Marinelli and granite countertops geometries. In addition, the granite countertops geometric experimental efficiency calibration is compared to a Marinelli beaker geometry efficiency calibration from a simulation study. Furthermore, the technique that is used to determine activity concentrations from measured γ -spectra is discussed in this chapter and the test results to validate the calculated efficiency parameters for the γ -ray detector using a ^{152}Eu standard source are then summarised. Chapter 4 will present the results and discussions of ^{238}U , ^{232}Th and ^{40}K radionuclides activity concentrations present in the samples. Moreover, the method used to test for secular equilibrium as well as the techniques used to evaluate the radiological parameters will be presented. Chapter 5 will provide a summary of the radioactivity distribution status of all samples. Furthermore, recommendations for future work will be given.

Chapter 2

NUCLEAR DECAYS AND GAMMA DETECTION

Radioactive decay, also known as nuclear decay or radioactivity, is encountered when an unstable nucleus decays to a daughter nucleus which may be another unstable nucleus [Leo, 1987]. A material that spontaneously emits such radiation which includes alpha particles, beta particles, gamma-rays and conversion electrons is considered radioactive.

2.1 Radioactive decay

After the discovery of radioactivity in 1896 by A. H. Becquerel [Allisy, 1996], the science of radioactivity has grown significantly. Radionuclides are the sources of radioactivity and emit nuclear radiations. Radiation can arise from natural radionuclides but it can also be from manmade sources. All matter surrounding us is made up of atoms; the atoms consist of a combination of a nucleus containing most of the mass, and of electrons [Tavernier, 2010]. Protons (p), which have a net positive charge and neutrons (n) which are neutral, are collectively referred to as nucleons (p,n). Nucleons (p,n) interact with each other via the nuclear force and due to Coulomb force protons repel each other. These forces cause the binding energy of the nucleus which results in the difference for the mass of the nucleus to be 1% smaller than the sum of the masses of the constituent neutrons and protons. Naturally, only certain combination of the number of neutrons (N) and the number of protons (Z) lead to stable nuclei. Unstable nuclei mainly decay by alpha (α), beta (β) and gamma (γ) decay, depending on the nucleus [Krane, 1988; Knoll, 2000].

In α decay, a heavy nucleus loses four nucleons through the emission of an α particle, ${}^4\text{He}$ nucleus. Alpha particles are positively charged and are emitted from natural elements such as uranium and radium (see example in Equation 2.1 below), as well as from anthropogenic radiation. Alpha radiation can penetrate the surface of the skin but be stopped by a simple sheet of paper.



In β decay, an unstable nucleus can de-excite to a lower state by converting a neutron (see eq. 2.2) into a proton or vice versa, the positron and neutrino (or electron and its antineutrino) leave the nucleus.



β radiation consists of electrons which can pass through 1-2 cm of water; it can be stopped by a sheet of aluminium a few millimetres thick. After β decay or α emission, the nucleus is often not in its ground state [Knoll, 2010]; the transition between the excited levels and the ground state can give rise to emission of γ -rays [Leo, 1987]. Gamma (γ) radiation, the highly energetic electromagnetic radiation from nuclei can pass through matter and thick layer (> 10 cm) of concrete or lead needs to be used to stop it.

The energy of the emitted α and γ radiation is discrete and well defined, but β decay is accompanied by the emission of an undetected (anti-) neutrino, thus the energy spectrum of the emitted β particles is continuous [Krane, 1988; Knoll, 2010].

Activity, A [Bq] of radioisotope source is defined as the rate of decay, fundamental law of radioactivity:

$$A \equiv \left. \frac{dN}{dt} \right|_{decay} = -\lambda N \quad (2.3)$$

where λ is the decay constant in s^{-1} and N is the number of nuclei, and the minus sign shows that N is decreasing with time (t). The decay rate, λN gives the activity of the radionuclide. The higher both number of unstable nuclei and decay constant, the higher the activity. The number of radioactive nuclei N can be found by solving Equation 2.3 to give:

$$N(t) = N_0 e^{-\lambda t} \quad (2.4)$$

with N_0 the number of radioactive nuclei at t_0 . An important relation between the decay constant and half-life, $t_{1/2}$ is derived by substituting $N = N_0/2$ into equation (2.4) and λ can be expressed as:

$$\lambda = \frac{\ln 2}{t_{1/2}} \quad (2.5)$$

The activity concentration of a sample is defined as the activity per unit mass [Bq/kg]. The half-life of any radioactive nuclide refers to the time required for any amount of it to decay to one-half of its original activity [Lapp, 1972].

2.2 Interaction of γ radiation with matter

In the following discussion, we regard a segment of matter e.g. detector or geological matrix, in which γ -ray emitting radionuclides are integrated. The material has an atomic number (Z) and density (ρ) [Hendricks, 2003], whilst a substantial number of possible interaction mechanisms are known for γ -rays in matter. Three types of interaction (predominantly through interaction with an electron) play an important role in radiation measurement [Evans, 1955; Krane, 1988; Knoll, 2000]; these three interaction processes are described below in the order of increasing dominant energy. Figure 2.1 shows the energy dependence of the interaction processes with the Z values of the absorber materials.

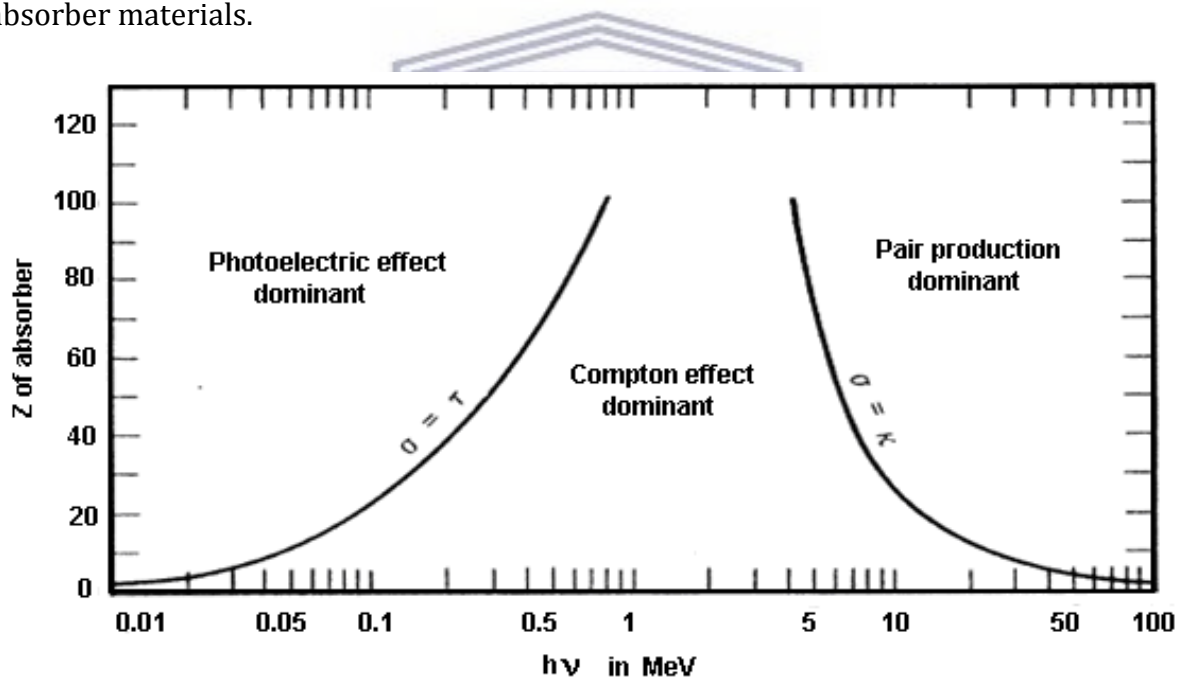


Figure 2.1: The relative importance of the three major interaction processes between γ radiation and matter. The solid lines indicate the value of Z and E_γ for which the cross sections for two neighbouring effects are equal [Knoll 2010].

- **Photoelectric absorption**

In the photoelectric absorption process, a γ -ray undergoes an interaction with a bound electron, and all the γ -ray energy completely disappears, the photoelectron appears with an energy given by [Debertin, 1988; Gilmore, 2008]:

$$E_{e^-} = E_\gamma - E_b \quad (2.6)$$

where E_b is the binding energy of the struck electron. It is quite difficult to describe the analytical expression of the cross section for the entire range of γ -ray energies and atomic numbers. The overall trend for the cross section per unit mass for photoelectric absorption σ_τ [m^2/kg], can be approximated by:

$$\sigma_\tau = \text{constant} \times \frac{Z^n}{E_\gamma^{3.5}} \quad (2.7)$$

with Z the atomic number and $n \sim 3-4$, depending on the γ -ray energy. From the expression above it can be deduced that; the cross section for photoelectric absorption strongly increases as the γ -ray energy decreases. Thus the process is dominant at low energy range and high Z materials are the most essential γ ray absorbers, if photoelectric absorption is the dominant effect [Knoll, 2010].

- **Compton scattering**

Compton scattering is the inelastic scattering of a gamma-ray by a free charged particle, usually an electron, illustrated in Figure 2.2 below. Consequently a portion of the gamma-ray energy is transferred to an electron, called Compton Scattering.

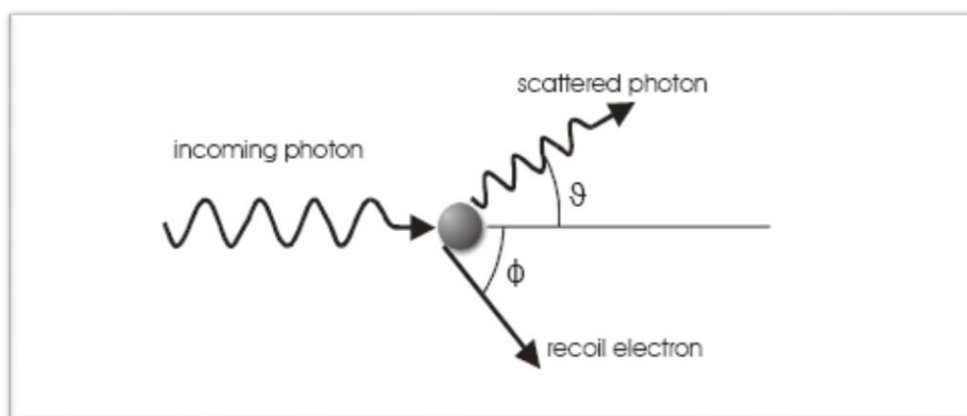


Figure 2.2: Diagrammatic representation of Compton scattering. The momentum of the incoming gamma-ray is shared between the scattered gamma-ray and a recoil electron, and the scatter angles are symbolized by ϑ and ϕ respectively.

Because all angles of scattering are possible, the energy transferred to the electron can vary from zero to a large fraction of γ -ray energy (as shown in Figure 2.3). The expression that relates the energy transfer and the scattering angle for any given interaction can be derived by solving simultaneous equations for the conservation of energy and momentum [Debertin, 1988; Gilmore, 2008].

$$h\nu' = \frac{E_\gamma}{1 + \frac{E_\gamma}{m_0c^2}(1-\cos\theta)} \quad (2.8)$$

where m_0c^2 is the rest mass energy of the electron [0.511 MeV]. The cross section for the Compton scattering, σ_c [m^2/kg], is given by

$$\sigma_c = \text{constant} \times E_\gamma^{-1} \quad (2.9)$$

This means the probability for the Compton scattering is independent of the atomic number of the material through which the γ -ray travels.

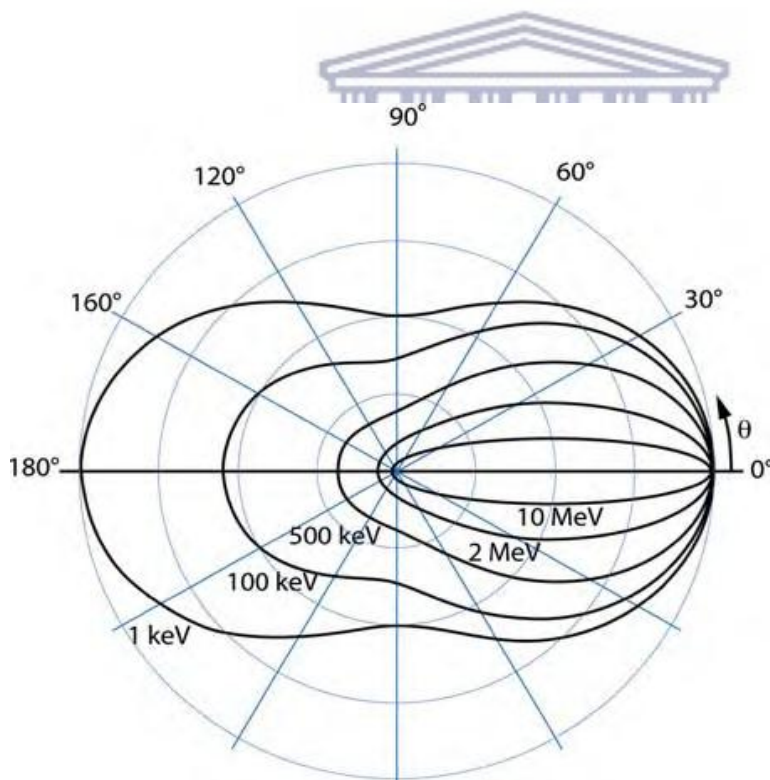


Figure 2.3: Angular distribution of Compton scattered gamma radiation. Each contour line gives the probable scatter angle ϑ for the denoted incoming E_γ . Figure from [Tavernier, 2010].

The angular distribution of the scattered gamma-rays is described by the Klein-Nishina formula (from Quantum Electrodynamics) for the differential scattering cross section $d\sigma_c/d\Omega$ [Knoll, 2010]:

$$d\sigma_c/d\Omega = Zr_0^2 \left(\frac{1}{1 + \alpha(1 - \cos\theta)} \right)^2 \left(\frac{1 + \cos^2\theta}{2} \right) \left(1 + \frac{\alpha^2(1 - \cos\theta)^2}{(1 + \cos^2\theta)[1 + \alpha(1 - \cos\theta)]} \right) \quad (2.10)$$

with $\alpha \equiv E_\gamma/m_0c^2$ and $r_0 = 2.8 \times 10^{-15}m$ is the Classical electron radius.

- **Pair production**

The process of pair production involves the transformation of a γ -ray into an electron positron pair. The γ -ray energy must be greater than twice the energy corresponding to the rest mass of an electron i.e. 1.022 MeV. The excess energy $E_\gamma - 2 \cdot m_0c^2$ is shared between the two particles as kinetic energy. Both particles electron and positron will be slowed down in material, allowing the positron to react with an electron and finally annihilate. Two annihilation γ -rays are normally formed as secondary products of the interaction. The pair production cross section σ_k [m²/kg], is given by

$$\sigma_k = \text{constant} \times Z \times E_\gamma^2 \quad (2.11)$$

The pair production cross section σ_k [m²/kg] increases with gamma-ray energy (E_γ) as well as atomic number Z.

2.3 Gamma-ray attenuation

The term attenuation refers to the gamma-rays that have either been absorbed or scattered in the layer [Debertin, 1988]. By summing up all individual cross sections, to give the total probability for a gamma-ray interaction in matter:

$$\sigma = \sigma_\tau + Z\sigma_c + \sigma_k \quad (2.12)$$

The Compton cross section is multiplied by Z to account for the Z electrons per atom [Leo, 1987]. The total linear attenuation coefficient is given by:

$$\mu = N\sigma = \sigma(N_A\rho/A) \quad (2.13)$$

where N (atoms/cm³) is the density of atoms, N_A (atoms/mol) is Avogadro's number, ρ (g/cm³) is density of the material, and A (g/mol) is the molecular weight. Consider a

beam of gamma-rays entering a layer of thickness x that is perpendicular to the surface, then the number of the transmitted gamma-rays I is given in terms of the original beam intensity I_0 by, (see Appendix D);

$$I/I_0 = e^{-\mu x} \quad (2.14)$$

Equation (2.14) relates the intensity of gamma-rays at a specified energy after attenuation, I , to that without attenuation at the same energy, I_0 . This relationship is only valid under 'good geometry' conditions with a thin absorber and collimated gamma-ray source. Under the open conditions the equation fails because of scattering from the absorber [Gilmore, 2008]. Equation (2.14) gives:

$$\ln I = \ln I_0 - \mu x \quad (2.15)$$

The Equation (2.15) implies that if a graph of $\ln(I_0/I)$ is plotted against the thickness (x) of the sample of interest; a straight line is obtained, where the slope is the attenuation coefficient of that sample.

2.4 Natural γ radiation

Radioactive decay series are often encountered in which an unstable nucleus decays to a daughter nucleus which will disintegrate to another unstable nucleus et cetera [Leo, 1987]. Most natural radionuclides that are observed which are short to moderately lived nuclides, such as ^3H , ^7Be and ^{14}C , are continuously formed under the influence of cosmic radiation, but some may descend from primordial radionuclides with half lives of the order of the age of the Earth which is approximately 4.5 billion years, for instance ^{40}K , ^{232}Th , and ^{238}U . These Earth-related natural radionuclides (^{40}K , ^{232}Th , and ^{238}U) are very large in quantity and the energy of emitted γ radiation is enough to be measured in situ.

2.4.1 ^{40}K

^{40}K can either decay by β^- decay to ^{40}Ca or by electron capture to an excited state of ^{40}Ar . In β^- decay, neutron-rich nuclei may transform a neutron into a proton by the emission of an electron and anti-neutrino and raising the atomic number by 1, whereas in EC, a proton is converted to a neutron through the capture of an electron of the atomic nucleus [Leo, 1987]. The excited ^{40}Ar state decays to the ground state through the emission of a 1.461 MeV γ -ray (as displayed in Figure 2.4).

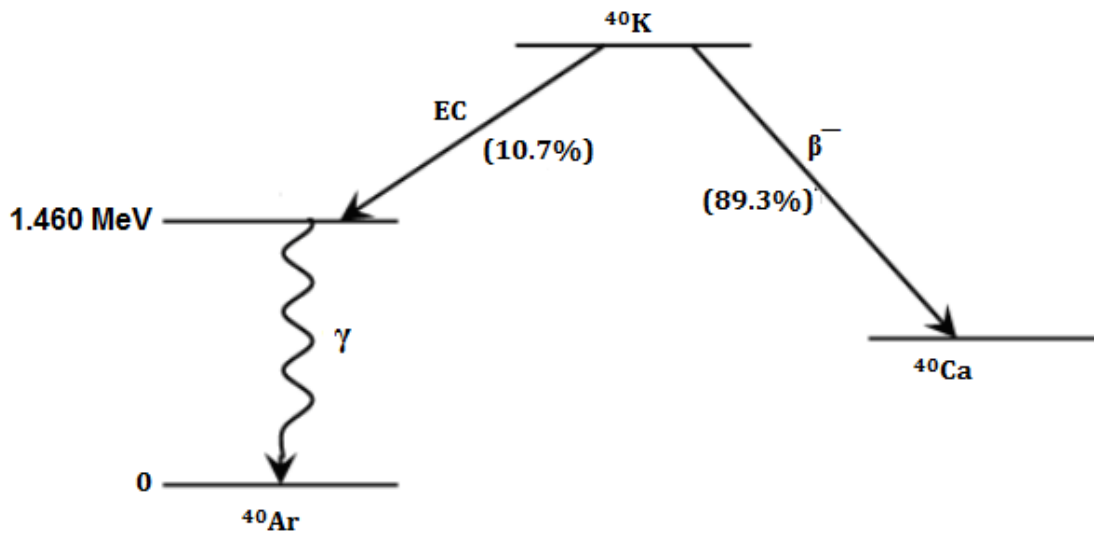


Figure 2.4: Diagrammatic representation of the decay of ^{40}K showing two decay modes, β^- decay to ^{40}Ca (89.3%) and electron capture to an excited state of ^{40}Ar (10.7%) [Firestone, 1996].

2.4.2 The natural decay series of ^{232}Th and ^{238}U

The decay chain refers to the radioactive decay of discrete radioactive decay products as a chained series of transformations, where each decay series step requires a specific time. Radionuclide decay chains are important in preparation for the management and disposal of radioactive materials and waste. As radioactive decay advances, the concentration of the original radionuclides reduces, while the concentration of their decay products rises and then reduces as they undergo transformation.

2.4.2.1 Decay series of ^{232}Th

^{232}Th decays through a series of 10 steps by the emission of α and β^- radiation, into a stable form of ^{208}Pb , (see Figure 2.5). ^{232}Th is the primordial isotope of thorium and successfully builds up all of natural thorium, with some trace amounts of thorium isotopes coming from comparatively short-lived decay products of uranium and thorium. The decay chain of ^{232}Th constitutes 5 radionuclides with half-lives longer than a day with [^{232}Th , $T_{1/2} = 1.9 \text{ years}$; ^{228}Ra , $T_{1/2} = 5.8 \text{ years}$] two longer lived decay by-products. The remainder is a series of shorter-lived radionuclides, and with a stable isotope of ^{208}Pb at the end of the chain. The gaseous radon isotope [^{220}Rn , $T_{1/2} = 56 \text{ s}$] is a very short-lived radionuclide, and because of its half-life, it cannot be carried for long

distances before decaying. Branching ratios and γ -ray emissions are deduced from [Firestone, 1996]. When ^{232}Th concentrations are mentioned in this thesis, it usually refers to the ^{232}Th decay series.

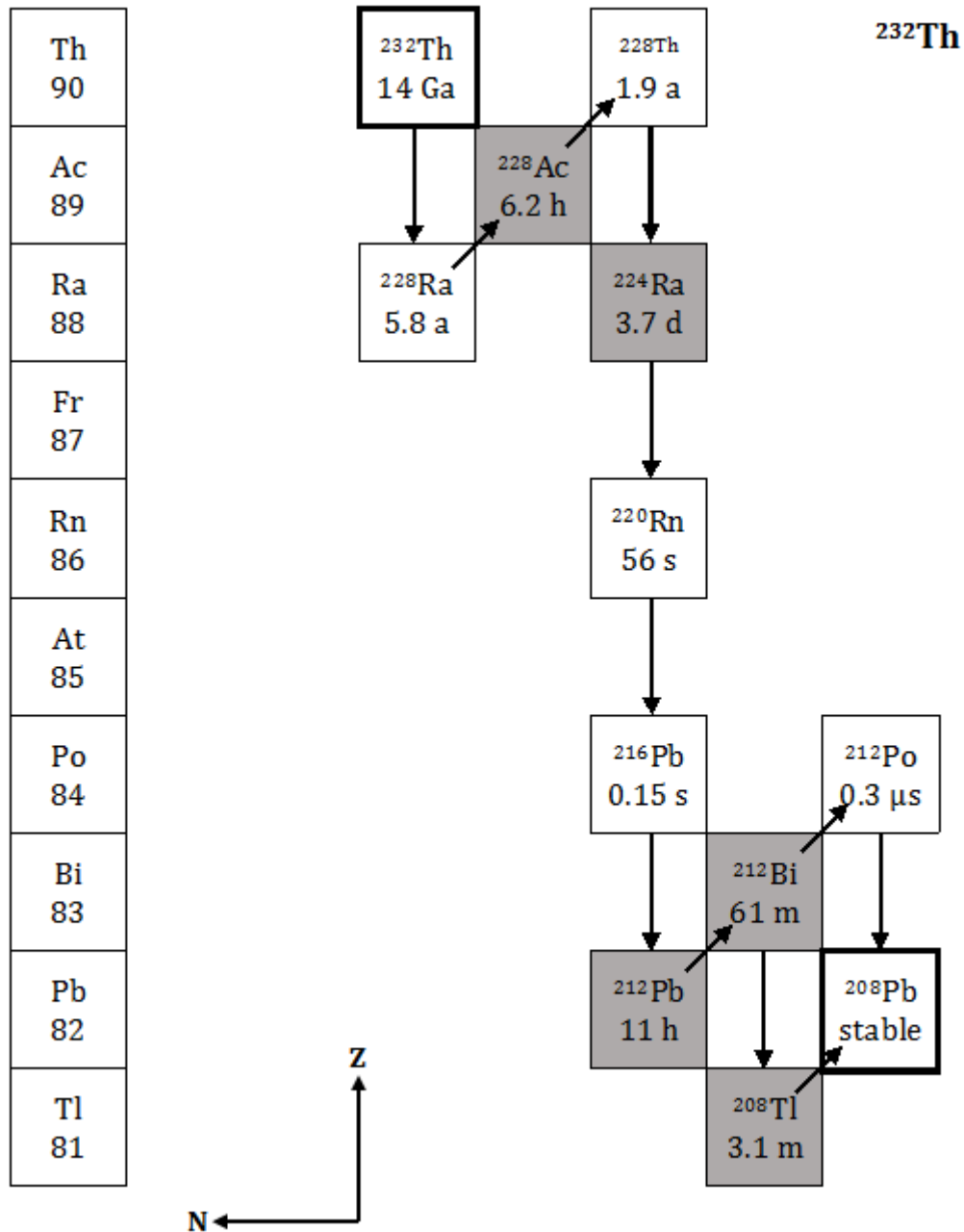


Figure 2.5: Diagrammatic representation of the decay series of the natural radionuclide ^{232}Th . The initial and final nuclides are indicated by a bold square. The downward arrows represent α radiation and the diagonal arrows represent β^- radiation. Each box also indicates $t_{1/2}$ (a for years, m for months, d for days, h for hours and s for seconds). The highlighted squares indicate the prominent γ -ray emitters that are measured in this study [Firestone, 1996].

2.4.2.2 Decay series of ^{238}U

^{238}U is the most common isotope of uranium found in nature; it is not fissile but yet fertile material and is 99.3% of all natural uranium while the remainder of 0.7% is the fissionable ^{235}U . Diverse evaluation studies have shown that ^{238}U and its progeny can be of particular importance in determining the long term radiological impact of deep geological disposal facilities for solid radioactive wastes [Smith, 2010; Mitchell 2013]. ^{238}U decays through a series of 16 steps to finally become a stable form of ^{206}Pb by the emission of α and β^- radiation, (see Figure 2.6). The ^{238}U decay chain constitute about 12 radionuclides with half-lives longer than a day, a sequence of even shorter lived radionuclides, and a stable isotope of ^{206}Pb at the end of the chain.

^{222}Rn is gas and has a short half-life (3.8 days) meaning that it emits α particles at a high rate. ^{222}Rn can quickly spread when dissolved in water, and/or air before it decays. It is not easy to test if secular-equilibrium conditions are attained from γ -ray measurements alone, since the portion of the uranium series prior to ^{222}Rn comprises only one significant γ -ray emitter, $E_\gamma = 186 \text{ keV}$, $I_\gamma = 3.6\%$. Secular equilibrium is considered broken, if there is a net ^{222}Rn flow out of the system which is measured. The γ radiation detected thereafter from the ^{222}Rn descendants cannot be used to determine the ^{238}U concentration. All branching ratios and γ -ray emissions are obtained from [Firestone, 1996].

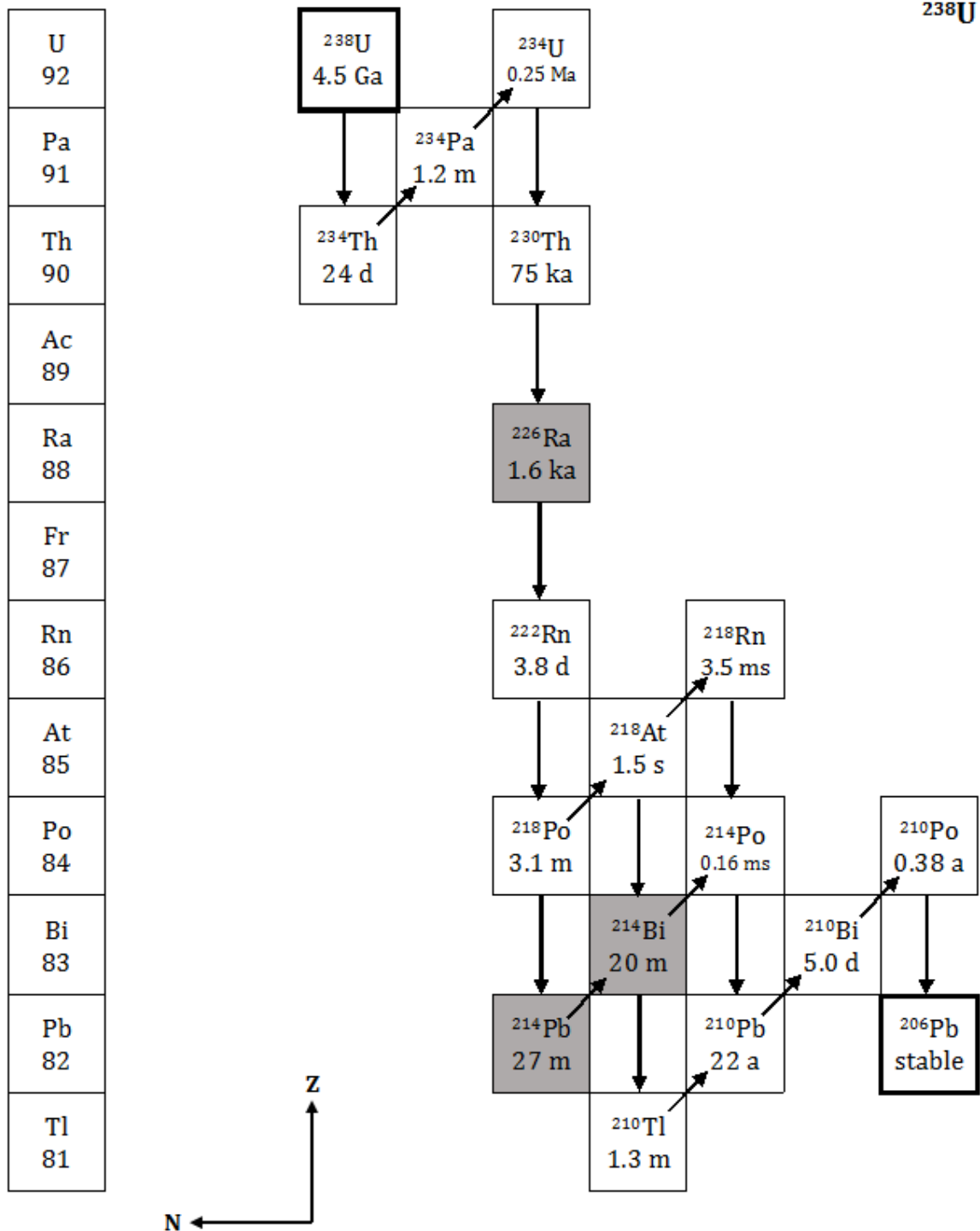


Figure 2.6: Diagrammatic representation of the decay series of the natural radionuclide ^{238}U . The initial and final nuclides are indicated by a bold square. The downward arrows represent α radiation and the diagonal arrows represent β^- radiation. Each box also indicates $t_{1/2}$ (a for years, m for months, d for days, h for hours and s for seconds). The highlighted squares indicate the prominent γ -ray emitters that are measured in this study [Firestone, 1996]. ^{234}Pa is used but has a weak γ -ray.

2.5 Detectors

Scintillation and semiconductor diode detectors are two main classes of solid-state radiation detectors, which dominate the area of ionizing radiation measurements [Kastalsky, 2006]. Scintillators are materials that are sensitive to high energy radiation which causes photons through ionisation. The resultant light is successively registered by a photo-detector, usually a photo-multiplier that transforms light into an electrical signal. Scintillators can have large detection volume [Zaid, 2006]. Semiconductor diode detectors make use of reverse biased p-n junctions where the consumed radiation generates electrons and holes, which are partitioned by the junction field, by that means giving rise to a direct electrical response [Gilmore, 2008; Krane, 1988]. The sensitivity of semiconductor diode detectors depends on the length of the field region, and semiconductor diode detectors have good spectral energy resolution of the ionizing radiation.

2.5.1 General characteristics of γ detectors

The detectors reviewed here are the NaI(Tl) scintillation detectors and Hyper-Pure Germanium semiconductor detectors. These detectors are also used to count electrons and heavy charged particles, but for this study, interest will focus only on γ -ray detections. Generally, scintillation detector is made up of a scintillating material which is optically combined directly, or through a light guide to a photo-multiplier. The radiation progressing through the scintillator stimulates the atoms and molecules assembling the scintillator stirring up light to be emitted. This light is conveyed to the photo-multiplier where it is transformed into a weak current of photo-electrons, and additionally, amplified by an electron multiplier system. The electronics system analyses the resultant voltage signal [Leo, 1987].

In 1948, Robert Hofstadter demonstrated that sodium iodide, to which a barely discernible amount of thallium iodide had been added in the melt, created a peculiar substantial scintillation light output with comparison to the organic materials that had dominated earlier [Iwanczyk, 2000]. The inorganic scintillators are to a great degree crystals of alkali halides and the most extensively used material is NaI(Tl) where thallium is the impurity activator, because of its availability in large volumes at relatively low cost. NaI(Tl) is hygroscopic, thus its crystal ought to be canned in an

closed container for standard use and will degenerate due to water absorption if exposed to the atmosphere for any period time.

Semiconductor detectors use crystalline semiconductor materials as the foundation, most remarkably germanium and silicon. Germanium is comprehensively deployed in the γ -ray measurements [Knoll, 2010]. The lower band also known as the valence band correlates with the outer-shell electrons that are bound to definite lattice sites within the crystal. In the instance of germanium, they are segments of the covalent bonding that account for the interatomic forces in the crystal. The higher-lying band also known as the conduction band, contain electrons that are unrestricted to drift throughout the crystal. The electrons in this band give rise to the electrical conductivity in the material and the two bands are set apart by the band-gap, where the band-gap energy is about 1 eV for the semiconductors. Figure 2.7 illustrates electron energy in various materials; the band-gap literally represents the energy difference between the levels of the two bands.

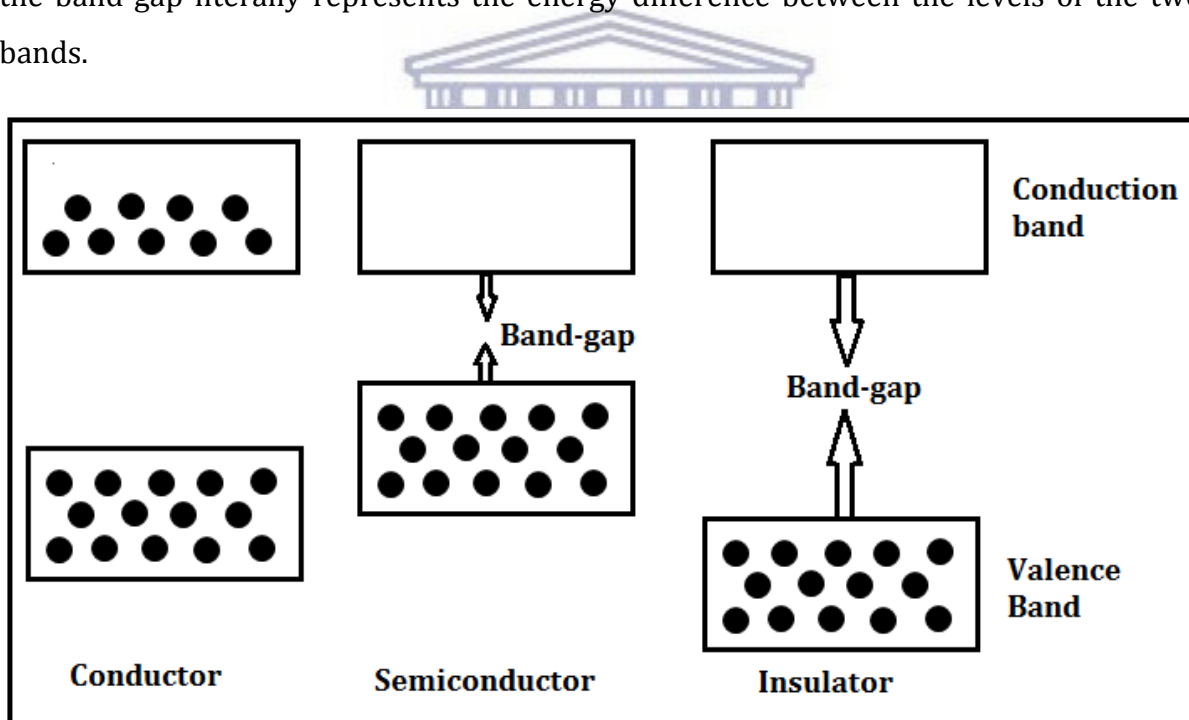


Figure 2.7: Electron energy levels in various materials. The band-gap literally represents the energy difference between the levels of the two bands.

In the early 1960s, the devices making use of semiconductors as the central detection channel were empirically accessible [Flakus, 1981]. Some of the thermal energy is distributed to the electrons in the crystal, if and only if the temperature is not zero. The valence electrons may obtain adequate thermal energy to be promoted over the band-

gap into the higher-lying band. This is excitation of an electron that is a constituent of a covalent bond such that the electron can evacuate a certain bonding site, and migrate through the crystal. This process of excitation produces an electron in the empty higher-lying band, and also cause to remain a vacancy called a hole in the valence band or simply lower band and their merger is known as electron-hole pair. By taking into account the electric field, the electron will begin to move. The net positive charge, the hole, shall be prone to move in the electric field, but in the reverse direction to the electron.

In comparison, the NaI(Tl) scintillation detectors are made up of a higher Z material at a very high density generally have a large thickness, usually 8 cm, whilst Ge semiconductor detectors have the same advantages with the NaI(Tl) detectors, but they have a lower Z material than the iodine of the NaI(Tl) detectors and are generally smaller in volume. Consequently, the NaI(Tl) scintillation detectors have a good probability for detecting γ -rays and even a better probability for absorbing all of the γ energy than the Ge semiconductor detectors, as illustrated by Figure 2.8 below.

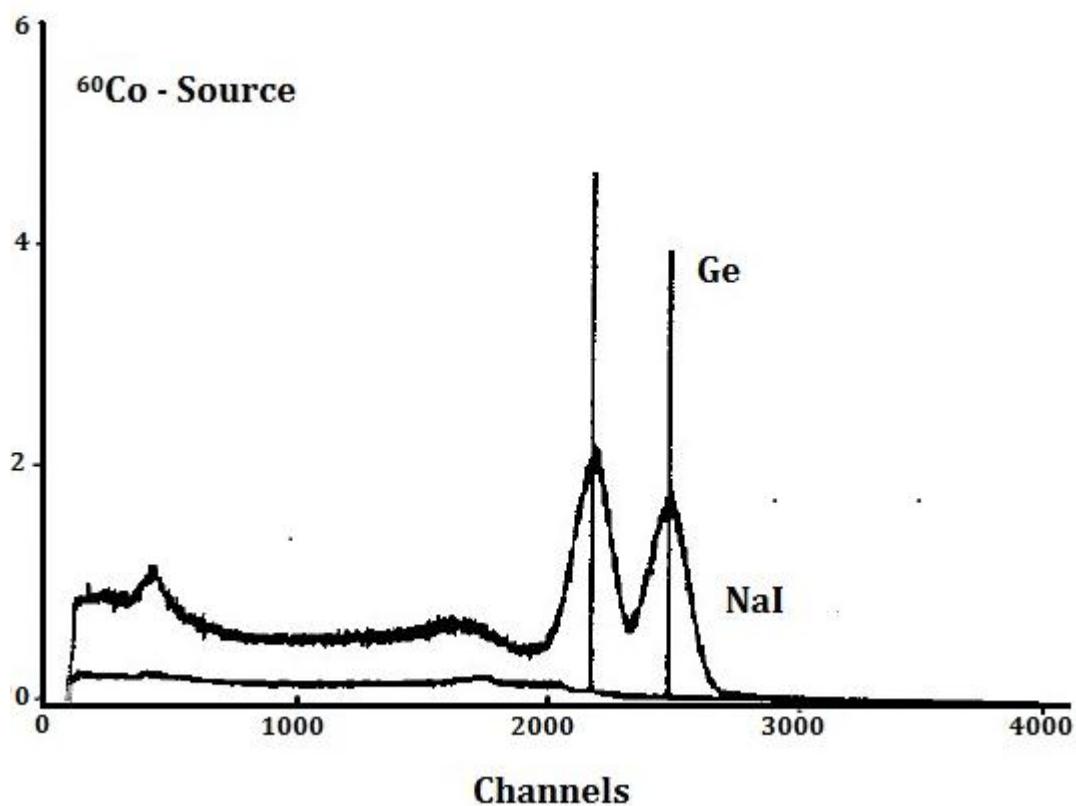


Figure 2.8: A spectrum plotted in comparison between Ge semiconductor detector and NaI scintillation detector using ^{60}Co source [Leo, 1987].

The NaI(Tl) detectors depends on the collection of light to function and Ge semiconductor detectors depends on the collection of charge to operate, and for this reason they cannot be directly compared, but however, the average energy needed to produce a charge carrier-pair is about 3 eV for semiconductor detectors and the average energy required to produce a light photon is about 100 eV [Debertin, 1988]. The HPGe detector used in this study has a 45% efficiency relative to a 3' × 3' NaI(Tl) detector at 1.332 MeV. According to Gilmore (2008) a gamma-ray with energy of 661.67 keV completely absorbed in a germanium detector can be expected to create 3.9 million electron-hole pairs. The same gamma-ray absorbed in sodium iodide will only give rise to 3900 photoelectrons. This thousand-fold difference in the number of charge carriers created is the most important reason for the poor resolution of sodium iodide detectors compared to an HPGe detector.



Chapter 3

METHODOLOGY

Gamma-ray spectrometry is a basic tool used for the determination of activity concentrations in environmental samples from water or soils [Eduardo, 2005] using gamma-emitting radionuclides. Accurate and precise activity measurements by this technique using gamma-ray detectors require proper calibrations before they can be used [Švec, 2008].

3.1 HPGe Detector system

Hyper Pure Germanium (HPGe) detectors, also called intrinsic Germanium detectors, are commonly used for gamma-ray detection because of their excellent energy resolution, good signal-to-noise ratio and modest efficiency. The primary application of HPGe detectors is gamma-ray spectroscopy at photon energies from a few keV up to about 10 MeV.

3.1.1 Instrumentation

The Hyper-Pure Germanium (HPGe) detector available at the Environmental Radioactivity Laboratory (ERL) of iThemba LABS is a closed-end coaxial Canberra GC4520 model (p type, 45 % relative efficiency, 2 keV FWHM resolution at 1332 keV) [Newman, 2008; Talha, 2008] and is encased in a 10 cm thick lead castle fitted with a 2.0 mm thick copper inner lining. This detector has an HPGe crystal of diameter 6.25 cm and length of 5.99 cm, (see Figure 3.1 and Table 3.1). The HPGe crystal is mounted in a vertical dipstick liquid nitrogen (LN₂) cryostat. Just like typical germanium detectors, the ERL HPGe detector uses liquid nitrogen to cool to optimal operating conditions. The system is kept at cryogenic temperature when in use.

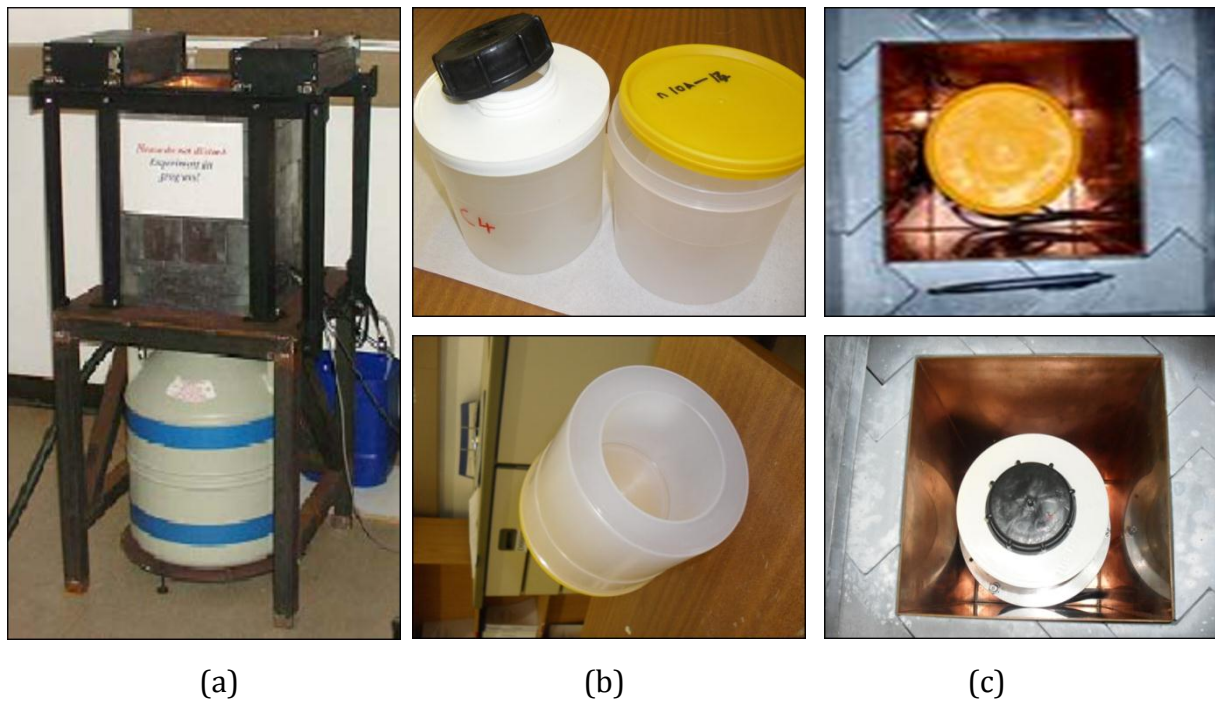


Figure 3.1: Photographs of (a) the ERL HPGe detector system, (b) Marinelli beakers used for samples and (c) the top view showing Marinelli beaker inside the castle.

Table 3.1: Summary of the electronic components and equipment used for gamma-ray spectroscopy in this study.

Detector: HPGe	Bias	+3500 volts
	Geometry	Closed-end coaxial
	Diameter	62.5 mm
	Length	59.0 mm
	Energy range	50 keV – 4000 keV
	Crystal type	Vertical dipstick
	Preamplifier	D-C coupled
Amplifier	Spectroscopy amplifier	ORTEC model 572
MCA	Atomki Palmtop	8k (8192 channels)
Low background shielding	Material	Lead
	Shape	Square
	Length	40 cm
	Height	60 cm
	Thickness	10 cm

Figure 3.2 shows the electronic block diagram of the experimental setup of the HPGe γ -ray detector system. In this setup, a high voltage power supply was originally set to zero

and switched off. Before starting to power up, the polarity was set to positive on the high voltage. The high voltage was then switched on and turned up slowly at approximately 100 V/s to the operating voltage of +3500V. A pulse is produced which is caused by the electron-hole pairs formed during the transfer of photon energy to atoms in the crystal which result in the emission of electrons.

The detector provides the signal in the form of current, which goes to a preamplifier. The principal function of the preamplifier is to amplify very weak signals from the detector and transmit the signal to the amplifier. Because of the very weak input signal, preamplifiers are mounted as close to the detector as they can be. A charge sensitive preamplifier will convert the charge into a voltage pulse proportional to the energy deposited in the detector crystal. The amplifier simply amplifies the pulse that comes from the preamplifier, and also shapes the signal. The amplifier also reverses the negative polarity of the signal coming from the preamplifier, for the reason that the Analog-to-Digital Converter (ADC) only handles signals of positive polarity.

The ADC converts the analog signal from the amplifier into digital form, thus the ADC receives the incoming uninterrupted signal and allocates a digital number that characterizes the amplitude of the signal. Then the pulse from the ADC is received by the Multi-Channel Analyzer (MCA). The pulse from the amplifier is collected and sorted by the ATOMKI Palmtop software multi-channel analyzer installed and linked to a desktop PC.

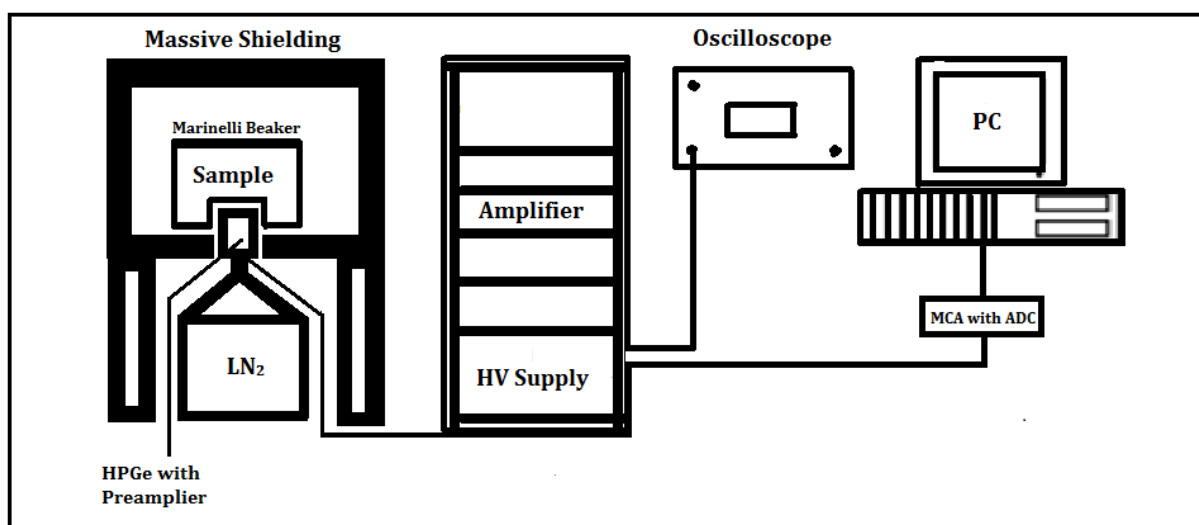


Figure 3.2: Block diagram showing how the components of the high resolution ERL HPGe gamma ray spectrometry experimental system interlink.

3.1.2 Spectrometer Calibration

A digital gamma-ray spectrum is essentially a list of numbers of pulses measured within small consecutive pulse height ranges. Detector calibration allows the gamma-ray spectrum to be interpreted in terms of energy, rather than channel number, and activity of the radionuclide, rather than number of pulses [Gilmore, 2008]. Appropriate gamma-ray spectra are used to calibrate spectrometers. For this purpose, known radionuclides with their gamma-ray energies, the branching ratio of these radiations and the half-life of the nuclide are required.

Prior to the sample measurements, a background spectrum is acquired which will be used for background corrections. For energy and efficiency calibrations, certified reference materials are required.

Energy calibration

The main purpose of the energy calibration is to derive a relationship between peak position in the multi-channel analyser with relevant γ -ray energy. This relationship between channel number and the energy was determined to be a linear function and is given by:

$$E = a + b \times Chn \tag{3.1}$$

where E is the energy of the gamma and Chn is the channel number of the centre of the photo-peak. The constants a and b are calibration parameters, with a an energy and b with units of [energy/ (channel number)]. Since the sources contain radionuclides with known gamma-ray energies, the calibration parameters can be determined. The system was energy calibrated with a certified ^{232}Th ore (IAEA/RGTh-1) such that the centroid of the photo-peak energies are linked with their corresponding channel numbers, see for example Figure 3.3 where a fit with $a = -1.27$ and $b = 0.52237$ is obtained..

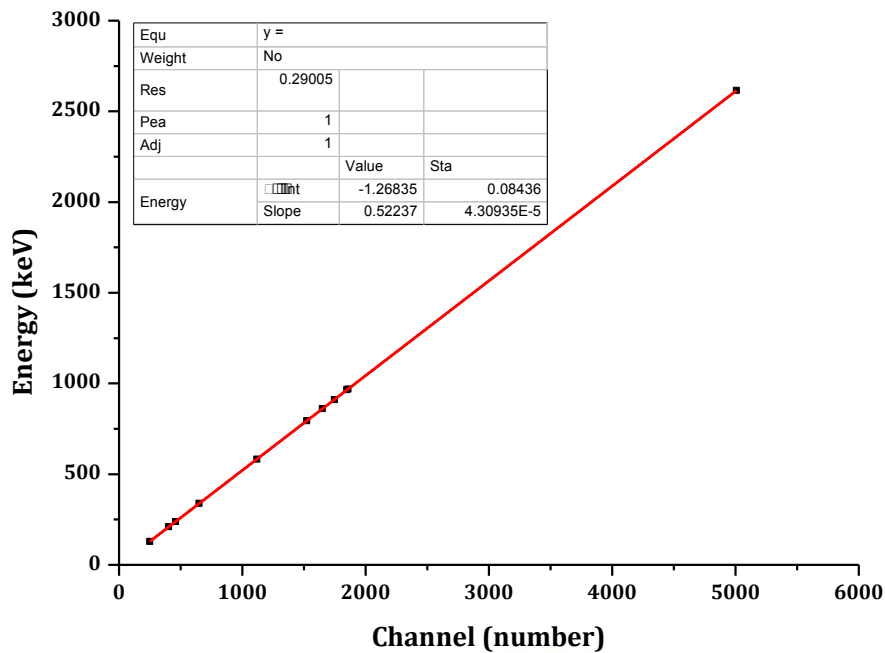


Figure 3.3: Peak energy as a function of channel number.

Efficiency calibration

The purpose of radiation detection is generally to measure an output pulse for each radiation event within the active volume in a detector. For γ -ray spectrometry of unknown activity in samples, it requires accurate counting efficiency of the detector. The absolute full-energy peak efficiency is used to relate the peak area in the spectrum to the activity of the radioactive sample [Gilmore, 2008]. The absolute full-energy peak efficiency is defined as the ratio between the number of particles detected to the number of particles emitted as follows:

$$\varepsilon_f = \frac{N_p}{N_\gamma} \quad (3.2)$$

where ε_f is the full-energy peak efficiency, N_p is the net γ -ray count rate in the full-energy peak and N_γ is the γ -ray emission rate. If the efficiency of the detector is known, then by measuring the number of particles detected, the number of particles emitted in a sample can be determined. The most important factors affecting the efficiency of the detector are:

- The source-detector geometry: the number of particles detected will depend on how close the source is to the detector. The closer the source is to the detector, the larger the efficiency.
- The size of the detector: large detectors are usually more efficient, since this large volume provides more material for the particles to be absorbed in.
- The energy of the gamma-ray: the photo-peak is produced mainly by photo-absorption. This photo-absorption process has strong energy dependence. For low energy photons, photo-absorption has a higher probability to occur than photons of high energy.

The efficiency calibration of the HPGe system for the granite samples investigated in this work forms an important part of this thesis.

3.1.3 Marinelli beaker geometry

The available detector system of the ERL has been efficiency calibrated using Marinelli beaker geometry. Furthermore, benchmark studies were performed using Monte Carlo simulations for that geometry.

Full-energy peak efficiency

According to Talha (2009, 2010), the approach for ascertaining exactly the full-energy peak efficiency for the 1.3 L full Marinelli beaker filled with water was determined and verified using Monte Carlo simulations. By applying similar techniques, full-energy peak efficiencies were computed with Monte Carlo simulations in a 1.3 L Marinelli beaker filled with a liquid up to the 1 L mark, see Figure 3.4. Furthermore, to validate the simulated data, standard reference sources (1 L volume) comprised of ^{137}Cs and ^{40}K was used to determine the absolute efficiencies for these radionuclides. The duo ^{137}Cs and ^{40}K have single gamma-ray energy each; consequently they are not prone to coincidence summing. Figure 3.4 displays simulated data and two measured data points that are in agreement, as a result the simulated full-energy peak efficiency curve was used for further analysis.

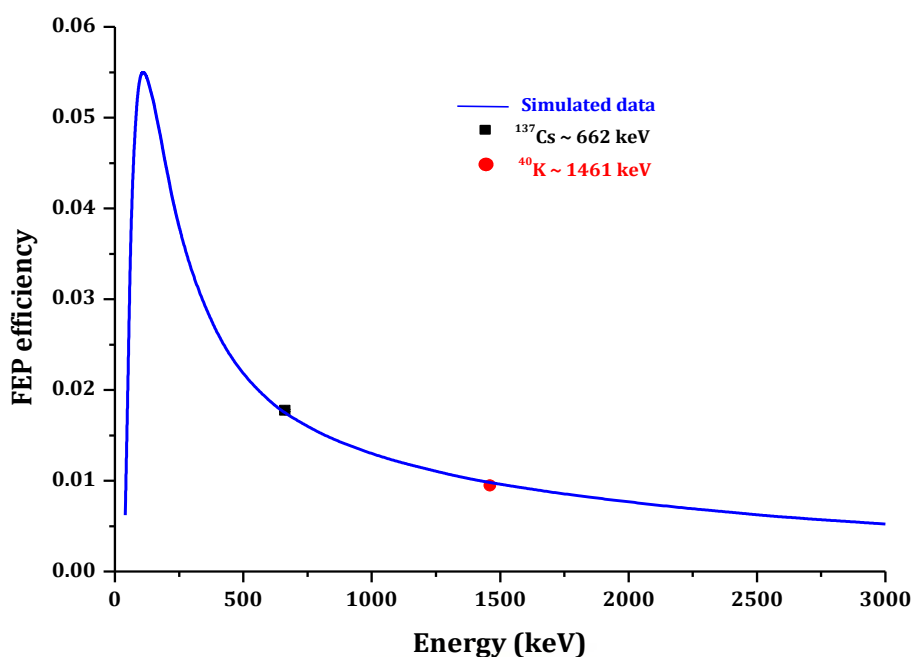


Figure 3.4: MCNPX simulated (solid line) and measured (points) full-energy peak (FEP) detection efficiencies for the ERL HPGe detector system in the 1.3 L screw-top Marinelli beaker geometry filled to the 1 L mark by [Maleka, 2012].

Certified reference materials

Table 3.2 present details about the certified reference materials prepared by the Council for Scientific and Industrial Research (CSIR) and National Metrology Institute of South Africa (NMISA). Moreover, Appendix B gives extended descriptions about these sources. These samples were prepared in Marinelli beakers and filled up to the 1 L mark.

Table 3.2: Activity concentrations of the certified reference materials CSIR and NMISA at the time they were characterized by the supplier. (All uncertainties are at the 1σ level).

Sample Label	Radionuclide	Activity (Bq/L)	Reference date	Supplier
CSIR	¹⁵² Eu	6550 ± 196	20 January 2002	CSIR
	¹³⁷ Cs	661 ± 13		
	⁶⁰ Co	1907 ± 38		
NMISA	¹⁵² Eu	6470 ± 181	20 October 2010	NMISA
	¹³⁷ Cs	617 ± 18		
	⁶⁰ Co	1859 ± 52		

HPGe photo-peak detection efficiency

Table 3.3 presents the radionuclides of ^{152}Eu , ^{137}Cs and ^{60}Co and corrected activity concentrations for the decay of radionuclides in the standard liquid sources, the CSIR and NMISA samples. The current activity concentrations were calculated using the following equation:

$$A(t) = A_0 e^{-\lambda t} \quad (3.3)$$

where A is the radioactivity at a given time (t), A_0 (see Table 3.2 for reference) is the initial radioactivity at t_0 and λ is the decay constant.

Table 3.4 presents the ^{152}Eu , ^{137}Cs and ^{60}Co radionuclides with their respective gamma-ray energies and branching ratios extracted from Firestone (1996). The γ -ray spectrum shown in Figure 3.5 is acquired from the water-equivalent polymer-based standard sources (^{152}Eu , ^{137}Cs and ^{60}Co) in a 1 litre Marinelli beaker, prepared by NMISA. The majority of these photo-peaks ranging from 121 to 1408 keV belong to ^{152}Eu (labelled in black), one photo-peak at 662 keV from ^{137}Cs (labelled in red) and two photo-peaks at 1173 and 1332 keV from ^{60}Co (labelled in green) as indicated in Figure 3.5 and also in Table 3.4.

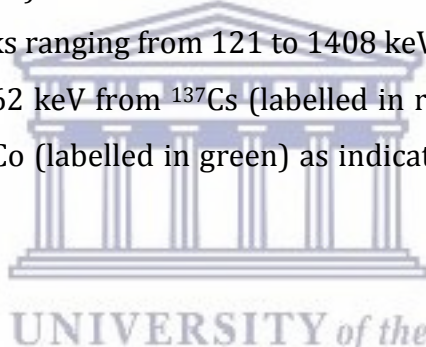


Table 3.3: Current activity concentrations of radionuclides in the certified reference materials CSIR and NMISA at the time of measurement. (All uncertainties are at the 1σ level)

Sample	Radionuclide	Activity (Bq/L)	Measurement date	Supplier
CSIR	^{152}Eu	3689 ± 110	02 April 2013	CSIR
	^{137}Cs	511 ± 10		
	^{60}Co	437 ± 9		
NMISA	^{152}Eu	5693 ± 159	18 April 2013	NMISA
	^{137}Cs	583 ± 17		
	^{60}Co	1339 ± 37		

Table 3.4: Gamma-ray lines and associated branching ratios (Firestone, 1996) for the given radionuclides present in the liquid standard sources.

Radionuclide	Energy (keV)	Branching ratio
¹⁵² Eu	121.8	0.2837
	244.7	0.0753
	344.3	0.2657
	411.1	0.0224
	444.0	0.0313
	778.9	0.1297
	867.4	0.0421
	964.1	0.1463
	1085.8	0.1013
	1089.7	0.0173
	1112.1	0.1354
	1212.9	0.0141
	1299.1	0.0163
1408.0	0.2085	
¹³⁷ Cs	661.7	0.8510
⁶⁰ Co	1173.2	0.9986
	1332.5	0.9998

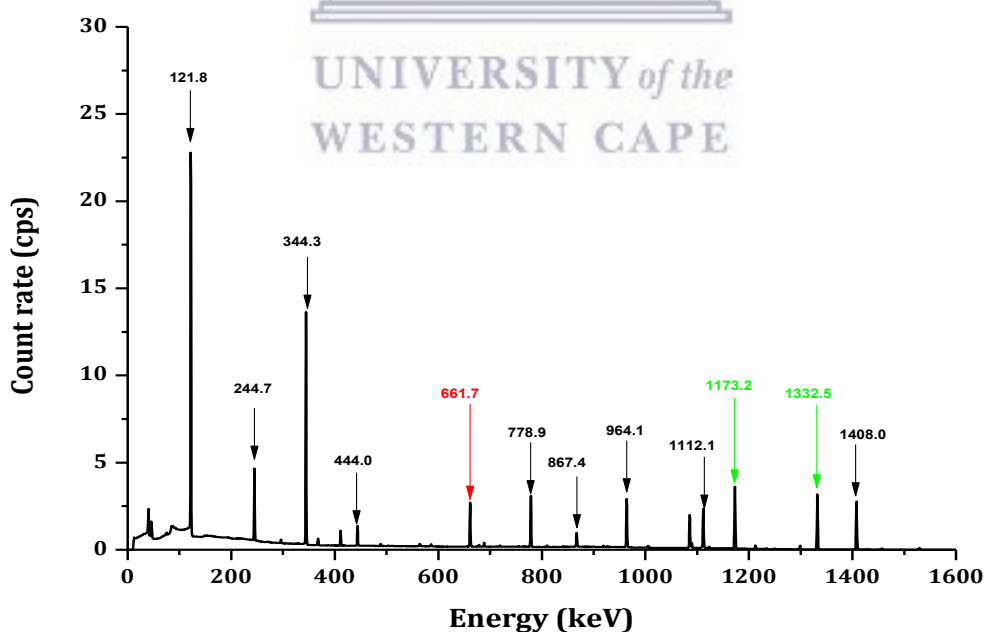


Figure 3.5: The photo-peak spectrum from NMISA liquid standard showing the energies of the gamma-ray lines.

Absolute efficiency

The relationship between the gamma photo-peak efficiency ε_γ of a detector and the gamma photo-peak energy E at definite energy limits (at energies > 120 keV) can be expressed by the Power Function [Debertin, 1988].

$$\varepsilon_\gamma = aE^b \quad (3.4)$$

with $E = E_\gamma/E_0$ and $E_0 = 1$ keV, a and b are dimensionless parameters with $a > 0$, and $b < 0$, thus, there is an inverse proportionality relationship between ε_γ and E . From the additive logarithm rule, the logarithm of the efficiency can be elicited as the function of the logarithm of the energy,

$$\log \varepsilon_\gamma = b \log E + \log a \quad (3.5)$$

This is a linear equation where, E ranges from 121 – 1408 keV and both a and b are dimensionless fit parameters. The parameters a and b are correlated with correlation coefficient $\rho_{a,b}$, meaning that the uncertainties should also be correlated, in addition, let covariance be $cov(a, b)$.

$$cov(a, b) = \rho_{a,b} \cdot \sigma_a \cdot \sigma_b \quad (3.6)$$

with σ_a and σ_b the uncertainty in the parameters a and b respectively, therefore, the efficiency uncertainty $\sigma_{\varepsilon_\gamma}$ is a function of σ_a , σ_b and $cov(a, b)$.

$$\sigma_{\varepsilon_\gamma} = \varepsilon_\gamma \sqrt{\left(\frac{\sigma_a}{a}\right)^2 + 2 \frac{\ln 2}{a} \cdot cov(a, b) + (\sigma_b \ln E)^2} \quad (3.7)$$

Following the analytical efficiency fit, the efficiency curves (Figure 3.6 & Figure 3.7) were plotted for the standard sources from the CSIR and NMISA. The two efficiency functions are comparable.

Coincidence summing effects play an important role in HPGe spectrometry at low source to detector distances. Section 3.3.2 discusses coincidence summing problems encountered when measuring aqueous samples in Marinelli beakers using γ -ray spectroscopy with HPGe detectors. This section discusses the determination of coincident γ -rays from ^{60}Co , but mainly focusing on coincidence summing in ^{152}Eu . Calibrations with the coincident γ -ray radionuclides ^{60}Co and ^{152}Eu are compared to

essentially coincidence-free calibrations. For these measurements, the Maleka (2012) efficiency curve for 1 L Marinelli beaker geometry was utilized.

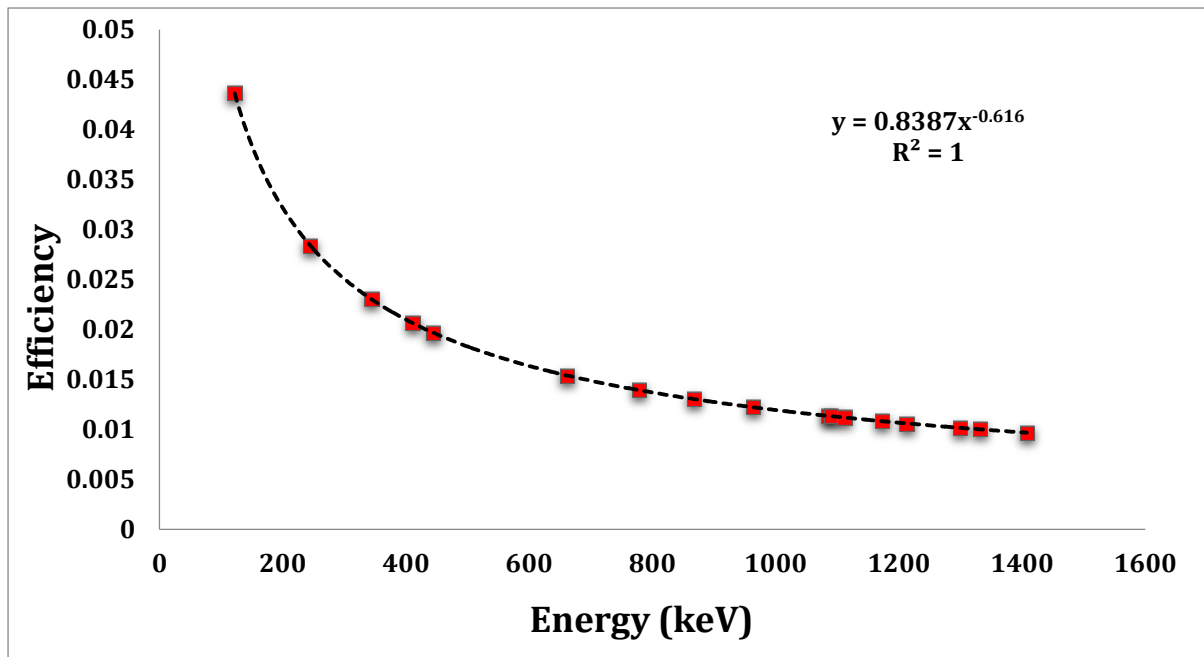


Figure 3.6: Absolute efficiency curve simulated using the standard a liquid source. The points are associated with the gamma-ray energies from ^{152}Eu , ^{137}Cs and ^{60}Co in the CSIR measurement.

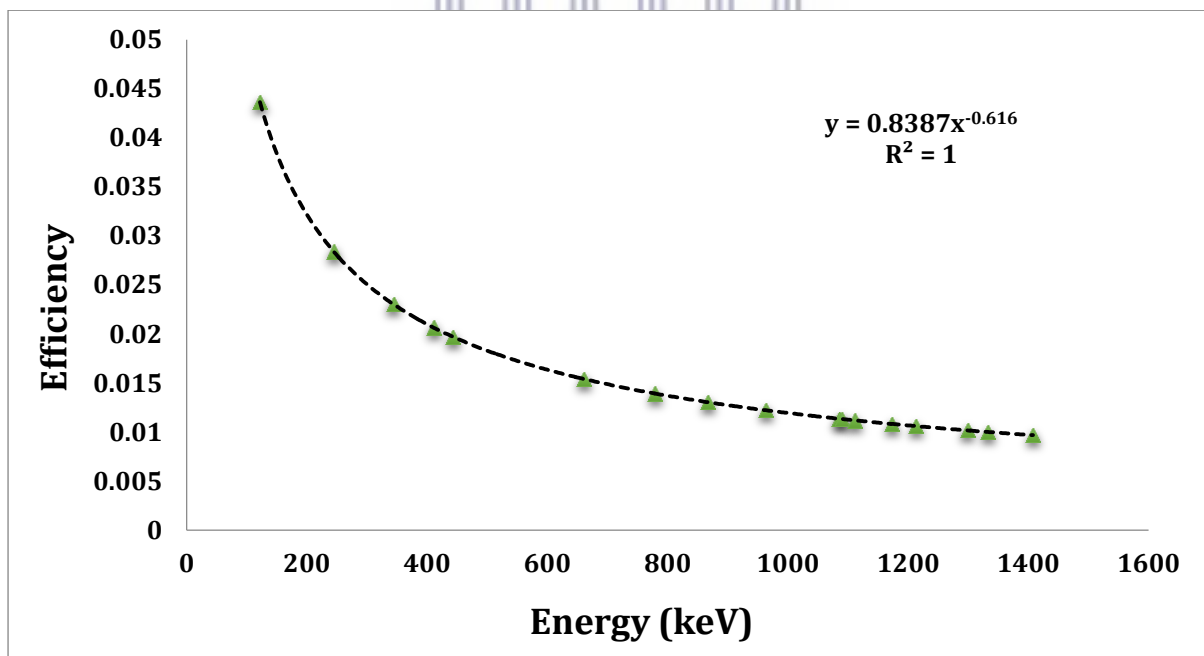


Figure 3.7: Absolute efficiency curve simulated using the standard liquid source. The points are associated with the gamma-ray energies from ^{152}Eu , ^{137}Cs and ^{60}Co in the NMISA source.

3.1.4 Granite countertops geometry

The HPGe γ -ray detector system available at iThemba LABS is calibrated for Marinelli beaker geometry. In order to measure the activity concentrations from granite countertops which have different measuring geometry (rectangular samples) from that of the Marinelli beaker, a new calibration was required. A study was performed to prepare a 'certified reference material' by making use of known Marinelli beaker efficiencies to determine the activity concentrations of a soil sample. Once the soil sample has been well characterised using the Marinelli geometry, it was then decanted into a sample holder, similar to the granite countertop samples. The soil sample used was collected from a heavy mineral mine, hence the density was also comparable to our samples when prepared in the new sample holder. See section 3.2.1 for a discussion on the preparation of the sample.

The activity concentration was calculated to be 940 ± 30 Bq/kg, 660 ± 20 Bq/kg and 153 ± 8 Bq/kg for the ^{238}U series, ^{232}Th series and ^{40}K , respectively. The sand was transferred from the Marinelli beaker into the rectangular box of similar dimensions to the granite countertops by methods described in Section 3.2. In order to deduce the efficiencies for the granite countertop geometry, the measured activity concentrations of the sand were used. Figure 3.8 shows the new efficiency calibration of the system for the countertop geometry of each nuclide and its associated standard uncertainty which were calculated from the self-prepared 'certified reference material'.

As a quality control measure, the prepared sample was counted 5 times at iThemba ERL using the HPGe γ -ray detector system to check for any discrepancy and observe any changes due to secular equilibrium in the ^{238}U series data.

3.1.5 KCl mass and activity relation

In addition to the soil sample prepared in the previous subsection 3.1.4, a KCl sample was also prepared in similar geometry. The amount of ^{40}K in the KCl sample was determined by standard gamma-ray spectroscopy using HPGe γ -ray detector. Figure 3.9 shows a typical spectrum.

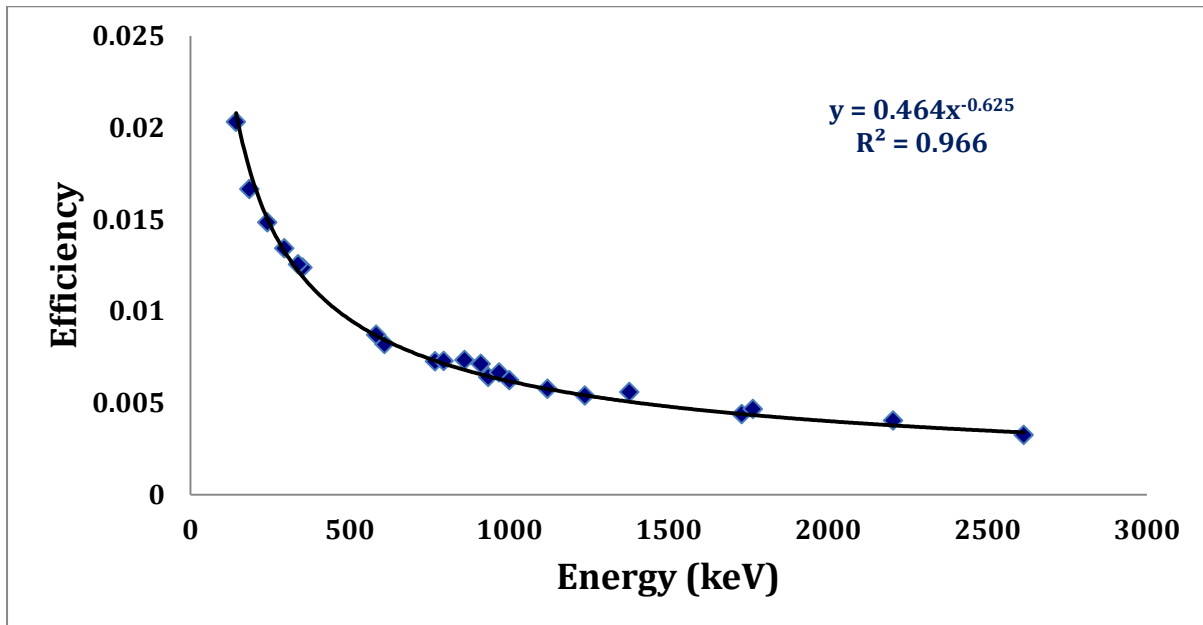


Figure 3.8: Efficiency curve deduced from the prepared reference sand material.

The relation between mass and activity of KCl

- The number of moles in 759 g KCl are determined as:

$$\frac{\text{KCl}_{\text{mass}} (\text{g})}{\text{KCl}_{\text{molar-mass}} (\text{g}\cdot\text{mol}^{-1})} = \frac{759 \text{ g}}{74.551 \text{ g}\cdot\text{mol}^{-1}} = 10.18 \text{ mol of KCl} \quad (3.8)$$

- 10.18 mol KCl is equivalent to about 6.4×10^{24} molecules of KCl, hence 6.4×10^{24} atoms of K.
- In nuclei of K, about 0.0117 (1) % are ^{40}K [Fujiyoshi, 2009]. Therefore the number of ^{40}K nuclei present:

$$N = (6.4 \times 10^{24}) \times (1.17 \times 10^{-4}) = 7.51 \times 10^{20} \text{ nuclei of } ^{40}\text{K}. \quad (3.9)$$

- Activity (A) of a radioisotope source is defined as the rate of decay, the fundamental law of radioactivity [Krane, 1988]:

$$A (\text{Bq}) = N \times (\ln 2 / t_{1/2}). \quad (3.10)$$

With $t_{1/2}$ of $^{40}\text{K} = 1.277 \times 10^9$ years [Firestone, 1996]; the activity A (Bq) of ^{40}K in the sample was calculated to be **1.2×10^4 Bq**. During the decay process of ^{40}K , only about 10.7 % of the ^{40}K decays by EC to an excited state of ^{40}Ar which decays to the ground state by the emission of 1461 keV γ -ray.

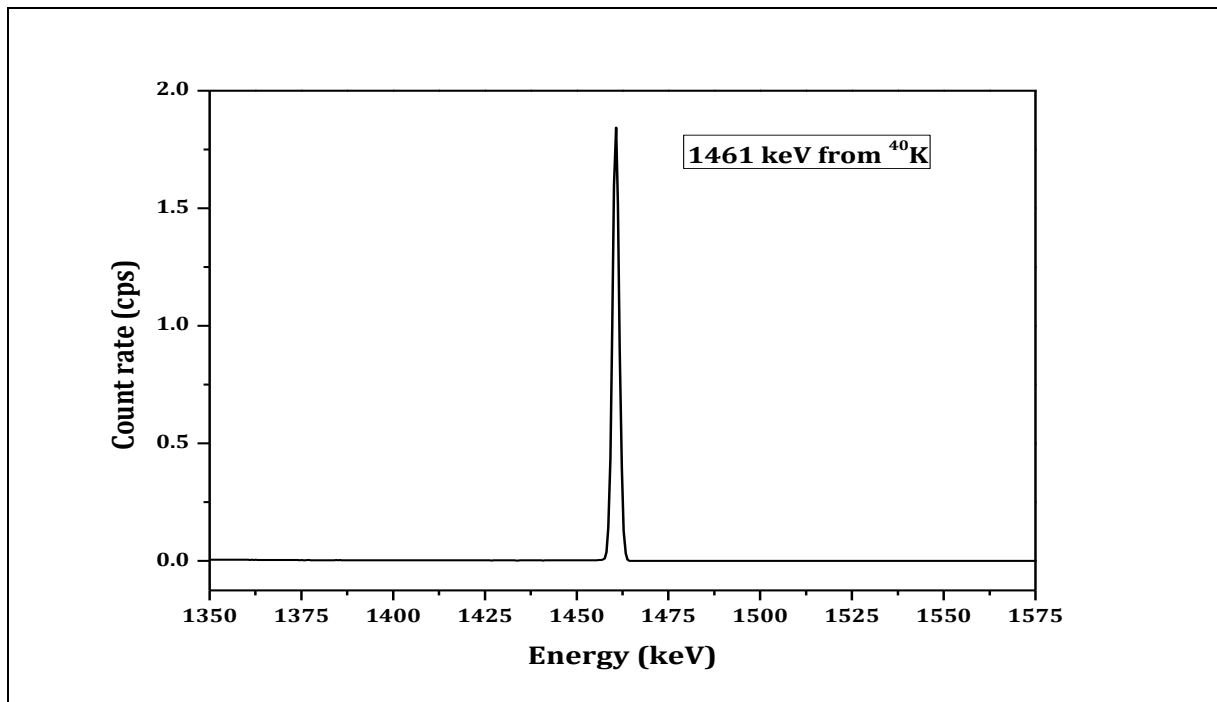


Figure 3.9: A spectrum of the count rate (cps) versus energy (keV) showing a 1461 (keV) photo-peak from ^{40}K .

The KCl mass and activity relation is a technique that uses the fundamental law of radioactivity to determine the activity concentration, see the box on previous page. Using the measured spectrum of the KCl sample, the absolute photopeak efficiency at 1461 keV can be calculated using the total activity of ^{40}K in the sample. This efficiency was also compared to the photopeak efficiency fit of the previous sand sample. Note also that the two samples (KCl and soil) had varying density (see Table 3.6).

For the two geometries, the Marinelli geometry is ideal due to its design, the sample matrix is closer to the detector, and hence the efficiency improves as compared to the granite countertop geometry. Table 3.5 displays absolute emission probabilities obtained from [Firestone, 1996; Newman, 2008] for important gamma-ray energies found in ^{238}U decay series, ^{232}Th decay series and ^{40}K . For the activity concentration calculations using the information in Table 3.5, some gamma-ray lines were ignored as they are prone to coincidence summing as reported by Newman *et al.* (2008).

Table 3.5: Gamma-ray lines in the ^{238}U -series, ^{232}Th -series and ^{40}K with absolute emission probabilities extracted from [Firestone, 1996] and the branching ratio for ^{226}Ra was adopted from [Newman, 2008].

Series/Radionuclide	Nuclide	Energy (keV)	Branching ratio
^{238}U	^{226}Ra	186	0.0617
	^{214}Pb	241	0.0750
	^{214}Pb	295	0.1850
	^{214}Pb	351	0.3579
	^{214}Bi	609	0.4479
	^{214}Bi	768	0.0480
	^{214}Bi	934	0.0303
	^{234}Pa	1001	0.0084
	^{214}Bi	1120	0.1480
	^{214}Bi	1238	0.0586
	^{214}Bi	1377	0.0392
	^{214}Bi	1729	0.0288
	^{214}Bi	1764	0.1536
	^{214}Bi	2204	0.0486
^{232}Th	^{228}Ac	338	0.1125
	^{208}Tl	583	0.3041
	^{228}Ac	794	0.0434
	^{208}Tl	860	0.0447
	^{228}Ac	911	0.2660
	^{228}Ac	968	0.1617
	^{208}Tl	2614	0.3570
^{40}K	^{40}K	1461	0.1067



3.2 Sample Preparation

For counting environmental samples using the gamma-ray method, a large part of the sample must preferably be in as close proximity to the detector crystal as possible [Debertin, 1989]. A one litre Marinelli beaker (see Figure 3.10) is deployed for these measurements. The available HPGe detector system has been calibrated using the Marinelli geometry and most samples counted in the system are prepared in this geometry.

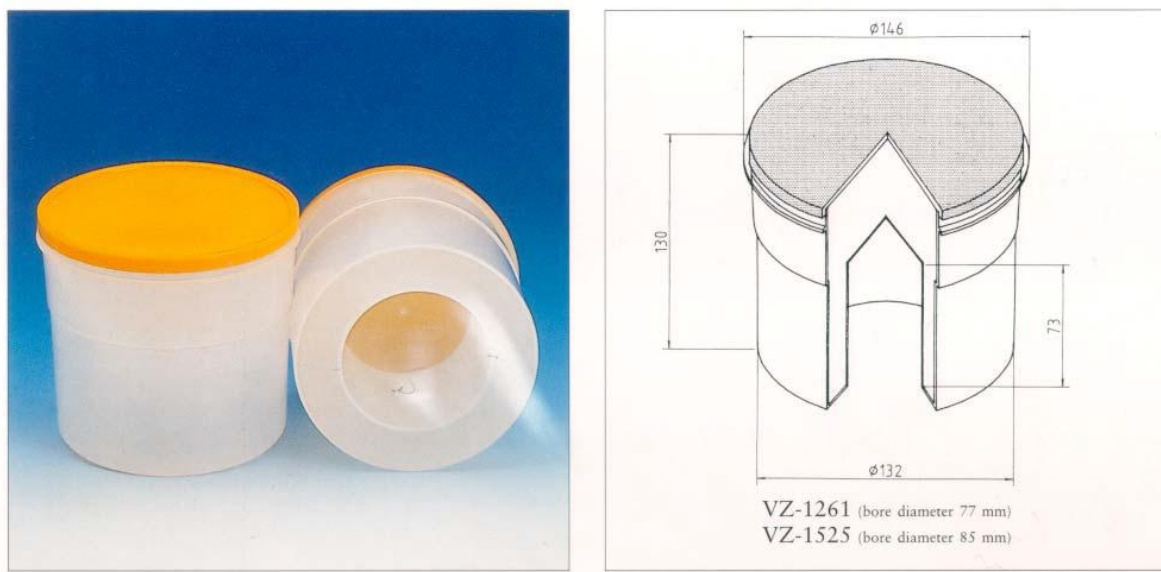


Figure 3.10: The Marinelli geometry used for measurement and a cross-section view indicating the dimensions.

3.2.1 Sand Sample

The soil sample used in this study was collected at a heavy mineral mine site. The soil was placed into a plastic bag which was sealed. This sand soil was used to prepare a reference soil sample [S13-fk-TS-0001] in a Marinelli beaker. The soil sample was dried in an oven (Labotec EcoTherm) overnight at temperature of 105°C to eliminate any moisture present. The dry soil samples were then decanted into a dry and clean Marinelli beaker, filled up to the 1 L mark and then weighed. The mass of the sample will later be used to calculate the activity concentrations of the sample. Once the soil sample was at the correct mark, a 2 mm thick lid of copper disc was placed to seal the sample. Using the silicone sealant, the copper was locked such that no air spaces exist between the sample and the outside. This was necessary, in case of radon build-up in the soil sample, there should be no escape route to the outside. Thereafter the Marinelli beaker lid was used to close the beaker, and was also sealed with the silicone sealant (see Figure 3.11). The soil sample was then stored for three weeks to attain secular equilibrium for the ^{238}U -series decay daughters, namely ^{226}Ra , ^{214}Bi and ^{214}Pb . Once the sample was counted using the HPGe system and the activity concentrations determined, it was ready to be transferred to the new counting geometry.



Figure 3.11: A typical photograph of a sealed Marinelli beaker with the soil sample inside.

3.2.2 Granite Countertops

Various granite countertops were acquired from the local supplier to be tested at the ERL laboratory. Each sample was a small rectangular block with dimensions of about $3.5 \times 14.5 \times 14.5 \text{ cm}^3$. A picture showing all the granite countertop samples used in this study is shown in Figure 3.12. The granite labels are also visible in the picture.

Considering the geometries of the granite samples, the soil sample described in subsection 3.2.1, the soil was also decanted into a new sample holder to mimic the granite samples. Figure 3.13 shows a photograph of the prepared soil sample in the new measuring geometry, similar to the granite countertop samples. Note also that the container was filled to the top and closed off with the lid, not allowing any airspace inside the container. For sealing, only the tape was used as shown.

The geometric variation between the various containers utilized in the assessment of activity concentrations for environmental measurement include the container material, dimensions and shape, as well as the filling volume within the container are presented in Table 3.6. In determining the accurate radioactivity concentration of soils, the effect of filling height should not be neglected [Abbas, 2001; Debertain, 1989]. Radionuclides exceptionally vulnerable to geometric effects are low energy gamma-emitters. When measuring such gamma-emitters, the difference in absorption for different geometric shapes can cause significant errors. Activity concentrations are also sensitive to

volumetric effects, but no volume correction was needed in this study, since the filling volume was kept uniform throughout.

Studies have shown that bulk density of characteristic mineral soils often ranges from 1.1 to 1.5 g/cm³ in surface horizons. It increases with depth and it is likely to be high in sands, and it is prone to be low in soils with rich organic matter [Guelland, 2013; Raynaud, 2014]. An average bulk density (granite countertops) of about 2.5 g/cm³ was determined which is comparable to the soil sample density of about 2.4 g/cm³, therefore the efficiency determined using the soil sample could be used for the granite samples [Zhao, 2013].

Table 3.6: Granite countertop samples physical properties; dimensions (cm), mass (kg) and their calculated bulk densities (g cm⁻³).

Sample	Dimensions (cm)	Volume (cm ³)	Mass (kg)	Density (g/cm ³)
Santa Cecelia	(3.5*14.5*14.5)	735	1.88	2.55
Namib Green	(3.5*14.5*14.5)	735	1.77	2.41
African Red	(3.5*14.5*14.5)	735	1.84	2.50
Golden Beach	(3.5*14.5*14.5)	735	1.75	2.40
Indiana Dakota	(3.5*14.5*14.5)	735	1.88	2.55
Soil	(3.5*14.5*14.5)	735	1.75	2.40
KCl	(3.5*14.5*14.5)	735	0.759	1.03



Figure 3.12: A photograph showing the granite countertops on top of each other, namely; Namib Green, Santa Cecelia, African Red, Indiana Dakota and Golden Beach in that order from top to bottom.



Figure 3.13: A photograph of the soil sample in a new measuring geometry on a mass scale sealed using tape.

3.2.3 KCl Sample

The KCl sample labeled C56-51-2 was placed in a glass bowl and oven dried in the EcoTherm LABOTEC oven overnight at 105°C to remove moisture. The KCl and glass bowl were weighed on a Sartorius scale and thereafter the KCl mass was determined by subtracting the mass of the pre-weighed bowl from the combined mass of KCl-plus-bowl system [Hlatshwayo, 2007]. The KCl sample was then removed from the oven and after cooling; the KCl sample was transferred into the one of the rectangular boxes which was sealed with a tape as shown in Figure 3.14.



Figure 3.14: Photographs showing the ERL EcoTherm oven (left-side) used in this study to dry the samples and the KCl sample in a container (right-side).

3.3 Data analysis

All the samples were measured by gamma-ray spectrometry using the ERL Hyper-Pure Germanium (HPGe) γ -ray detector system described in section 3.1. Prior to the sample measurements, a background spectrum (acquired mainly during the weekend) was recorded. The system is energy and efficiency calibrated regularly with a certified ^{232}Th ore (IAEA/RGTh-1) or any other certified reference material (e.g. liquid standard source for liquid samples) such that the centroid of the photo-peaks and the gamma-ray detection efficiency are continuously monitored. Each of the samples was counted for 24 hours using the ERL HPGe γ -ray detector and weighed with the mass scale, (SARTORIUS, model EA6DCE-I), unless stated otherwise. The test measurements were performed also to validate the calculated efficiency parameters for the gamma-ray detector using liquid (and water-equivalent) reference sources containing ^{152}Eu , ^{137}Cs and ^{60}Co radionuclides.

In this study, the efficiency calibration by Maleka (2012), as illustrated in Figure 3.4 for the 1 L Marinelli beaker geometry was used to determine the activity concentrations for the standard sources.

A background count for the box geometries was done. This background count was compared to the general background counted earlier during this study. After determining the activity concentrations of the soil sample, the box geometry efficiency calibrations were deduced as described in Section 3.1.4; these efficiencies were employed in order to find the activity concentrations of the granite countertops.

The number of counts under the full-energy peaks, the counting time, the absolute full-energy peak efficiency for the energy of interest and the γ -ray emission probability related to the different peaks, are used for the determination of the activities of specific radionuclides in the samples.

3.3.1 Activity concentration

Radionuclides present in the sample are recognised by comparing the peaks with the background spectrum which also contains the natural decay series. The full-energy peaks were seen above background, as illustrated by Figure 3.15 and for a typical counting spectrum, see also Appendix C.

Moreover, the full-energy peak efficiency was required in order to calculate the activity concentrations of the radionuclide in the samples. Activity concentrations for samples are determined as follows:

$$A_c(\text{Bq/L}) = \frac{\text{counts}}{\text{Br} \cdot \epsilon \cdot t \cdot V} \quad (3.11)$$

where A_c (in Bq/L) is the activity concentration of a specific radionuclide in a source, counts represent the full-energy peak content corrected for background contribution, Br is the branching ratio (that is the % of the decay of the nuclide that will proceed via the emission of a particular gamma-ray), ϵ is the detector efficiency at that photo-peak energy, t (in s) is the live counting time, and V (in L) is the sample volume or m (in kg) for sample mass as in the case of heavy mineral soil and granite countertops (then A_c will be in Bq/kg).

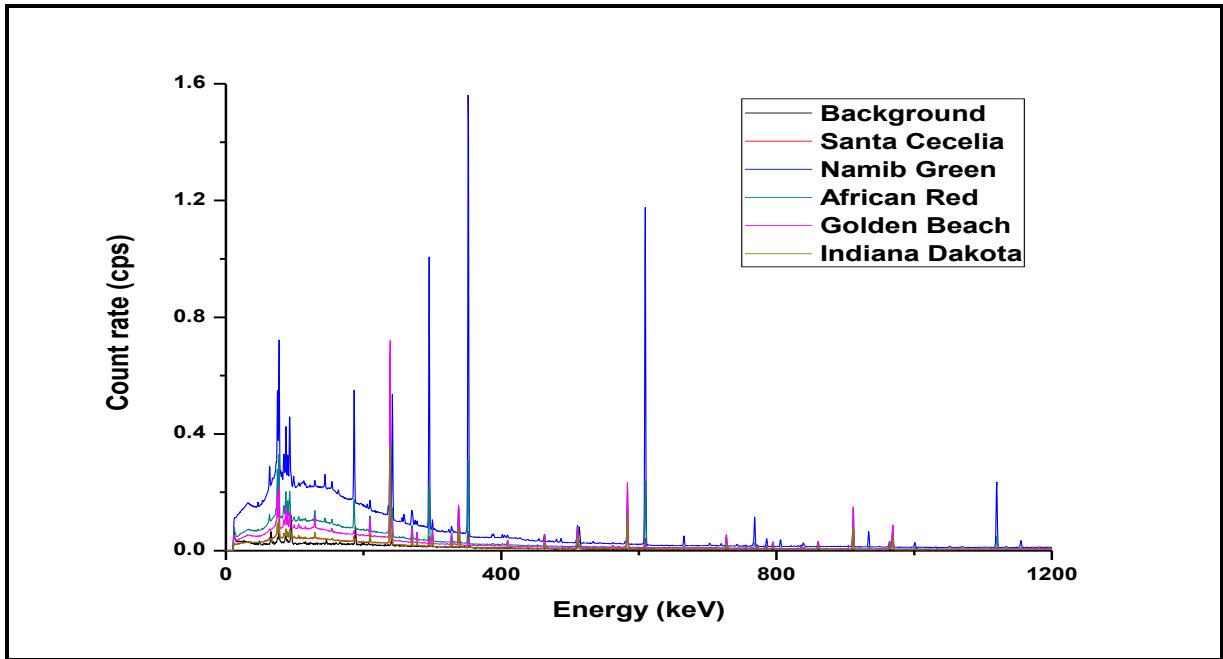


Figure 3.15: Typical measured spectra (Santa Cecelia, Namib Green, African Red, Golden Beach and Indiana Dakota) superimposed over a background spectrum to indicate relative count rates of the samples to the environmental background.

If the data set is a statistical population, meaning that it contains every possible observation and not just a subset of them, it follows that the mean of that population is called the population mean. But if the data set is a statistical sample, i.e. a subset of the population, then the statistical outcome from this assessment is called a sample mean.

Suppose we have a data set of deduced radioactivity concentrations containing the values $[a_1, \dots, a_n]$. The arithmetic mean A for these radioactivity concentrations without irresolution (or rather referred to as uncertainty) is defined as usual by the formula

$$A = \frac{1}{n} \sum_{i=1}^n a_i \quad (3.12)$$

Uncertainties in weighted mean activity concentrations A_w may be conveyed simply by stating the standard error (SE). However it is often more critical to use both A_w and SEA_w to express the uncertainty by the approximate confidence interval $A_w \pm SEA_w z^{(\alpha)}$, where $z^{(\alpha)}$ is the 100α percentile point of a standard normally distributed, where this interval would have the approximate analysis probability of $1 - 2\alpha$. 95% confidence interval implies $[\alpha = 0.025, 1 - 2\alpha = 0.95]$, and $z^{(\alpha)} = -1.96$, see Table 3.7.

Table 3.7: Z scores commonly used confidence interval [Kirkup, 1994].

Desired confidence interval	Z score
90%	1.645
95%	1.96
99%	2.576

$$A_w = \left(\sum_{i=1}^n \frac{a_i}{\sigma_i^2} \right) / \left(\sum_{i=1}^n \frac{1}{\sigma_i^2} \right) \quad (3.13)$$

where σ_i is the uncertainty in a_i .

$$A_w \pm 1.96 \left(\frac{s}{\sqrt{n}} \right) \quad (3.14)$$

The uncertainty in the weighted mean can be given by the internal uncertainty U_{int} and the external uncertainty U_{ext} .

$$U_{int} = 1 / \sum_{i=1}^n \frac{1}{\sigma_i^2} \quad (3.15)$$

$$U_{ext} = \sqrt{\chi_R^2} U_{int} \quad (3.16)$$

with the reduced chi-squared $\chi_R^2 = \frac{1}{n-1} \sum_{i=1}^n \frac{(a_i - A_w)^2}{\sigma_i^2}$. A chi-square χ^2 statistic is used to investigate whether distributions of categorical variables differ from one another. The degree of freedom is determined by subtracting 1 from the number of classes [Kirkup, 1994]. In this case, if the estimated probability is very low, then it means that there is a high chance that the study is biased.

3.3.2 Coincidence summing

All gamma-ray spectrometry laboratories plan to maintain high spectral output while ensuring low detection limits for every sample counted on their system. But this solution can be suitable only if the practical method to deduce cascade summing is possible [Sima, 2008]. The correction method for coincidence summing effects using the peak to total ratio (P/T ratio) is well established in the field of gamma-ray spectrometry [ANSI, 1999]. The method is not easy to apply to the nuclides with a complex decay scheme involving a number of γ -ray cascade transitions and large internal conversion [Lee, 2008].

Activity determination of gamma-ray emitting radionuclides in environmental samples is a difficult task, in most cases, due to the low level of activity concentration. The main problem involved with low level activity measurements is insufficient counting statistics. This could be avoided by increasing the volume of the sample and/or by performing close geometry measurements. However, in close geometry measurements, true coincidence summing effects for radionuclides with a complex decay scheme have to be taken into account [Vukanac, 2008; Plagnard, 2008].

The nuclides ^{133}Ba and ^{152}Eu are comprehensively exploited for efficiency and energy calibrations of γ -ray spectrometers, these nuclides are also measured as products throughout fission reaction from nuclear power plants. ^{133}Ba decays by electron capture (EC) to ^{133}Cs through the excited states at 383 keV (13.9%) and 437 keV (86.1%) [Bé, 2004]. The majority of γ -rays emitted from these excited states decay to the ground state by way of excited states at 81 keV. The excited state at 81 keV has an internal conversion and emits KX rays in the range from 30 keV to 36 keV. Figure 3.16 shows the complex decay scheme of ^{152}Eu which radiates at roughly 130 γ -ray energies. ^{152}Eu decays to ^{152}Sm by EC (72.1%) and to ^{152}Gd by Beta emission (27.9%). Furthermore, when ^{152}Eu decays to ^{152}Sm , KX-rays in the range from 40 keV to 50 keV are emitted by following internal conversion. This emission of X-rays, causes the correction to cascade summing to be further complicated.

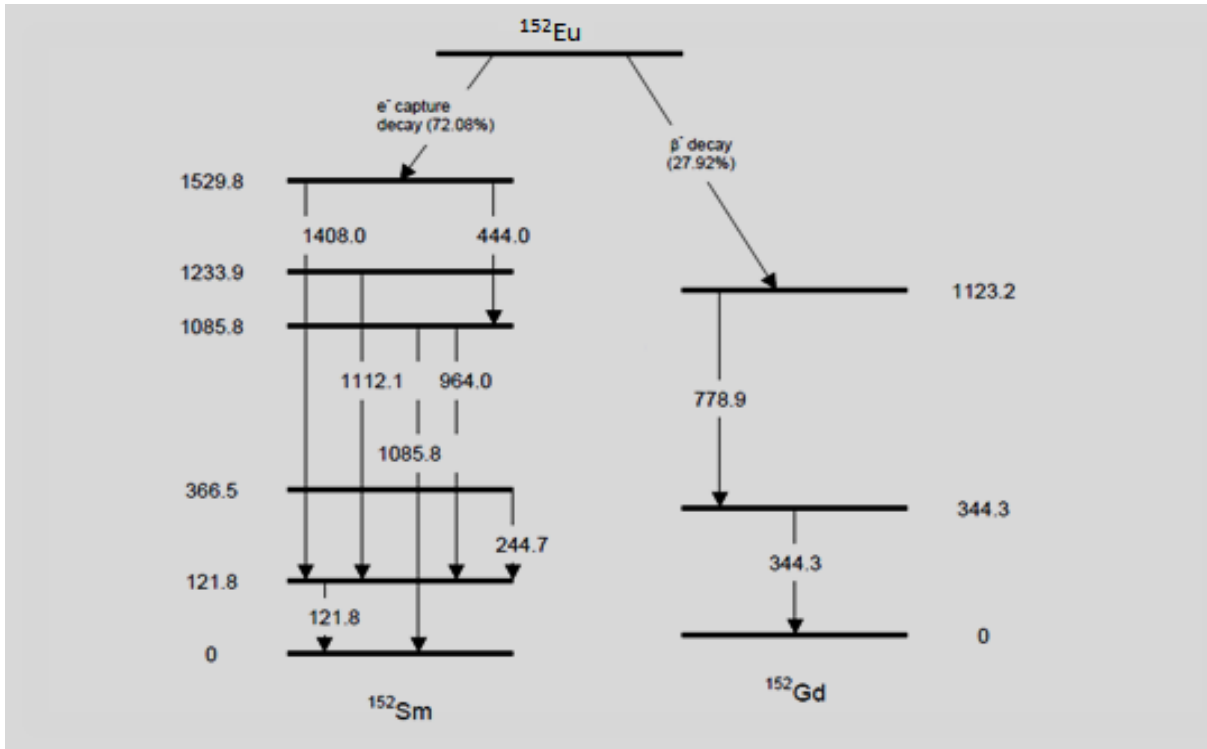


Figure 3.16: This figure depicts the simplified decay scheme of ^{152}Eu . The gamma-rays and the branching ratios are extracted from [Firestone, 1996].

Another important fission fragment is ^{137}Cs , a by-product of nuclear reactors. ^{137}Cs decays to ^{137}Ba by electron emissions (β^-); by the emission of 1174 keV (8%) to the stable isotope, and the emission of (520 keV) β^- particle (92%) which is in an excited state and decays by emitting a 662 keV gamma-ray nearly immediately to a stable state.

In addition to the full-energy peak efficiency, and by using the efficiency estimate in Figure 3.4, when radionuclides (e.g. ^{152}Eu) decay by cascading photons, the measured nuclide activity is often influenced by true coincidence summing effects. A Monte Carlo code was deployed to examine coincidence summing effects for a HPGe γ -ray detector. For this detector, absolute peak efficiency (PE) for each gamma-ray energy with given measuring conditions (geometry, density etc.) has to be known.

For this active test, the available reference source materials from CSIR and NMISA were used, see Table 3.8. If the detector is calibrated with a standard source which is similar in shape and size to that of the sample, and all the nuclides in the study are similar in the standard source and in the sample, then under those circumstances, it follows that no correction is required for true coincidence summing.

Table 3.8: Calculated efficiencies of the coincidence summing from different standard sources for ^{152}Eu measured with 1 L Marinelli beaker geometry.

Radionuclide	Energy (keV)	Measured Photo-peak Efficiency from expected A_c [Bq/l]		
		Simulated efficiency	CSIR	NMISA
^{152}Eu	121.78	0.04362	0.03771	0.03921
	244.70	0.02839	0.02875	0.02991
	344.28	0.02301	0.02527	0.02609
	411.12	0.02063	0.01919	0.02032
	444.00	0.01967	0.01882	0.01982
	778.90	0.01392	0.01359	0.01393
	867.38	0.01303	0.01160	0.01180
	964.10	0.01221	0.01193	0.01234
	1085.84	0.01134	0.01147	0.01176
	1089.74	0.01132	0.00753	0.00739
	1112.07	0.01118	0.01138	0.01169
	1212.95	0.01060	0.00930	0.00950
	1299.14	0.01016	0.00949	0.00952
	1408.01	0.00967	0.00949	0.00966

The activity of the liquid standards was mainly from ^{152}Eu . Most of the visible γ -rays are from ^{152}Eu , ^{137}Cs and ^{60}Co . Liquid solution samples were contained in 1 L Marinelli beakers. To acquire the efficiency calibration curves for CSIR and NMISA configurations, Maleka (2012) simulated efficiencies for 1 L Marinelli beaker were deployed. The radionuclides used for the calibration were ^{152}Eu , ^{137}Cs and ^{60}Co , their associated emissions from nuclides covering the range 121 keV to 1408 keV. The resulting efficiency curve shown in Figure 3.17 was used to calculate the activities of the samples used in the test of coincidence summing, mainly focusing only on the ^{152}Eu radionuclide (in both CSIR and NMISA reference sources).

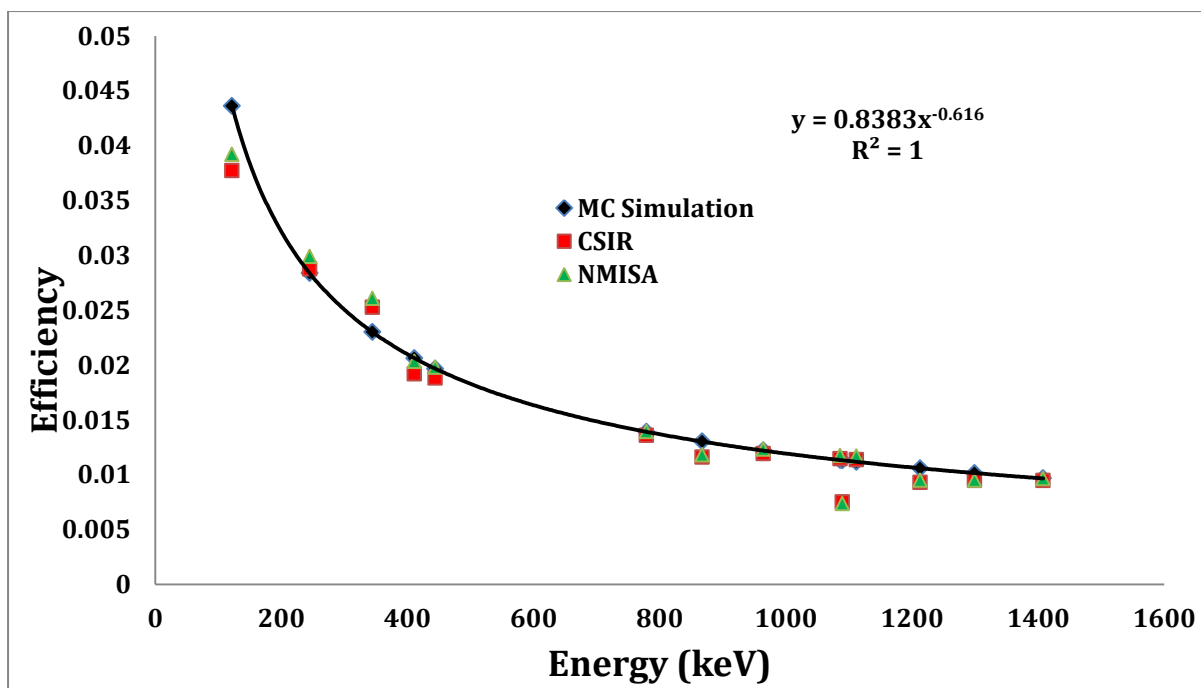


Figure 3.17: Efficiency calibration curve following Maleka's (2012) efficiency fit for 1 L Marinelli beaker geometry and the measured efficiencies from different standard sources for ^{152}Eu measured with 1 L Marinelli beaker geometry. The effect of coincidence summing is clear for several of the peaks.

The expected activity concentration of ^{152}Eu found in the CSIR and NMISA samples was 3689 ± 110 and 5693 ± 159 Bq/L, respectively (see also Figure 3.18 and Figure 3.19), Unc + and Unc - shows the width of 1σ standard deviation. The expected activity concentration of ^{137}Cs was 511 ± 10 and 583 ± 17 Bq/L, and for the ^{60}Co was 437 ± 9 and 1339 ± 37 Bq/L for the CSIR and NMISA samples, respectively.

Most gamma-ray lines are consistent with the expected activity concentration values, but some show clear indication of coincidence summing such as the 1089 keV line which is off by 30 %. The data for the 1086 and 1408 keV lines are consistent with results from [Lee, 2008]: i.e. less expected influence of coincidence summing. The measured value at 344 keV is consistently higher than the simulated value by about 10%, which cannot be due to coincidence summing. Further investigation is required.

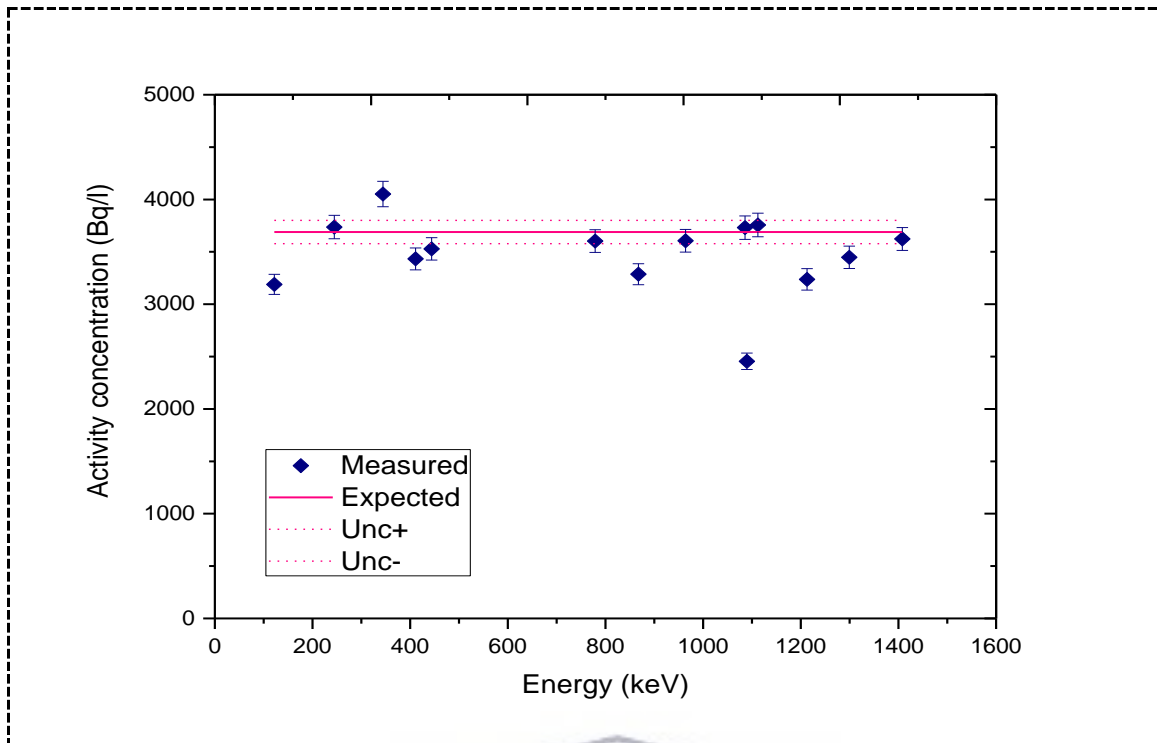


Figure 3.18: Figure showing the calculated activity concentration (Bq/L) as a function of Energy (keV) for the ^{152}Eu radionuclide found in reference sources from CSIR. Unc+ and Unc- indicate 1σ deviation from the expected values.

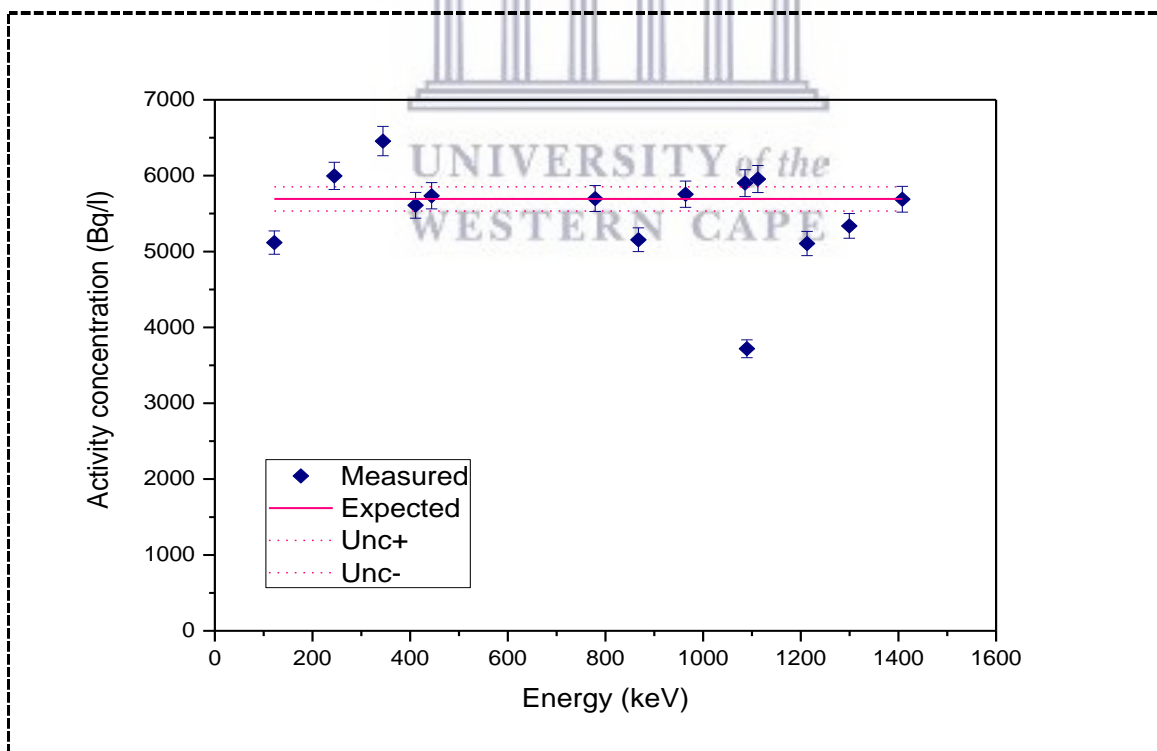


Figure 3.19: Figure showing the calculated activity concentration (Bq/L) as a function of Energy (keV) for the ^{152}Eu radionuclide found in reference sources from NMISA. Unc+ and Unc- indicate 1σ deviation from the expected values.

Chapter 4

RESULTS AND DISCUSSION

The main purpose of this study was to measure the activity concentration levels of the following primordial radionuclides; the ^{238}U -series, ^{232}Th -series and ^{40}K in granite countertops and to assess radiological hazards. The analysis of the radionuclide contents and the determination of the corresponding activity concentrations and absorbed dose rates in the samples are presented and discussed in this chapter.

4.1 ^{232}Th and ^{238}U

The distributions of the radioactivity measured in all countertops studied are presented in this chapter. The radioactivity concentrations of ^{238}U , ^{232}Th and ^{40}K found in each sample varied greatly from one granite sample to another.

4.1.1 ^{232}Th

The activity concentration of ^{232}Th is determined using its progenies (see also Fig. 2.5). Using the gamma-ray spectrometry technique, only gamma emitting radionuclides in the series are considered, moreover the system should be in secular equilibrium. In nature this is not always the case for ^{232}Th [Chu and Wang, 1997] but the determination of ^{228}Ra can be done from ^{228}Ac , and of ^{228}Th from its progeny ^{212}Pb , ^{212}Bi and ^{208}Tl .

The activity concentrations of ^{232}Th (Bq/kg) and their respective weighted means (highlighted by solid red lines) for the granite countertops used in this study are presented in Figure 4.1 to 4.5. Most of the intense γ lines which can be used for the analysis have energies that lie between 238 keV and 2614 keV. The results also indicate that the γ -line of ^{208}Tl at 2614 keV always exhibit the lowest activity concentration compared to other ^{232}Th progenies in all granite samples. This observation may be linked to the gamma-ray line emission at 583.3 keV (^{208}Tl) which is associated with coincidence summing, since it is always followed by an emission of a γ -ray at 2614 keV. Furthermore, it is often in coincidence summing with other emissions since the beta branching ratio of the level is only about half of its depopulating intensity [Talavera, 2000].

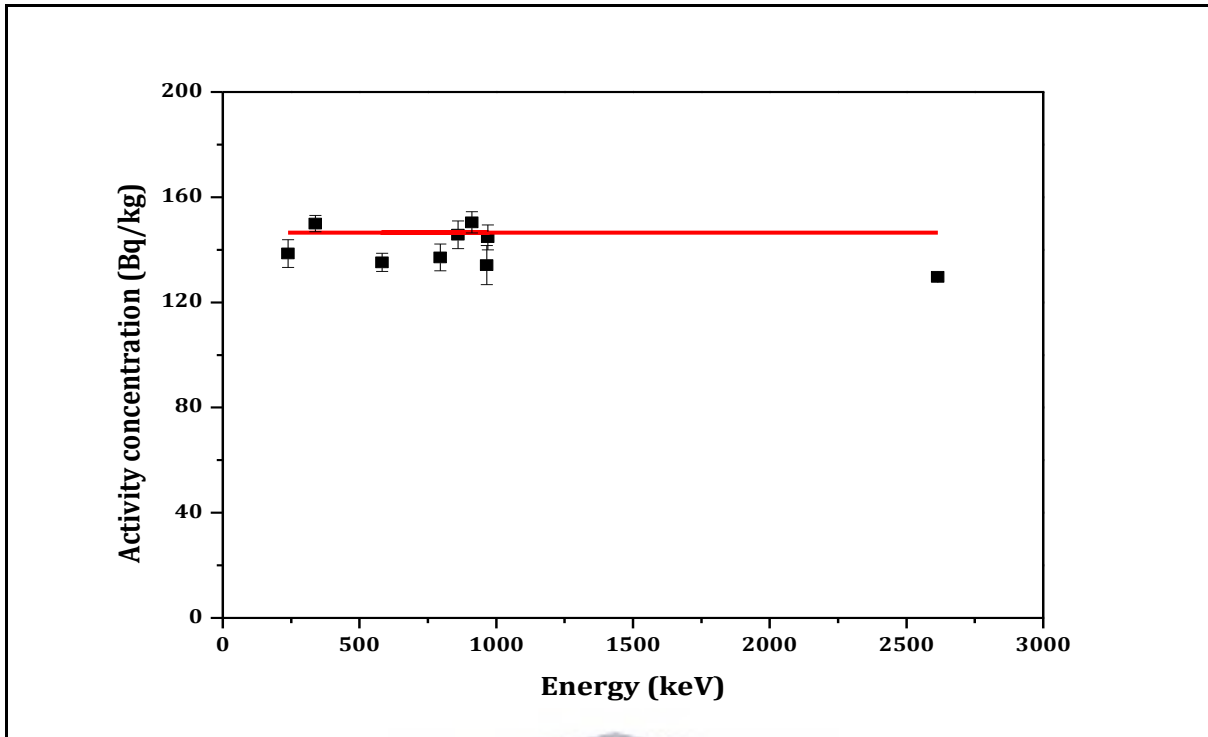


Figure 4.1: Activity levels of ^{232}Th as measured from the **AR sample**. These activity levels were calculated using individual γ lines from ^{228}Ac , ^{212}Pb , ^{212}Bi and ^{208}Tl in the ^{232}Th decay chain. The weighted mean is indicated by the line.

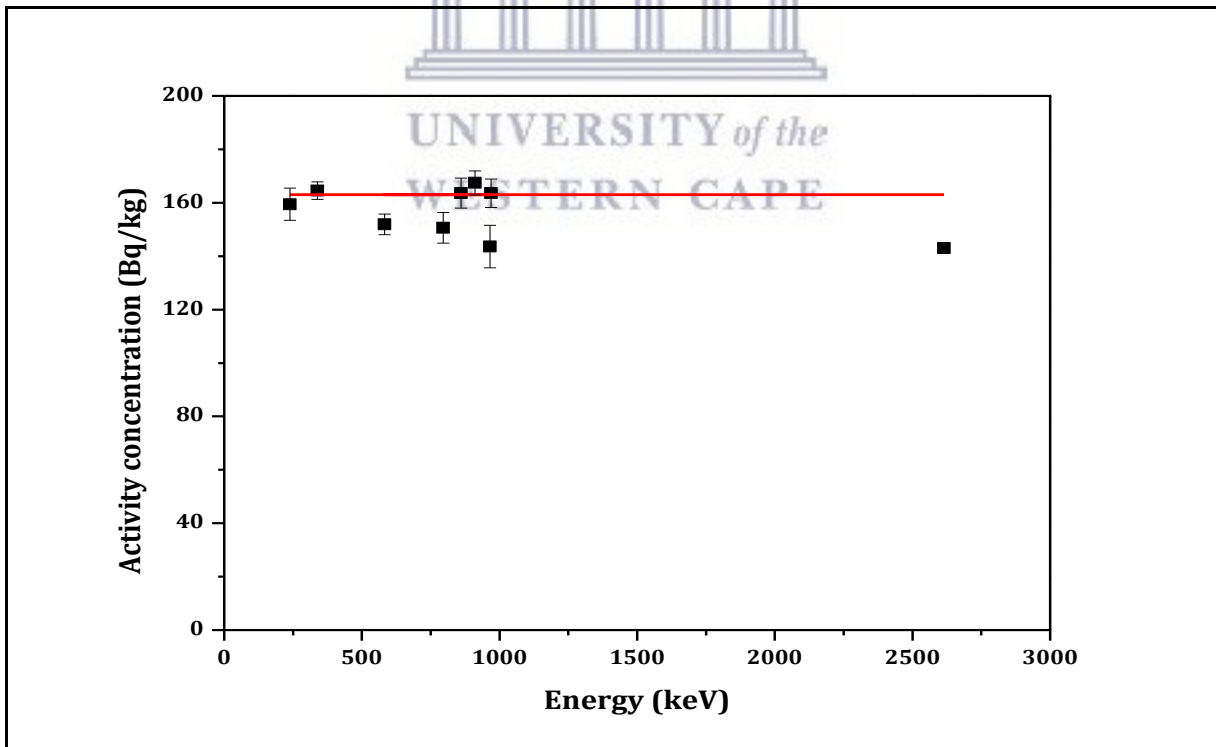


Figure 4.2: Activity levels of ^{232}Th as measured from the **GB sample**. These activity levels were calculated using individual γ lines from ^{228}Ac , ^{212}Pb , ^{212}Bi and ^{208}Tl in ^{232}Th decay chain. The weighted mean is indicated by the line.

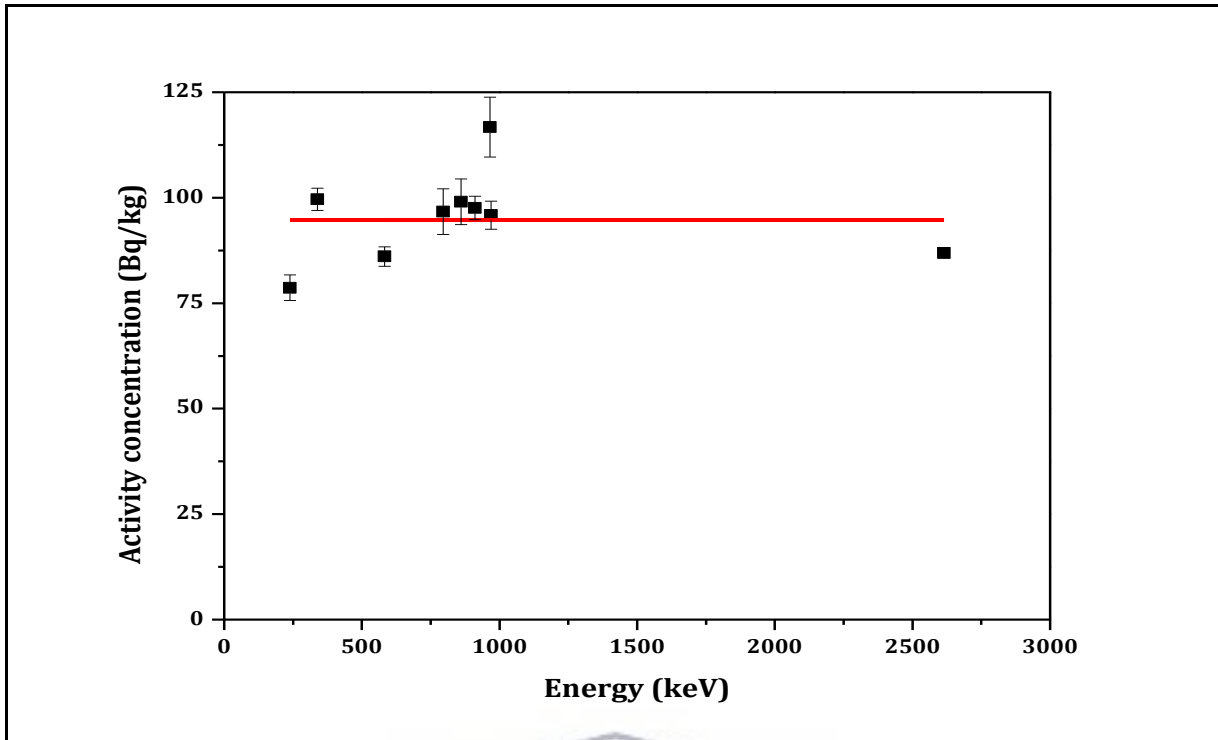


Figure 4.3: Activity levels of ^{232}Th as measured from the **NG sample**. These activity levels were calculated using individual γ lines from ^{228}Ac , ^{212}Pb , ^{212}Bi and ^{208}Tl in ^{232}Th decay chain. The weighted mean is indicated by the line.

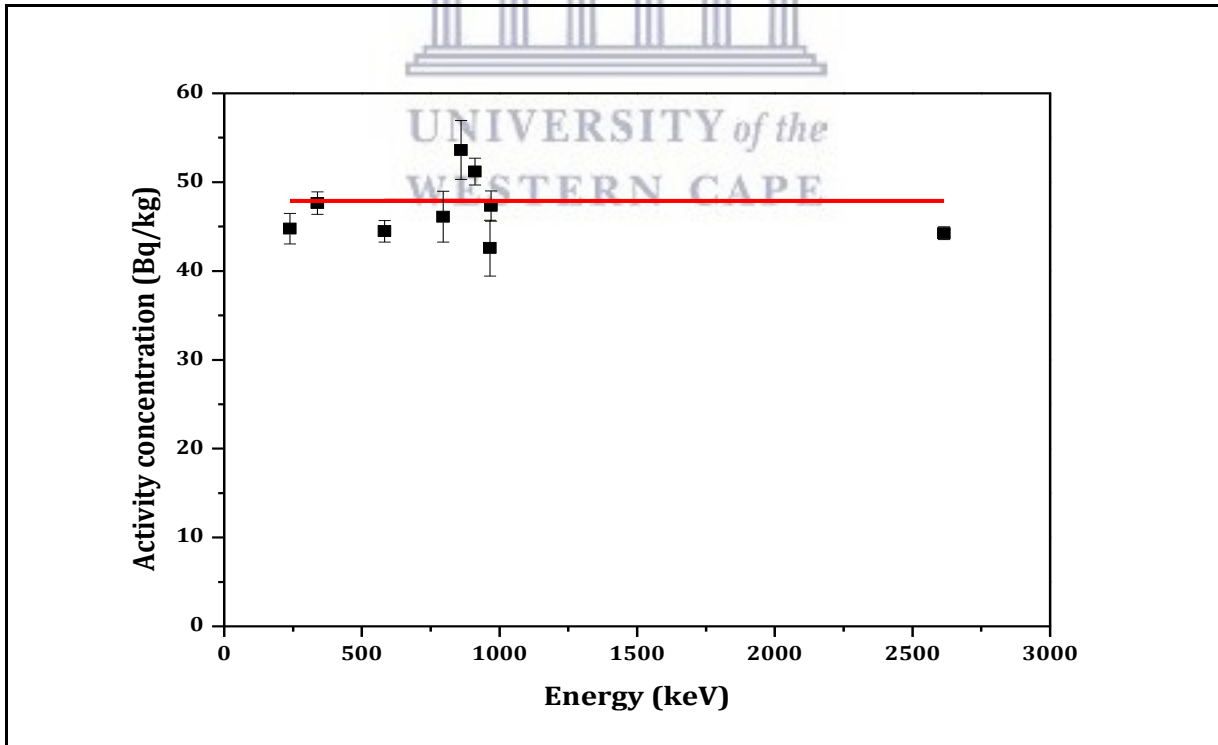


Figure 4.4: Activity levels of ^{232}Th as measured from the **SC sample**. These activity levels were calculated using individual γ lines from ^{228}Ac , ^{212}Pb , ^{212}Bi and ^{208}Tl in ^{232}Th decay chain. The weighted mean is indicated by the line.

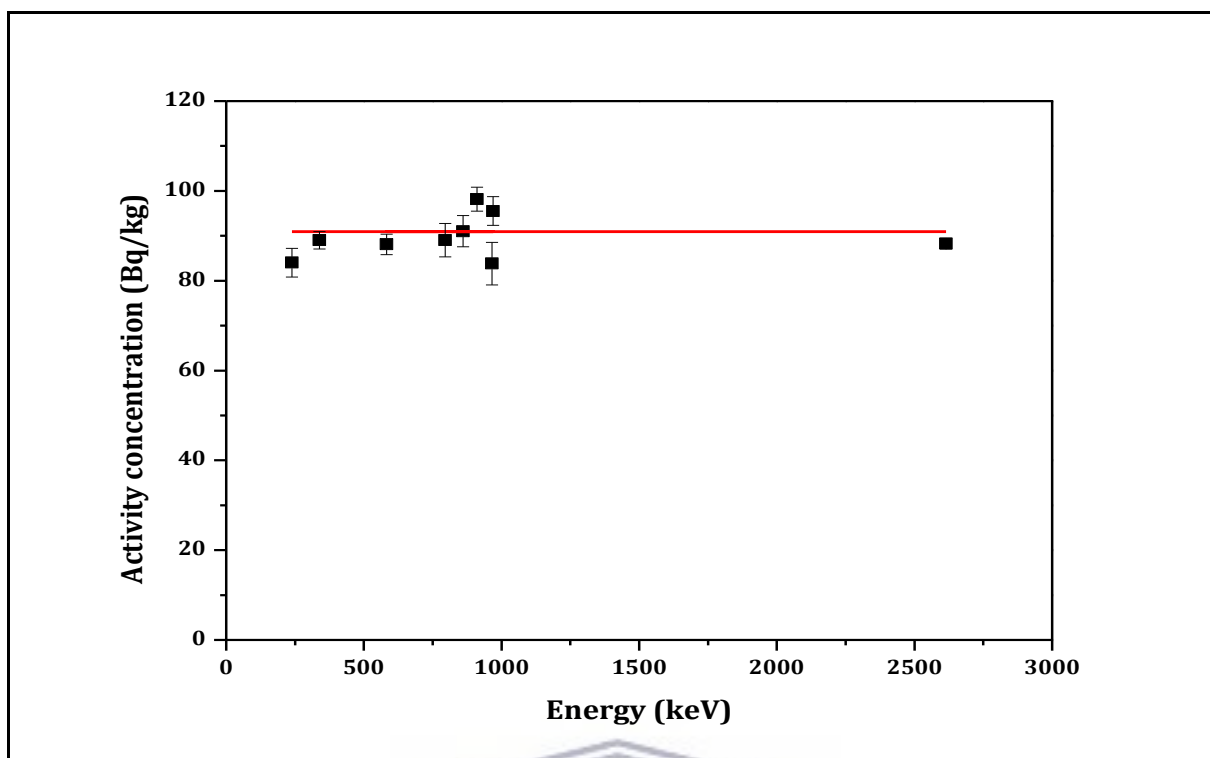


Figure 4.5: Activity levels of ^{232}Th as measured from the **ID sample**. These activity levels were calculated using individual γ lines from ^{228}Ac , ^{212}Pb , ^{212}Bi and ^{208}Tl in ^{232}Th decay chain. The weighted mean is indicated by the line.

Table 4.1 presents the range from low to high activity concentrations with their respective mean (weighted) activity concentrations for thorium available in each countertop sample. Also the reduced chi-squared values for each sample is shown, hence most of the uncertainties reported for the weighted average values are external.

Table 4.1: Average thorium activity concentration available in each granite countertop sample, with respective low and high activity levels measured. The uncertainties indicated are at the 1σ level.

Sample	Lowest A_c (Bq/kg)	Highest A_c (Bq/kg)	Mean A_c (Bq/kg)	χ_R^2
SC	43 ± 3	54 ± 3	47.8 ± 1.2	2.8
NG	79 ± 3	117 ± 7	95 ± 4	8.6
AR	134 ± 7	150 ± 4	147 ± 2	1.5
GB	144 ± 8	167 ± 5	163 ± 3	1.5
ID	84 ± 5	98 ± 3	91 ± 2	3.4

4.1.2 ^{238}U

The activity concentrations calculated using the γ -rays in the ^{238}U decay series with their respective weighted means for the granite countertops studied are presented in Figures 4.6 to 4.9. Most γ lines within each sample are in agreement, especially activity concentrations from Santa Cecelia with an average activity of 19.4 ± 0.6 Bq/kg. The other figures indicate many lines which are more than one standard deviation from the average. Table 4.2 presents the range of activity concentrations of ^{238}U in the countertops which varies from below detection limit and/or rather **Minimum Detectable Activity (MDA)** (< 3.0 Bq/kg) to the high values as reported in the table.

Table 4.2: Average uranium activity concentration in each granite countertop sample, with respective low and high activity levels measured.

Sample	Lowest A_c (Bq/kg)	Highest A_c (Bq/kg)	Mean A_c (Bq/kg)	χ_R^2
SC	18.2 ± 1.8	25 ± 3	19.4 ± 0.6	1.1
NG	564 ± 14	642 ± 15	604 ± 11	2.8
AR	99 ± 4	164 ± 17	107 ± 4	4.0
GB	3 ± 11	11 ± 3	7.9 ± 0.5	1.2
ID	< MDA	7 ± 3	4 ± 3	1.1

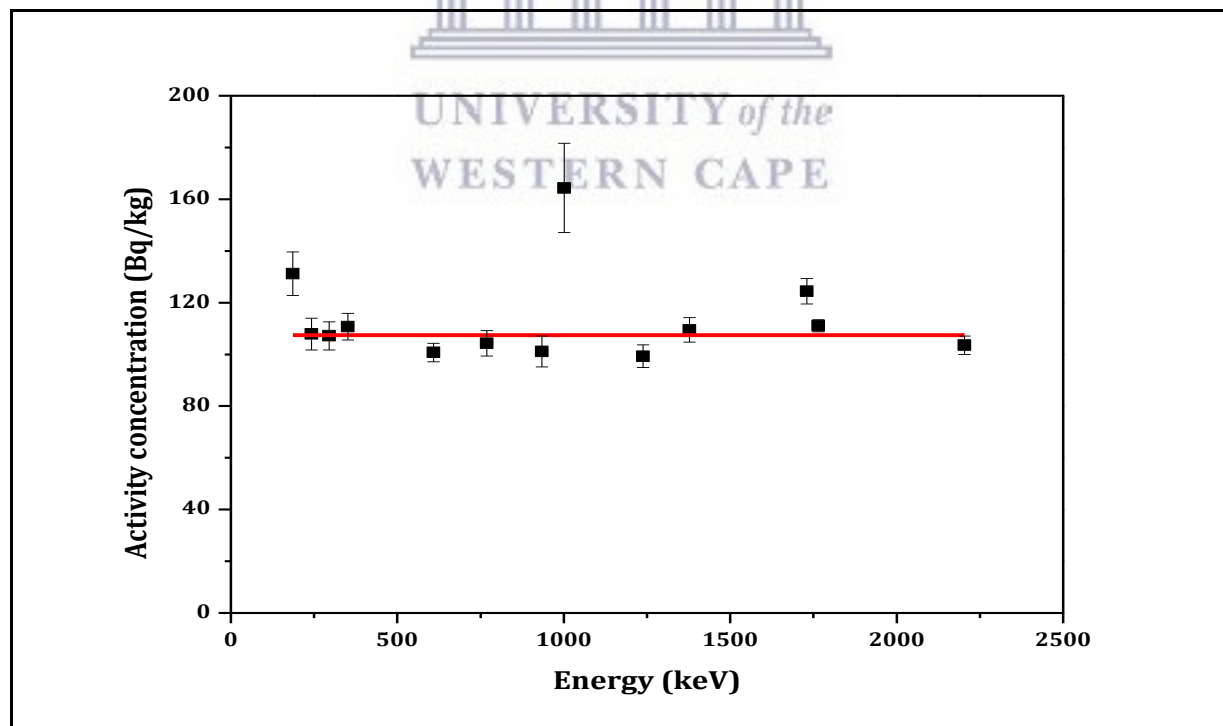


Figure 4.6: Activity levels of ^{238}U as measured from the **AR** sample. These activity levels were calculated using individual γ lines from ^{234}Pa , ^{226}Ra , ^{214}Pb , and ^{214}Bi in ^{238}U decay chain. The weighted mean is indicated by the line.

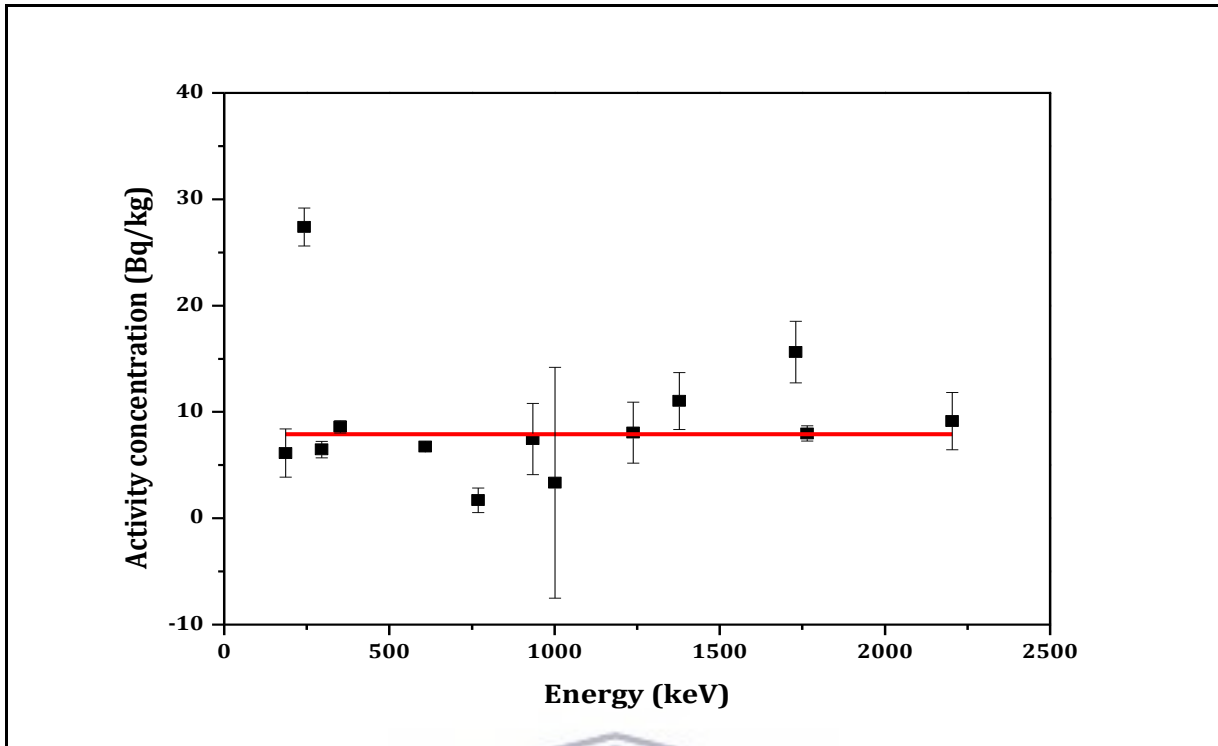


Figure 4.7: Activity levels of ^{238}U as measured from the **GB** sample. These activity levels were calculated using individual γ lines from ^{234}Pa , ^{226}Ra , ^{214}Pb , and ^{214}Bi in ^{238}U decay chain. The weighted mean is indicated by the line.

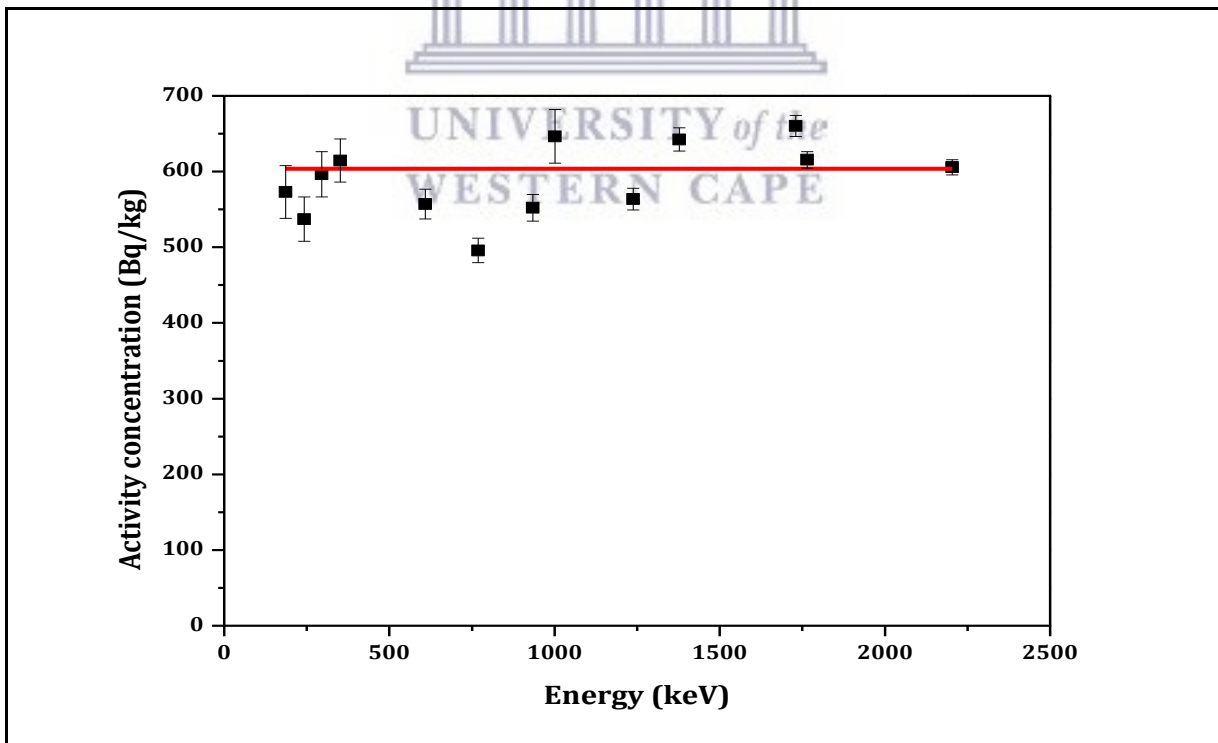


Figure 4.8: Activity levels of ^{238}U as measured from the **NG** sample. These activity levels were calculated using individual γ lines from ^{234}Pa , ^{226}Ra , ^{214}Pb , and ^{214}Bi in ^{238}U decay chain. The weighted mean is indicated by the line.

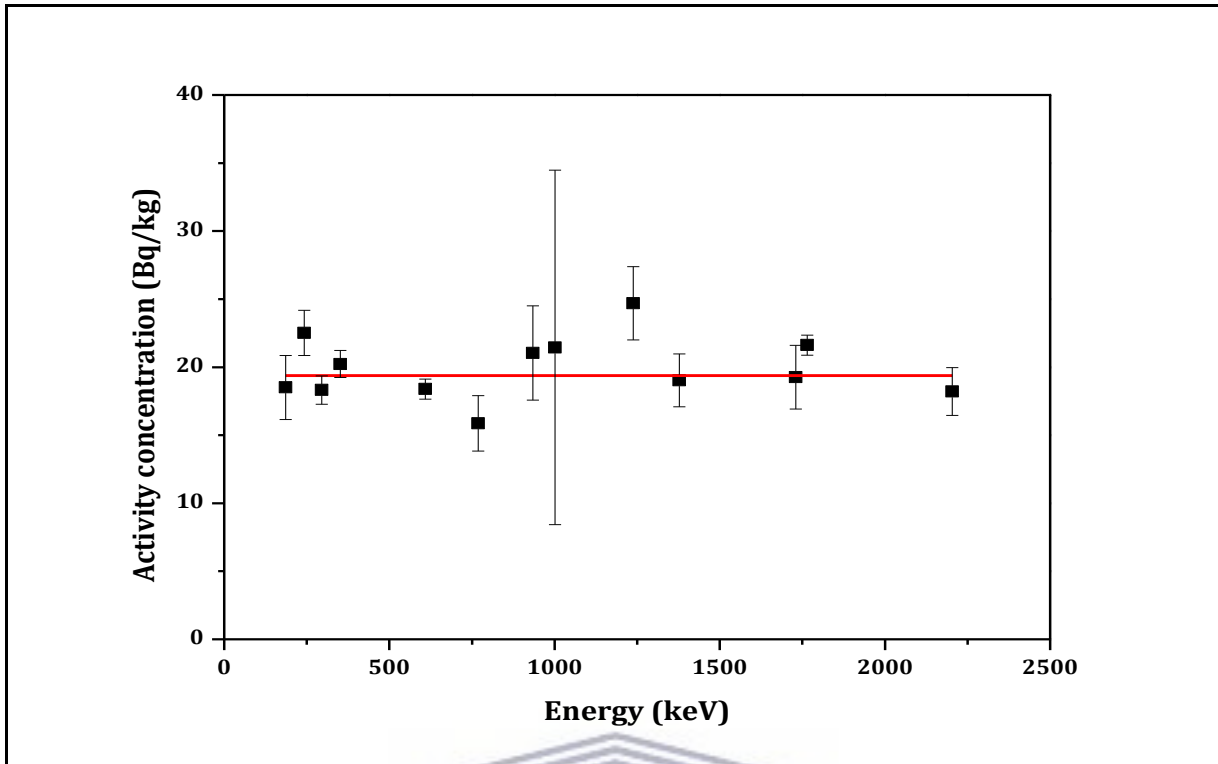


Figure 4.9: Activity levels of ^{238}U as measured from the **SC** sample. These activity levels were calculated using individual γ lines from ^{234}Pa , ^{226}Ra , ^{214}Pb , and ^{214}Bi in ^{238}U decay chain. The weighted mean is indicated by the line.

The parent in the decay chain, ^{238}U , does not yield any important γ lines, and approximation of its activity has to be done by means of its progenies ^{234}Th and $^{234\text{m}}\text{Pa}$, both of which reach secular equilibrium with ^{238}U within the period of 120 days in a closed system. Amidst the emissions of ^{234}Th , the 63.3 keV photon is the most suitable for activity determination [Talavera, 2000], but was not used in this work because of efficiency calibration problems at such low energies. Likewise the emissions from ^{214}Pb and ^{214}Bi soon reach secular equilibrium with ^{226}Ra within 30 days due to their short half-lives but since the samples in this study were not sealed, ^{222}Rn could escape. For ^{214}Pb the predominant γ line is 351.9 keV, and this is not expected to need special correction [Talavera, 2000]. The activity concentrations using the $^{234\text{m}}\text{Pa}$ gamma-ray line showed much inconsistency from one sample to the next, and it was assumed this was due to the low branching ratio (0.84%) for this gamma-line resulting in a low intensity and also the effect of background.

4.2 Testing secular equilibrium

In this study the existence of secular equilibrium was tested between ^{238}U and all its progenies. The energy transitions used (branching ratios given in bracket) are 186 keV (6.17 %) of the ^{226}Ra isotope, and 1001 keV (0.84 %) of the ^{234}Pa isotope prior to ^{222}Rn decay and compared to 241 keV (7.5 %), 295 keV (18.5 %) and 351 keV (35.8 %) of the isotope ^{214}Pb and 609 keV (44.8 %), 768 keV (4.8 %), 934 keV (3.03 %), 1120 keV (14.8 %), 1238 keV (5.9 %), 1377 keV (3.9 %), 1729 keV (2.9 %), 1764 keV (15.4 %) and 2204 keV (4.9 %) of the isotope ^{214}Bi succeeding ^{222}Rn decay.

From Table 4.3, it is clear that of 5 granite countertop samples, not all samples are in secular equilibrium. The activity concentration for the radionuclides ^{214}Pb and ^{214}Bi clearly indicate whether or not the system was in secular equilibrium when compared to ^{234}Pa and ^{226}Ra activity levels. Both the ^{234}Pa and ^{226}Ra , with relatively low branching ratios also requires careful analysis for samples with expected low activity concentrations of ^{238}U . Note also that the results as discussed above and below, did not discard the gamma-ray lines that are considered to be prone to coincidence summing according to Newman (2008).

Table 4.3: Activity concentration (Bq/kg) of radionuclides from ^{238}U series before radon decay and after radon decay.

Sample	A (Bq/kg) Before ^{222}Rn		Average	A (Bq/kg) After ^{222}Rn		Average
	^{234}Pa	^{226}Ra		^{214}Pb	^{214}Bi	
SC	21 ± 13	19 ± 2	20 ± 8	20 ± 2	20 ± 3	20 ± 2
NG	650 ± 40	570 ± 40	610 ± 40	580 ± 40	590 ± 50	590 ± 50
AR	164 ± 17	131 ± 8	148 ± 13	109 ± 2	107 ± 8	108 ± 5
GB	3 ± 11	6 ± 2	5 ± 7	14 ± 12	9 ± 4	11 ± 8
ID	< MDA	< MDA	< MDA	< MDA	< MDA	< MDA

Figures 4.10 and 4.11 show the plot of the radionuclides before (^{234}Pa and ^{226}Ra) and after (^{214}Pb and ^{214}Bi) radon decay as compared to the calculated average concentration of ^{238}U in the Santa Cecelia (SC) and African Red (AR) samples, respectively. Data in Figure 4.10 shows secular equilibrium, while in Figure 4.11 the secular equilibrium was clearly broken. This is probably due to radon (^{222}Rn) escape in the African Red sample whereas there is no indication of this effect in the Santa Cecelia sample. The data in Table 4.3 above and the presentations in Figures 4.10 - 4.11, show that a different approach should be adopted in the future for similar measurements. One possibility

required that all samples are prepared in a sealed container to avoid any radon loss or another possibility samples would be to crush the sample and prepared in the available Marinelli geometry with the normal standard procedures.

Table 4.3 indicates that the NG sample has by far the highest ^{238}U activity concentrations but the AR sample may have the largest ^{222}Rn escape. This was borne out by ^{222}Rn measurements [Wentzel, MSc in progress].

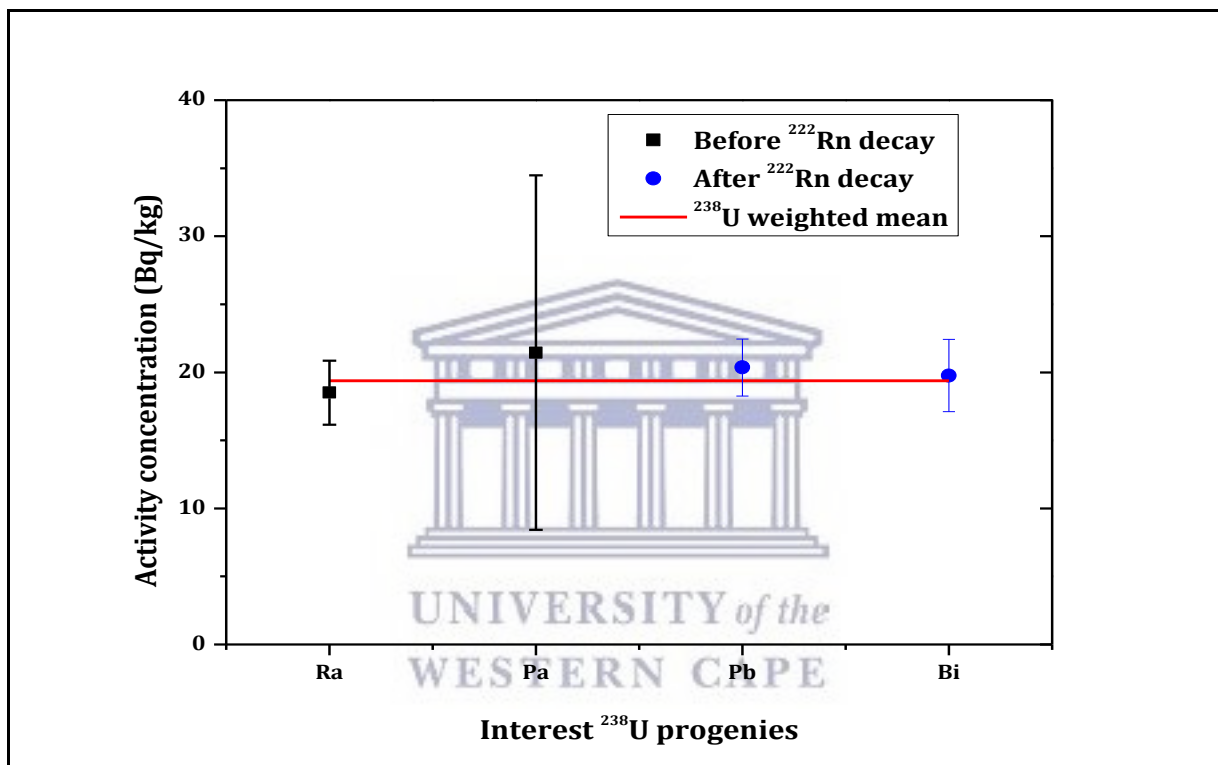


Figure 4.10: Activity concentration (Bq/kg) of interest radionuclides from ^{238}U before radon escape and after radon escape in the SC sample.

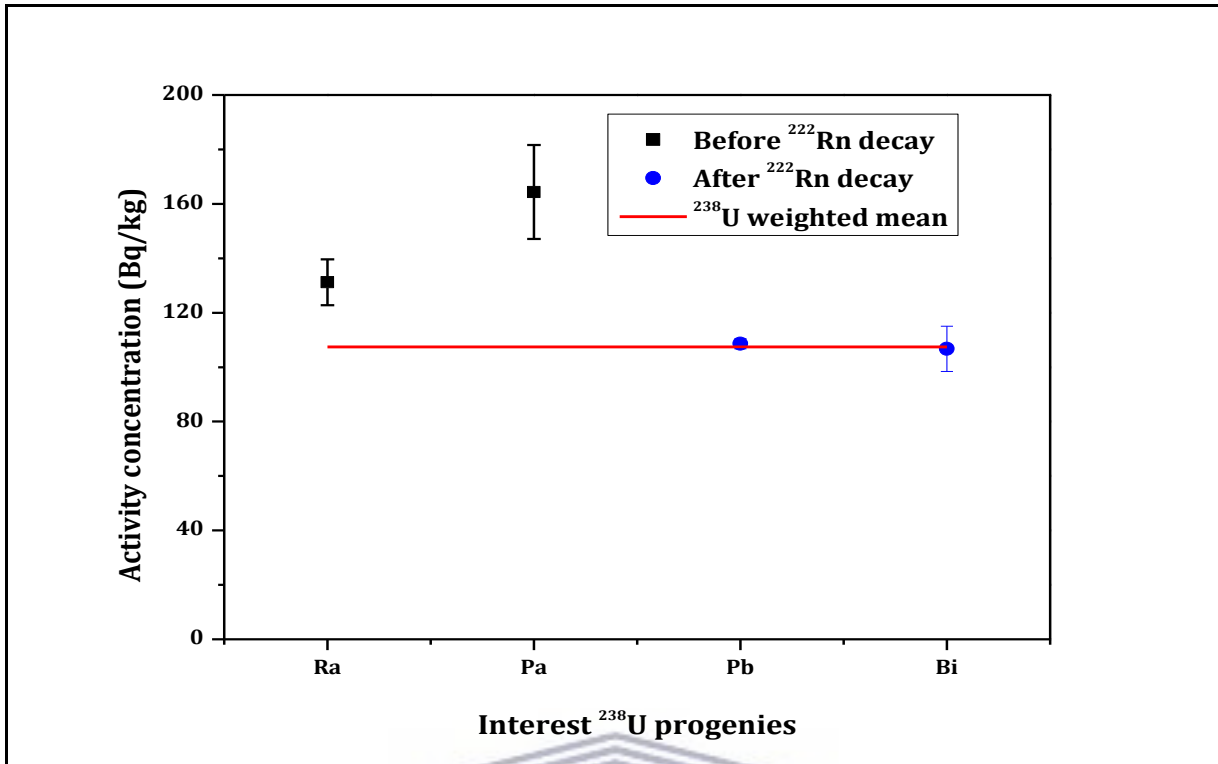


Figure 4.11: Activity concentration (Bq/kg) of radionuclides from the ²³⁸U decay series before radon escape and after radon escape in the AR sample.

4.3 Correlation between ²³⁸U/²³²Th and ²³⁸U

Figure 4.12 presents a graph plotted between ²³⁸U/²³²Th activity ratios with the ²³⁸U activity concentration. The relation between the ratio and the ²³⁸U activity can be expressed mathematically by a linear function, as follows:

$$y = a + bx \quad (4.1)$$

where y is the activity ratio, x is the activity concentration of ²³⁸U radionuclide in the countertops, and a and b are parameters. By deploying the above equation, the following function is obtained:

$$^{238}\text{U}/^{232}\text{Th} = -0.03307 + 0.00929 (^{238}\text{U conc.}) \quad (4.2)$$

with a coefficient of determination $R^2 = 0.99$. This correlation reflects that the activity ratio ²³⁸U/²³²Th changes linearly with ²³⁸U concentration. It is clearly difficult to predict what could happen at low activity concentration. More statistics is required to quantify the uncertainty and to predict how the linear function will unfold over a range of data points.

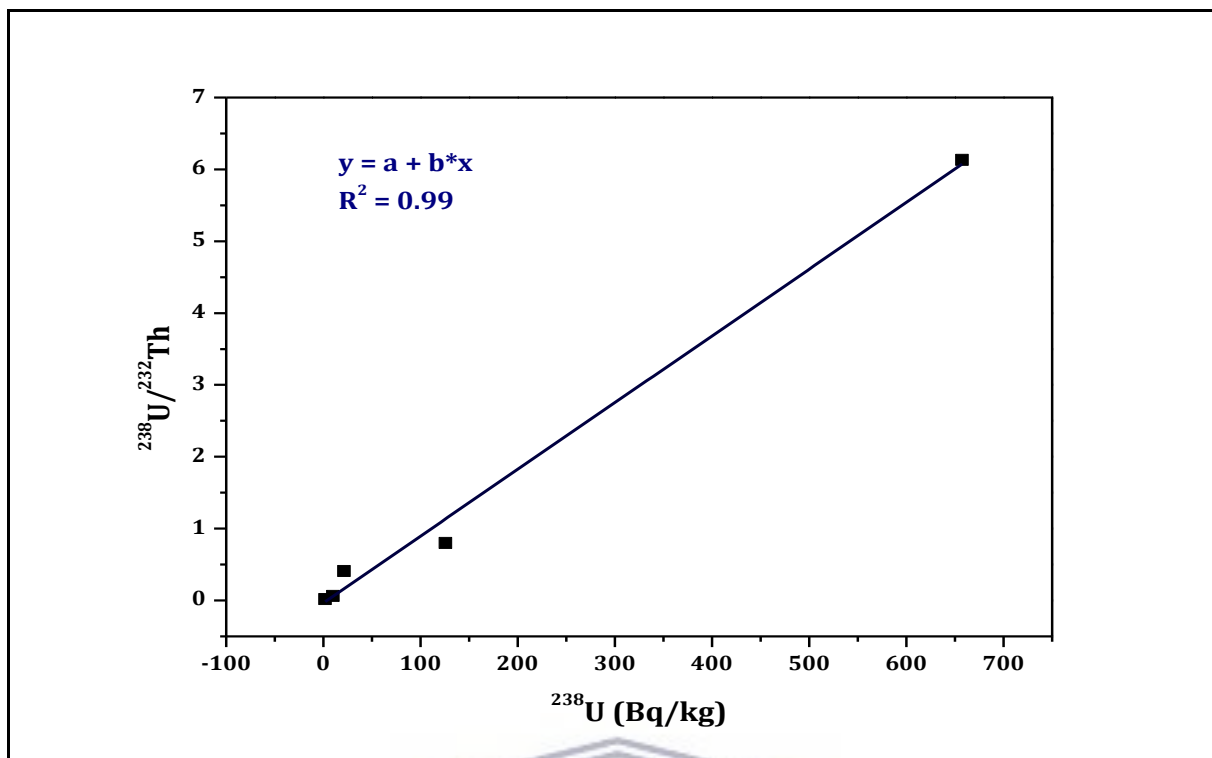


Figure 4.12: A linear function fitted between $^{238}\text{U}/^{232}\text{Th}$ and ^{238}U (Bq/kg) that indicates a linear relationship.

While comparing radionuclides from diverse decay chains ($^{238}\text{U}/^{232}\text{Th}$ and ^{238}U), it was perceived that both series are linearly related i.e. the concentration of the $^{238}\text{U}/^{232}\text{Th}$ ratio increases with an increase of ^{238}U series. And one might expect that the concentration of the ^{238}U series will increase with an increase in ^{232}Th , however, that is not quite the case. Since the y-intercept is not far away from zero, this could imply that the $^{238}\text{U}/^{232}\text{Th}$ activity ratio is uniform for the countertops.

4.4 Comparison of ^{238}U , ^{232}Th and ^{40}K

Table 4.4 present the average activity concentrations of the three radionuclides to be discussed. Figures 4.13 - 4.15 show the comparison of ^{238}U , ^{232}Th and ^{40}K activity concentration (Bq/kg) respectively of various granite countertop samples. As shown in Figure 4.13 (and Table 4.4), the activity concentrations of ^{238}U (range 3.9 – 603 Bq/kg) in the samples differ greatly; the levels are high in the Namib Green (NG) sample and fairly low in the Indiana Dakota (ID) sample. The pattern is different for the ^{232}Th activity concentration (range 47.9 – 163 Bq/kg) as shown in Figure 4.14 and Table 4.4. The activity concentration of ^{40}K (range 1447 – 1958 Bq/kg) is shown in Figure 4.15.

Table 4.4: Average activity concentrations for the five granite countertop samples

Sample	Average activity concentration (Bq/kg)		
	$^{238}\text{U}^*$	^{232}Th	^{40}K
SC	19.4 ± 0.6	47.8 ± 1.2	1550 ± 30
NG	604 ± 11	95 ± 4	1960 ± 40
AR	107 ± 4	147 ± 2	1550 ± 30
GB	7.9 ± 0.5	163 ± 3	1920 ± 40
ID	4 ± 3	91 ± 2	1450 ± 30

*Note: ^{238}U value presented in the table did not correct for secular equilibrium effect.

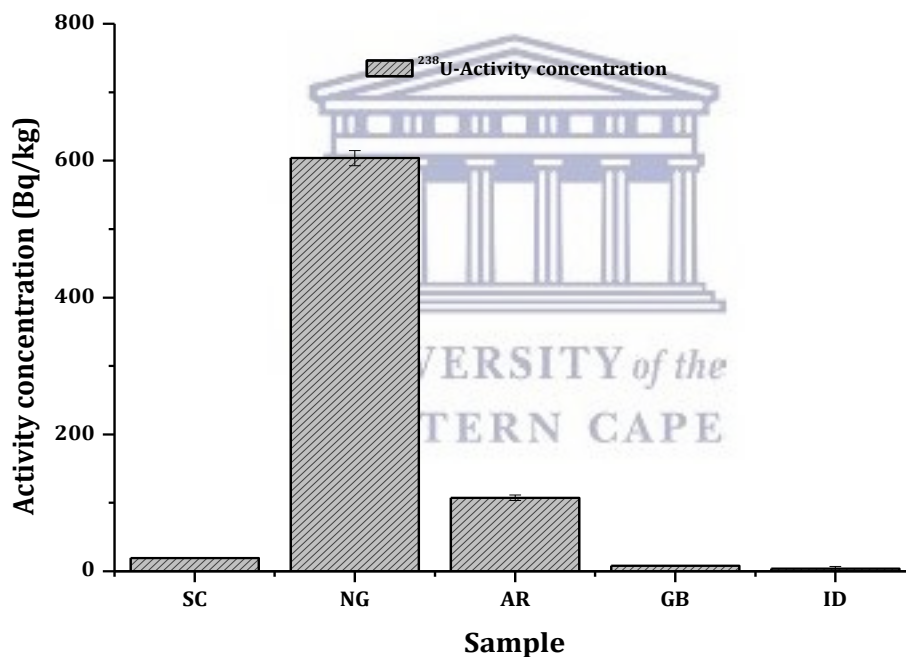


Figure 4.13: Comparison of ^{238}U activity concentration (Bq/kg) of various granite countertop samples.

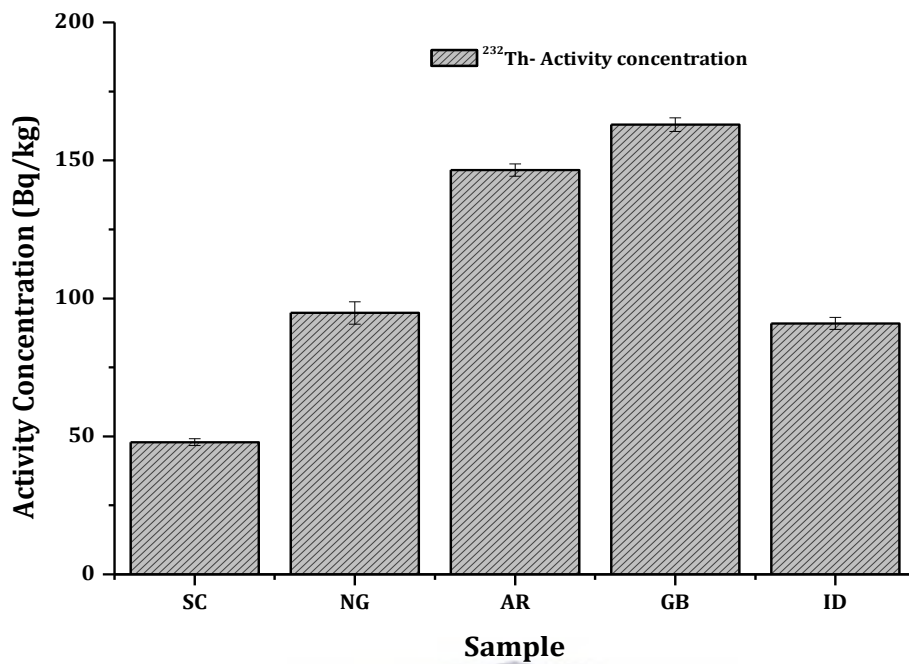


Figure 4.14: Comparison of ^{232}Th activity concentration (Bq/kg) of various granite countertop samples.

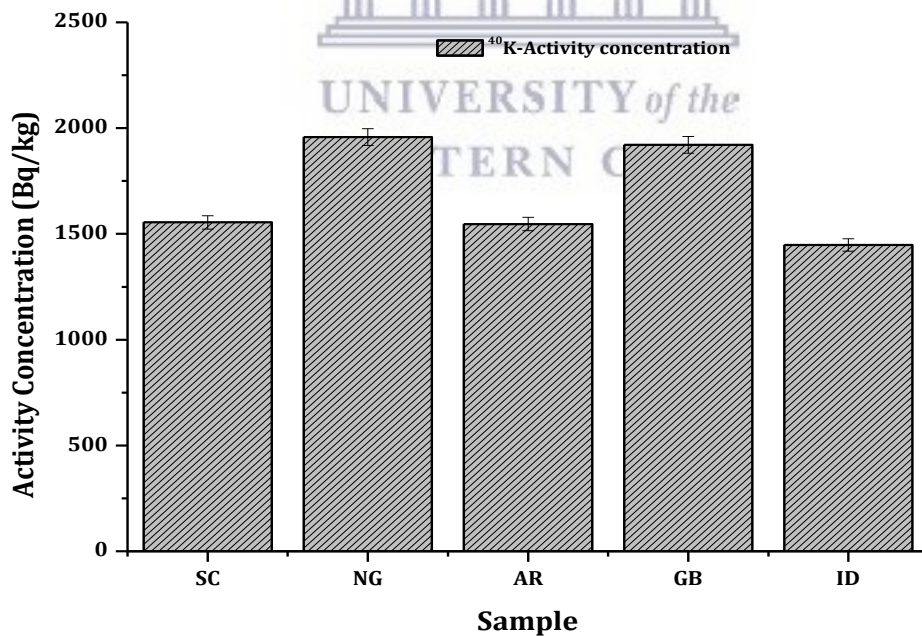


Figure 4.15: Comparison of ^{40}K activity concentration (Bq/kg) of various granite countertop samples.

Gamma-ray spectrometry has been used to determine the activity concentration levels in 5 granite countertop samples. The activity profile of radionuclides has clearly showed the existence of a large range of radioactive activity levels in different samples. The range of activity concentrations found was [3 – 610 Bq/kg] for ^{238}U series, (47 – 165 Bq/kg) for ^{232}Th series, and (1400 – 2000 Bq/kg) for ^{40}K respectively, from all countertop samples studied. Of all samples, the activity concentration due to ^{238}U in the Namib Green and African Red samples is of concern. High levels of uranium may increase the levels of radon (^{222}Rn) which is a decay product within the series. The big disequilibrium shown in Table 4.3 for these two samples implies that considerable radon gas will be released. Radon and its daughters are a significant health risk [BEIR VI, 1999]

In Table 4.5, the average values of the activity concentration of ^{226}Ra , ^{232}Th and ^{40}K are compared with the corresponding values measured in other countries and the average values of natural radionuclides in earth's crust. From Table 4.8, it can be concluded that the activity concentration levels of ^{226}Ra , ^{232}Th and ^{40}K measured in granite countertops from various locations in the world have varying ranges. The mean activity level values of ^{238}U , ^{232}Th and ^{40}K in the SC granite countertop is comparable to the values obtained in Brazil. Furthermore, the mean activity values of ^{238}U and ^{232}Th in the SC sample are comparable to the Earth crust average values, while the average value ^{40}K is 4 times higher than the Earth crust average value of 420 Bq/kg.

Table 4.5: Average values of the activity concentrations of ^{226}Ra , ^{232}Th and ^{40}K in granite samples from the different countries and earth crust.

Country	Activity concentrations (Bq/kg)			References
	^{226}Ra	^{232}Th	^{40}K	
Brasil	31	73	1648	Anjos (2005)
China	88	114	1270	Xinwei (2006)
Egypt	56	54	4849	El-Arabi (2007)
Greece	64	81	104	Pavlidou (2006)
USA	57	69	1140	Kitto (2009)
Pakistan	659	598	1203	Asghar (2008)
Turkey (Sivrilhisar)	67**	153	1058	Orgun (2005)
Turkey (Ezine)	175	205	1172	Orgun (2007)
Earth crust average	32	45	420	UNSCEAR (2000)
European Union	60	60	640	EC (1999)
Worldwide	42**	73	1055	Kitto (2009)
This study				
SC	19	48	1550	
NG	570	95	1960	
AR	131	147	1550	
GB	6	163	1920	
ID	< MDA	91	1450	

4.5 Assessment of radiation dose

Assessment of radiation dose received by users is calculated to evaluate the radiological health hazards. Radiological hazards associated with ^{238}U , ^{232}Th , and ^{40}K arise mainly from the external exposure to gamma radiation emitted from the granite countertops. The external absorbed dose rate (nGy/h) received by a user due to gamma exposure can be estimated using Equation 4.6.

4.5.1 Radium equivalent activity

Due to a non-uniform distribution of natural radionuclides in the granite countertop tiles, the actual activity level of ^{226}Ra , ^{232}Th and ^{40}K in the samples can be evaluated by

means of a common radiological index called the radium equivalent activity (Ra_{eq}) [Beretka, 1985]. It is the most widely used index to assess the radiation hazards and can be calculated using Equation 4.3 given by Beretka (1985). This estimates that 370 Bq/kg of ^{226}Ra , 259 Bq/kg of ^{232}Th and 4810 Bq/kg of ^{40}K produce the same gamma-ray dose rate [Kurnaz, 2007; Al-Hamarneh, 2009]. It has been reported that specific dose rates depends to a large degree on wall thickness and density but not on position in the room and dimensions of the room [Koblinger, 1984; Risica, 2001]. To assess the radiological risk of the building and/or decorating materials used, it is useful to calculate the Ra_{eq} [Papadopoulos, 2010]:

$$Ra_{eq} = A_{Ra} + (1.43 \times A_{Th}) + (0.077 \times A_K) \quad (4.3)$$

where A_{Ra} , A_{Th} and A_K are the activity concentrations of ^{226}Ra , ^{232}Th and ^{40}K , respectively. The calculated values of the radium equivalent activity for the studied granite countertops are given in Table 4.6. The permissible value of the Ra_{eq} activity is 370 Bq/kg which corresponds to an effective dose of 1 mSv for the general public [Ajayi, 2009].

4.5.2 External hazard index

A number of indices related to the evaluation of the external exposure to gamma radiation arising from building materials have been proposed by several investigators [Righi, 2006, Turhan, 2012]. To limit the radiation exposure attribution to natural radionuclides in the samples to the permissible dose equivalent limit of 1 mSv/y, the external hazard index based on a criterion have been introduced using a model by Krieger (1981) which is given by [Koblinger, 1984; Risica, 2001]:

$$H_{ex} = \frac{A_{Ra}}{370} + \frac{A_{Th}}{259} + \frac{A_K}{4810} \leq 1 \quad (4.4)$$

In order to keep the radiation hazard negligible, the value of H_{ex} must not exceed the limit of unity. The maximum value of H_{ex} equal to unity corresponds to the upper limit of radium equivalent activity (370 Bq/kg) [Dragovic, 2006; Nada, 2009].

4.5.3 Internal hazard index

In addition to the external hazard, the internal hazard exposure to radon and its daughter products is quantified by the internal hazard index (H_{in}) given by [Papadopoulos, 2010]:

$$H_{in} = \frac{A_{Ra}}{185} + \frac{A_{Th}}{259} + \frac{A_K}{4810} \leq 1 \quad (4.5)$$

For the safe use of a material in the construction of dwellings, H_{in} should be less than unity [Mohamed, 2015]. The calculated values of the internal hazard index for the studied granite samples are given in Table 4.6.

4.5.4 Absorbed dose rate

A direct connection between radioactivity concentrations of natural radionuclides and their exposure is known as the absorbed dose rate in the air at 1 metre above the ground. In order to assess any radiological hazard, the absorbed dose rate in indoor air due to gamma-ray emission from activity of ^{226}Ra , ^{232}Th and ^{40}K were calculated using [Mohamed, 2015; Papadopoulos, 2010]:

$$D = 0.92 A_{Ra} + 1.1 A_{Th} + 0.08 A_K \quad (4.6)$$

where D is the absorbed dose rate (nGy/h), A_{Ra} , A_{Th} and A_K are the activity concentrations of ^{226}Ra , ^{232}Th and ^{40}K , respectively. The estimated results for absorbed dose rate are given in Table 4.6.

Table 4.6: The values of the $R_{a_{eq}}$, the H_{ex} , the H_{in} and the absorbed dose rate (D) evaluated for the samples of the granite countertops.

Sample	$R_{a_{eq}}$ (Bq/kg)	H_{ex}	H_{in}	D (nGy/h)
SC	207 ± 4	0.56 ± 0.07	0.61 ± 0.08	194 ± 4
NG	860 ± 40	2.3 ± 0.2	3.9 ± 0.3	790 ± 30
AR	460 ± 9	1.2 ± 0.1	1.6 ± 0.1	406 ± 9
GB	387 ± 5	1.1 ± 0.4	1.1 ± 0.4	339 ± 5
ID	247 ± 4	0.7 ± 0.2	0.7 ± 0.2	221 ± 4

However these calculations are based on the assumption that all building materials are made of granite countertops. A more realistic estimate is presented by Llope (2011).

4.5.5 Effective dose

The absorbed dose rate does in air does not directly provide the radiological risk to which an individual is exposed [Jibiri, 2007]. In order to estimate the indoor annual effective dose, the conversion coefficient from absorbed dose in air to effective dose and

the indoor occupancy factor must be taken into account. By adopting similar technique from UNSCEAR 1993 and 2000 reports [UNSCEAR, 1993; UNSCEAR, 2000], the Committee used 0.7 Sv/Gy for the conversion coefficient from absorbed dose in air to effective dose exposure by adults and 0.8 for the indoor occupancy factor. The indoor annual effective dose is given by the expression:

$$E_D(\text{mSv}) = D (\text{nGy/h}) \times 8760 \text{ h} \times 0.8 \times 0.7 \text{ Sv/Gy} \times 10^{-6} \quad (4.7)$$

where E_D is the indoor annual effective dose (mSv), D is the absorbed dose rate (nGy/h) of each sample. The estimated results for indoor annual effective dose are given in Table 4.7.

Annual effective dose exposure determined by the indoors external terrestrial radiation component from the granite is summarized in Table 4.7. UNSCEAR (2010) determined the average worldwide exposure by adding the components of cosmic radiation, external terrestrial radiation, inhalation exposure and ingestion exposure. According to this report, the worldwide average annual exposure to natural radiation sources would generally be expected to be in the range 1 – 10 mSv, with 2.4 mSv being the present estimate of the mean.

Table 4.7: Estimated indoor annual effective dose E_D (mSv), calculated from the corresponding absorbed dose rate D (nGy/h).

Sample	D (nGy/h)	E_D (mSv)
SC	194	0.95
NG	788	3.9
AR	406	2.0
GB	339	1.7
ID	221	1.1

4.6 Assessment of radiological hazards

In addition to the radioactivity levels found in the granite countertop samples, it was also important to determine their effect in terms of health hazard. The radiological parameters can be evaluated from the measured activity levels of the 3 primordial radionuclides (^{238}U , ^{232}Th and ^{40}K) in granite countertops by using relations described in Section 4.5. Table 4.6 presents estimated values of these radiological parameters in

this study. The radium equivalent activity (Ra_{eq}) levels vary from 207 – 860 Bq/kg with a permissible value of 370 Bq/kg being considered safe, i.e. to reach the allowed maximum effective dose level for member of public at 1 mSv per year.



Chapter 5

SUMMARY AND OUTLOOK

5.1 Introduction

This chapter presents a summary of the findings found in this study and a conclusion is drawn with regard to the research questions stated in the first chapter. Recommendations and an outlook are discussed as well in this chapter.

5.2 Summary

Five granite countertop samples were radiometrically analysed using low-background high resolution gamma-ray spectrometry. The activity concentration levels in each sample was determined and used to assess their health risk to the public.

The range of the activity concentrations of ^{238}U , ^{232}Th , and ^{40}K varies from about 3 – 610 Bq/kg, 50 – 170 Bq/kg and 1400 – 2000 Bq/kg, respectively. From the results obtained, it can be observed that ^{238}U exhibits higher values of activity concentration compared with ^{232}Th which may be due to the relatively higher mobility of ^{238}U progenies i.e. ^{226}Ra compared to ^{232}Th [Talavera, 2000]. The activity concentrations of ^{40}K measured was noticeably higher when compared to the activity concentrations of ^{238}U and ^{232}Th in all the samples. Figure 4.13, 4.14 and 4.15 displays comparison between the specific activity level distribution of ^{238}U , ^{232}Th , and ^{40}K in the investigated countertops.

Most of the measured activity levels of ^{238}U , ^{232}Th , and ^{40}K found in some samples were higher than the world average values of 40 Bq/kg for ^{238}U , 40 Bq/kg for ^{232}Th , and 370 Bq/kg for ^{40}K (high in all samples) [UNSCEAR, 2000]. Using γ -ray spectrometry, most values were more than the permissible value 370 Bq/kg of Ra_{eq} , which is acceptable as a safe limit [OECD, 1979].

Countertops with radioactivity levels less than the permissible value of 370 Bq/kg (Ra_{eq}) are considered acceptable from a radiation hazard point of view, but concentrations above the limit could require intervention. Until very recently it was generally accepted that only 5% of the indoor radon concentration was due to building materials [Lao, 1990]. It is believed, in general, construction materials do not show alarming radioactive levels [Papaefthmiou, 2008; Damla, 2011]. However, the same

cannot be said about some of the granites. Allen et al. [Allen, 2010] studied the exhalation rate of granite countertops reporting a higher dispersion. These authors mention that the use of small granite specimens does not allow for extrapolations concerning the exhalation rate of the countertops. Other studies [Sahoo, 2011] criticize previous estimation on radon exhalation rate made on construction materials specimens, because they under estimate, by as much as 7 times, the exhalation rate of the material when used in a wall.

Radon constitutes the second most important cause of lung cancer in the general population, the first being smoking. In the past, it was accepted that only radon activity levels above 400 Bq/m³ could constitute a health risk, however, recent epidemiological findings demonstrate lung cancer risk from exposure to indoor radon at levels in the order of 100 Bq/m³ [Pacheco-Torgal, 2012]. The radiological hazard to humans due to the radioactivity arising from radionuclides contained in granite countertops was assessed. The estimated absorbed dose rates range from 194 to 790 nGy/h. These nuclides: ²²⁶Ra, ²³²Th and ⁴⁰K contribute approximately 44%, 52% and 4%, respectively, of the total absorbed dose rate in all measured granite countertops. The radium equivalent activity (Ra_{eq}) levels varies from 207 to 860 Bq/kg with the safety limit value of 370 Bq/kg recommended by OECD (1979). In addition, the calculated values of H_{ex} and H_{in} implies that some samples (SC and ID) are within the radiological risks limits of unity or less.

Moreover, estimates are made both nationally and internationally, of the sources and distribution of radiation exposures of populations. According to the latest periodic review of radiation exposures by the UNSCEAR (2010), reference individuals receive an average of approximately 3 mSv effective dose annually. But within a population, there may be a broad range of distinct personal exposures varying from below 1 mSv to a few tens of mSv. For each person, the absolute and relative contributions of different sources of radiation exposure will depend on many factors [McColl, 2015]. Factors include; home location (e.g. radon and cosmic ray exposure), exposure to radiotherapy, workplace exposure, ingestion of radionuclides, etc.

Figure 5.1 shows the pie chart of the annual average dose to the representative individual from different radiation sources. The chart also indicates that most of the radiation exposure of a typical individual comes from the natural radiation sources.

These sources include, the internal exposure from inhaling radon decay products when indoors, the external exposure from γ -emitting radionuclides in rocks, soil and building materials, and as well as internal exposure from ingestion of natural radionuclides, e.g. food and drinks [UNSCEAR, 2010].

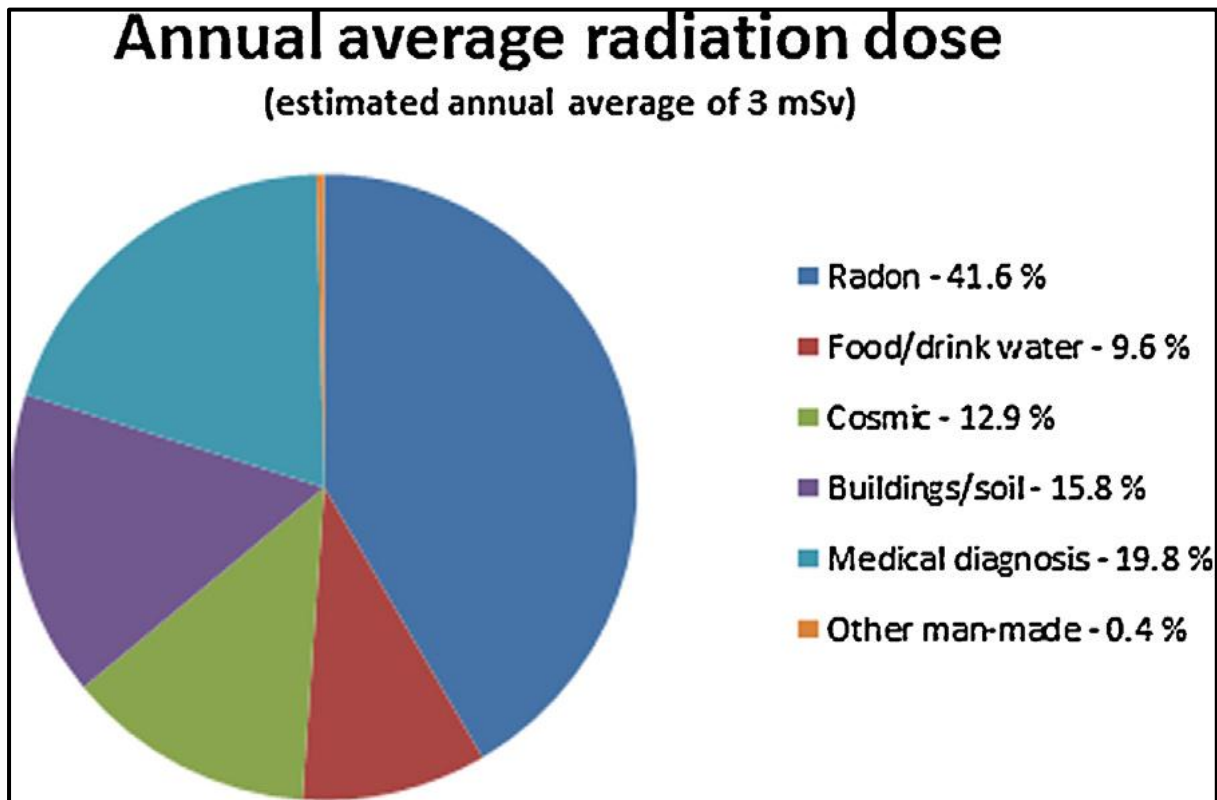


Figure 5.1: Components of the worldwide annual average individual radiation dose. The pie chart shows the annual average dose to the representative individual from the different radiation sources [McColl, 2015].

The evaluations on the Table 4.7 of exposures from natural radiation sources indicate that the annual effective dose is in the range of 0.95 – 3.9 mSv. The UNSCEAR (2010) report has indicated that the average annual effective dose to the world population is approximately 2.4 mSv, which is the same as the previous estimate of the Committee [UNSCEAR, 1993]. According to this report, for certain individuals, annual exposures ranging from 1 mSv to 3 times the world average were frequently encountered. It is estimated that about 65% of individuals have exposures between 1 and 3 mSv, about 25% of the population have exposures below 1 mSv and 10% have exposures above 3 mSv.

It can be concluded that the use of the: SC, AR, GB and ID granite countertop samples under investigation in the construction of dwellings are considered to be safe for inhabitants when the only source of exposure in these samples is external terrestrial radiation (indoors). Any individual under this exposure could be at risk, taking into account other exposures like cosmic radiation, inhalation exposure and ingestion exposure. However, some samples particularly AR needs to be further investigated for ^{222}Rn escape as it shows disequilibrium (see Table 4.3).

5.3 Outlook

Prior to measurements, more especially in the determination of ^{238}U activity concentration, it is recommended that the granite samples should also be thoroughly tested for secular equilibrium, i.e. sealed in a container and left for about 30 days before counting.

Attempts to enhance the analysis procedures are in progress. To improve the counting statistics, a 24 hour measuring time is recommended. In addition, an automatic program for peak detection of multi-overlapped peaks is needed to improve the peak area analysis in the spectrum. Thus, a benchmark based on the analysis of the selectivity of the signal is required to automatically select the most efficient deconvolution procedure for each state.

Considering exposure to environmental ionising radiation, inhalation of naturally occurring radon is the major source of radiation in the population [McColl, 2015]. Exposures to radon in buildings can be reduced by a three step process discussed by McColl (2015), namely; identifying those with potentially elevated radon levels, measuring radon levels, and reducing exposure by installation of remediation systems. In the 4th Edition of the European Code against Cancer, it is recommended: “Find out if you are exposed to radiation from naturally high radon levels in your home. Take action to reduce high radon levels”.

This work has laid a foundation for information on the activity concentrations of natural occurring nuclides in various granite countertops. These results have provided a good estimate of the radionuclides that are present in the granite countertops. There is an on-going effort for a future study to determine annual effective dose equivalent from

various granite countertops. One other option that could be explored, which involves 'transforming' the granite rock into a powder like sample, then use the available Marinelli geometries for counting, i.e. destructive method. Also for the radon and thoron (^{222}Rn and ^{220}Rn) determination, direct measurement could also be explored for this kind of building materials. Further ongoing work aims to utilize Monte Carlo simulations to determine corrections to coincidence summing in uranium and thorium decay chains for the HPGe detector system available at iThemba LABS.



APPENDICES

A. References

- Abbas, M. (2001). HPGe detector photo-peak efficiency calculation including self-absorption and coincidence corrections for Marinelli beaker sources using compact analytical expressions. *Applied Radiation and Isotopes* 54, 791.
- Ajayi, O. S. (2009). "Measurement of Activity Concentrations of K-40, Ra-40 and Th-232 for Assessment of Radiation Hazards from Soils of the Southwestern Region of Nigeria", *Radiation and Environmental Biophysics* 48, 323-332.
- Al-Hamarneh, I. F., & Awadallah, M. I. (2009). "Soil Radioactivity Levels and Radiation Hazards Assessment in the Highlands of Northern Jordan", *Radiation Measurements* 44, 457-465.
- Allen, J. G., Minegishi, T., McCarthy, W. B., Stewart, J. H., Macintosh, D. L., & McCarthy, J. F. (2009). Assessing exposure to granite countertops-part 1: Radon. *Journal of Exposure Science and Environmental Epidemiology*; doi.1038/jes.2009.43.
- Allen, J., Minegishi, T., Myatt, T., Stewart, J., McCarthy, J., & MacIntosh, D. (2010). Assessing exposure to granite countertops part 2: radon. *Journal of Exposure Science and Environmental Epidemiology*. 20:263-72.
- Allisy, A. (1996). "Henri Becquerel: The discovery of radioactivity", *Becquerel's Legacy: A Century of Radioactivity. Proceedings of a Conference, London: Nuclear Technology Publishing*, pp. 3-10.
- Anjos, R. M., Veiga, R., Soares, T., Santos, A. M., Aguiar, J. G., Frasca, M. H., et al. (2005). "Natural radionuclide distribution in Brazilian commercial granites", *Radiation Measurements* 39, 245-253.
- ANSI. (1999). American National Standard Institute. Calibration and use of germanium spectrometry for the measurements of gamma-ray Emission Rates of Radionuclides. ANSI-N42.14.
- Asghar, M., Tufail, M., Sabiha-Javied, Abid, A., & Waqas, M. (2008). Radiological implications of granite of Northern Pakistan. *Journal of Radiological Protection* 28, 387-399.
- Be, M. M. (2004). Table of radionuclides. Monographie MIPM-5.
- BEIR, V. (1999). BEIR VI (Committee on Health Risks of Exposure to Radon). Health Effects of Exposure to Radon: BEIR VI (Free Executive Summary). <http://www.nap.edu/catalog/5499.html>. National Research Council.
- Beretka, J., & Mathew, P. J. (1985). "Natural Radioactivity of Australian Building Materials, Industrial Waste and By-products", *Health Physics* 48, 87-95.
- Bohicchio, F. (2011). The newest international trend about regulation of indoor radon. *Radiation Protection Dosimetry*; 146:2-5.
- Chu, T. C., & Wang, J. J. (1997). Radioactive disequilibrium of uranium and thorium nuclide series in river waters from the Ta-Tun volcanic group area in Taiwan. *Applied Radiation and Isotopes* 48, 1149-1155.

- Cooke, M. S., Evans, M. D., Dizdaroglu, M., & Lunec, J. (2003). Oxidative DNA damage: mechanisms, mutation, and disease. *The FASEB Journal*, vol. 17 no. 10 1195-1214.
- Damla, N., Cevik, U., Kobya, A., Celik, A., Celik, N., & Yildirim, I. (2011). Assessment of natural radioactivity and mass attenuation coefficients of brick and roofing tile used in Turkey. *Radiation Measurements*. 46:701-8.
- Debertin, K. H. (1988). Gamma-ray and X-ray spectrometry with semiconductor detectors. North-Holland, 258-270.
- Debertin, K., & Jianping, R. (1989). Measurements of the activity of the radioactive samples in Marinelli beakers. *Nuclear Instruments and Methods in Physics Research, A* 275, 541.
- Dinua, A., Cosma, C., Sainz, C., Poncelab, L., & Vasilinius, S. (2009). Lung cancer attributable to indoor radon exposures in two radon - Prone areas, Stei (Romania) and Torrelodones (Spain). *Physics Conference, TIM-08; Timisoara, Romania. AIP Conf Proc.* 1131:175-80.
- Dragovic, S., Jankovic, L., & Onjia, A. (2006). "Assessment of Gamma Dose Rate Terrestrial Exposure in Serbia and Montenegro", *Radiation Protection Dosimetry* 121 (3), 297-302.
- EC. (1999). Radiological protection principles concerning the natural radioactivity of building materials, Directorate-General Environment, Nuclear Safety and Civil Protection. *Radiation Protection* 112.
- Eduardo, G. T. (2005). Monte Carlo calculations of coincidence summing corrections for volume sources in gamma-ray spectrometry with Ge detectors. *Nuclear Instruments and Methods in Physics Research A* 544, 577-583.
- El-Arabi, A. M. (2007). Ra-226, Th-232 and K-40 concentration in igneous rocks from eastern desert, Egypt and its radiological implications. *Radiation Measurements* 42, 94-100.
- ERSSFOPH. (2005). Environmental Radioactivity Section Swiss Federal Office of Public Health. Annual report.
- Evans, R. D. (1955). *The Atomic Nucleus*, Massachurets Institute of Technology. New York: McGraw-Hill. Inc.
- Firestone, R. B. (1996). *Table of Isotopes* (8th Ed). New York: John Wiley & Sons, Inc.
- Flakus, F. N. (1981). "Detecting and Measuring Ionizing Radiation - a Short History," *IAEA Bulletin*, VOL 23, NO 4.
- Fujiyoshi, R., Satake, Y., & Sumiyoshi, T. (2009). Depth profile of potassium and its isotope ratio (K-40/K) in several forest soils. *Journal of Radioanalytical and Nuclear Chemistry*, 281(3): 553-561.
- Gilmore, G. R. (2008). *Practical gamma-ray spectrometry*. England: John Wiley & Sons, Ltd.
- Guelland, K., Hagedorn, F., Smittenberg, R. H., Goransson, H., Bernasconi, S. M., Hajdas, I., et al. (2013). Evolution of Carbon fluxes during initial soil formation along the forefield of Damma glacier, Switzerland. *Biogeochemistry* 113: 545-561.
- Hendricks, P. (2003). In-depth gamma-ray studies - Borehole measurement.
- Hlatshwayo, I. N. (2007). In-situ gamma-ray mapping of environmental radioactivity at iThemba LABS and associated risk assessment. MSc Thesis, University of Zululand, South Africa.


- Holmgren, O., & Arvela, H. (2012). Assessment of current techniques used for reduction of indoor radon concentration in existing and new houses in European countries. STUK, A251. Helsinki, Finland: Radiation and Nuclear Safety Authority-STUK.
- Iwanczyk, J. S., Tull, C. R., MacDonald, L. R., Bescher, E., Robson, S. R., Mackenzie, J. D., et al. (2000). New LSO Based Scintillators. IEEE Transactions on Nuclear Science, VOL. 47, NO. 6.
- Jibiri, N. N., Farai, I. P., & Alausa, S. K. (2007). Estimation of Annual Effective Dose due to Natural Radioactive Elements in Ingestion of Foodstuffs in Tin Mining Areas of Jos-Plateau, Nigeria. *Journal of Environmental Radioactivity* 94, 31-40.
- Kastalsky, A., Luryi, S., & Spivak, B. (2006). Semiconductor high-energy radiation scintillation detector.
- Kirkup, L. (1994). *Experimental Methods. An Introduction to the Analysis and Presentation of Data*. John Wiley & Sons Australia, Ltd.
- Kitto, M. E., Haines, D. K., & Menia, T. A. (2009). Assessment of gamma-ray emissions from natural and manmade decorative stones. *Journal of Radioanalytical and Nuclear Chemistry* 282, 409-413.
- Knoll, G. F. (2000). *Radiation Detection and Measurement*, 3rd edition, John Wiley & Sons, Inc.
- Knoll, G. F. (2010). *Radiation Detection and Measurement*, 4th edition, John Wiley & Sons, Inc.
- Koblinger, L. (1984). Mathematical models of external gamma radiation and congruence of measurements. *Radiation Protection Dosimetry* 7, 227-234.
- Krane, K. S. (1988). *Introductory Nuclear Physics*. John Wiley & Sons, Inc.
- Krieger, R. (1981). "Radioactivity of Construction Materials", *Betonwerk Fertigteil Tech* 47, 468-473.
- Kurnaz, A., Kucukomeroglu, B., Keser, R., Okumusoglu, N. T., Kprkmaz, F., G, K., et al. (2007). "Determination of Radioactivity Levels and Hazards of Soil and Sediment Samples in Firtina Valley (Rize, Turkey)", *Applied Radiation and Isotopes* 65, 1281-1289.
- Lao, K. (1990). *Controlling indoor radon*. New York: Van Nostrand Reinhold.
- Lapp, R. E., & Andrews, H. L. (1972). *Nuclear Radiation Physics*. New Jersey: Prentice - Hall. Inc.
- Lee, M., Park, T. S., & Woo, J.-K. (2008). Coincidence summing effects in gamma-ray spectrometry using a Marinelli beaker. *Applied Radiation and Isotopes*. 66, 799-803.
- Leo, W. R. (1987). *Techniques for Nuclear and Particle Physics Experiments*. New York: Springer-Verlag.
- Llope, W. J. (2011). Activity concentrations and dose rates from decorative granite countertop. *Journal of Environmental Radioactivity*. 102, 620-629.
- Lobo, V., Patil, A., Phatak, A., & Chandra, N. (2010). Free radicals, antioxidants and functional foods: Impact on human health. *Pharmacogn Rev*:4(8): 118-126.
- Maleka, P. P., & Newman, R. T. (2012). Report on radiometric analyses of iThemba LABS liquid standard sources.

- McCull, N., Auvinen, A., Kesminiene, A., Espina, C., Erdmann, F., De Vries, E., et al. (2015). European Code against Cancer 4th Edition: Ionising and non-ionising radiation and cancer. *Cancer Epidemiology*.
- Mitchell, N., Perz-Sanchez, D., & Thorne, M. C. (2013). A review of the behaviour of U-238 series radionuclides in soils and plants. *Journal of Radiological Protection*. 33, R17-R48.
- Mohamed, R. I., Algamdi, S. K., & Al-shamani, N. S. (2015). Evaluation of radionuclide concentrations and associated radiological hazard in marble indices and granite used as building materials in Al-Madinah Al-Munawarah. *Journal of Taibah University for Science: JTUSCI-170*.
- Myatt, T. A., Allen, J. G., Minegishi, T., McCarthy, W. B., Stewart, J. H., Macintosh, D. L., et al. (2009). Assessment exposure to granite countertops-part 1: Radiation. *Journal of Exposure Science and Environmental Epidemiology*; doi.1038/jes.44, 1-8.
- Nada, A., Maksoud, T. M., Hosnia, M. A., El-Nagar, T., & Awad, S. (2009). "Distribution of Radionuclides in Soil Samples from a Petrified Wood Forest in El-Qattamia, Cairo, Egypt", *Applied Radiation and Isotopes* 67, 643-649.
- Newman, R. T., Lindsay, R., Maphoto, K. P., Mlwilo, N. A., Mohanty, A. K., Roux, D. G., et al. (2008). Determination of soil, sand and ore primordial radionuclide concentrations by full-spectrum analyses of high-purity germanium detector spectra. *Applied Radiation and Isotopes*.
- OECD. (1979). Organization for Economic Cooperation and Development, "Exposure to Radiation from the Natural Radioactivity in Building Materials". Paris, France: Report by a Group of Experts of the OECD Nuclear Energy Agency, OECD.
- Ongori, J. N. (2013). In-situ measurements and calculation of radon gas concentration and exhalation from a tailings mine dump. PhD Thesis, University of the Western Cape, South Africa.
- Orgun, Y., Altinsoy, N., Gultekin, A. H., Karahan, G., & Celebi, N. (2005). "Natural radioactivity levels in granitic plutons and groundwaters in Southeast part of Eskisehir. Turkey", *Applied Radiation and Isotopes* 63 (2), 267-275.
- Orgun, Y., Altinsoy, N., Sahin, S. Y., Gungor, Y., Gultenkin, A. H., Karahan, G., et al. (2007). "Natural and anthropogenic radionuclides in rocks and beach sands from Ezine region (Canakkale), Western Anatolia. Turkey", *Applied Radiation and Isotopes* 65, 739-747.
- Pacheco-Torgal, F., & Jalali, S. (2011). Toxicity of building materials. A key issue in sustainable construction. *Int J Sustain Eng Taylor Francis*; 4:281-7.
- Papadopoulos, A., Christofides, G., Papastefanou, C., Koroneos, A., & Stoulos, S. (2010). Radioactivity of Granite Rocks from Northern Greece.
- Papaefthmiou, H., & Gouseti, O. (2008). Natural radioactivity and associated radiation hazards in building materials used in Peloponnese, Greece. *Radiation Measurements*. 43:1453-7.
- Pavlidou, S., Koroneos, A., Papastefanou, C., Christofides, G., Stoulos, S., & Vavelides, M. (2006). "Natural radioactivity of granites used as building materials", *Journal of Environmental Radioactivity* 89, 48-60.
- Plagnard, J., Hamon, C., & Lepy, M. C. (2008). Study of scattering effects in low energy gamma-ray spectrometry. *Applied Radiation and Isotopes*. 66, 769-773.

- Raynaud, X., & Nunan, N. (2014). Spatial Ecology of Bacteria at the Microscale in Soil. *PLOS One*. 9(1): e87217.
- Righi, S., & Bruzzi, L. (2006). "Natural radioactivity and radon exhalation in building materials used in Italian dwellings", *Journal of Environmental Radioactivity* 88, 158-170.
- Risica, S., Bolzan, C., & Nuccetelli, C. (2001). Radioactivity in building materials: room model analysis and experimental methods. *The Science of the Total Environment* 272, 119-126.
- Sahoo, B., Sapra, B., Gaware, J., Kanse, S., & Mayya, Y. (2011). A model to predict radon exhalation from walls to indoor air based on the exhalation from building material samples. *Science Total Environment*. 409:2635-41.
- Shapiro, J. (2002). *Radiation Protection - A Guide for Scientists, Regulators, and Physicians*, vol. 4th edition. Cambridge, MA: Harvard University Press.
- Sima, O., & Arnold, D. (2008). A tool for processing decay scheme data that encompasses coincidence summing calculations. *Applied Radiation and Isotopes*. 66, 705-710.
- Smith, K., Smith, G., & Thiry, Y. (2010). Key issues in Biosphere Aspects of Assessment of the Long-term Impact of Contaminant Releases Associated with Radioactivity Waste Management. *BIOPROTA-WORKSHOP REPORT - VERSION 2.0*.
- Svec, A. (2008). Analytical efficiency curve for coaxial germanium detectors. *Applied Radiation and Isotopes*. 66, 786-791.
- Talavera, M. G. (2000). Coincidence summing corrections for the natural decay series in gamma-ray spectrometry. *Applied Radiation and Isotopes*.
- Talha, S. A. (2009). Measurements and application of radon in South Africa aquifer and river waters. PhD Thesis, University of the Western Cape, South Africa.
- Talha, S. A., de Meijer, R. J., Lindsay, R., Newman, R. T., Maleka, P. P., & Hlatshwayo, I. N. (2010). In-field radon measurement in water: a novel approach. *Journal of Environmental Radioactivity*. 101, 1024-1031.
- Talha, S. A., Lindsay, R., Newman, R. T., de Meijer, R. J., Maleka, P. P., Hlatshwayo, I. N., et al. (2008). Gamma-ray spectrometry of radon in water and the role of radon to representatively sample aquifers. (Proceedings of IAEA International Conference on Environmental Radioactivity, 23-27 April 2007, Vienna, Austria).
- Tavernier, S. (2010). *Experiment Techniques in Nuclear Physics Experiments*. Berlin Heidelberg: Springer-Verlag.
- Tso, M. Y., & Leung, J. K. (2000). "Population Dose Due to Natural Radiations in Hong Kong", *Health Physics* 8, 555-78.
- Tsoufanidis, N. (2010). *Measurement and detection of radiation*, 3rd edition. New York: McGraw-Hill.
- Turhan, S. (2012). "Estimation of possible radiological hazards from natural radioactivity in commercially-utilized ornamental and countertops granite tiles", *Annals of Nuclear Energy* 44, 31-39.
- Tzortzis, M., Tsertos, H., Christofides, S., & Christodoulides, G. (2003). Gamma radiation measurements and dose rates in commercially-used natural tiling rocks (granites). *Journal of Environmental Radioactivity*. 70, 223-235.

- UNSCEAR. (1993). United Nations. Sources and Effects of Ionizing Radiation. United Nations Scientific Committee on the Effects of Atomic Radiation, Report to the General Assembly, with scientific annexes. United Nations, New York: United Nations sales publication E.94.IX.2.
- UNSCEAR. (2000). (United Nations Scientific Committee on the Effects of Atomic Radiation). New York: Report to the General Assembly United Nations.
- UNSCEAR. (2008). United Nations Scientific Committee on the Effects of Atomic Radiation. UNSCEAR 2006 Report: Source and Effects of Ionizing Radiation. Report to the General Assembly with scientific annexes. New York: United Nations.
- UNSCEAR. (2010). United Nations Scientific Committee on the Effects of Atomic Radiation. UNSCEAR Report: Summary of low-dose radiation effects on health. Report to General Assembly and a Scientific Report. New York: United Nations.
- Veloso, B., Nogueira, J. R., & Cardoso, M. F. (2012). Lung cancer and indoor radon exposure in the north of Portugal - an ecological study. *Cancer Epidemiol*; 36(1):e26-32.
- Vidmar, T., Aubineau, -L. I., Anagnostakis, M. J., Arnold, D., Brettner-Messler, R., Budjas, D., et al. (2008). An intercomparison of Monte Carlo codes used in gamma-ray spectrometry. *Applied Radiation and Isotopes*. 66, 764-768.
- Vukanac, I., Djurasevic, M., Kandic, A., Novkovic, D., Nadjerdj, L., & Milosevic, Z. (2008). Experimental determination of the HPGe spectrometer efficiency curve. *Applied Radiation and Isotopes*. 66, 792-795.
- WHO. (2009). WHO handbook on indoor radon: a public health perspective. Geneva 27, Switzerland: World Health Organization.
- Xinwei, L., Lingqing, W., & Xiaodan, J. (2006). "Radiometric analysis of Chinese commercial granites", *Journal of Radioanalytic and Nuclear Chemistry* 267 (3), 669-673.
- Zaid, H. (2006). Quantitative Analysis in Nuclear Medicine Imaging. PhD Thesis, Geneva University Hospital, Switzerland.
- Zhao, H., Poon, C. S., & Ling, T. C. (2013). Utilizing recycled cathode ray tube funnel glass sand as river sand replacement in the high-density concrete. *Journal of Cleaner Production* 51 184-190.

B. Certified reference

 **CSIR**
NATIONAL METROLOGY
LABORATORY (NML)

National Metrology Laboratory

Radioactivity Standards Laboratory
CSIR-NML
15 Lower Hope Road, Rosbank 7700, Cape Town
☎ (021) 686 2759 / 685 7776 • fax (021) 686 2759

CERTIFICATE RS02-2

Mixed Volume Source

ISSUED TO:
Mr. J. van Rooyen
Radiation Safety Officer
iThemba LABS

DESCRIPTION:

One litre solution of ^{152}Eu , ^{137}Cs and ^{60}Co in 0.1 M HCl in a 1 L Marinelli beaker.

<u>Radionuclide</u>	<u>Activity</u>	<u>Uncertainty (1σ)</u>
^{152}Eu	6.550 kBq (0.177 μCi)	± 3.0 %
^{137}Cs	0.661 kBq (0.018 μCi)	± 2.0 %
^{60}Co	1.907 kBq (0.052 μCi)	± 2.0 %

REFERENCE DATE: 14 January 2002

HALF-LIFE:
 ^{152}Eu : 13.506 years
 ^{137}Cs : 30.018 years
 ^{60}Co : 5.271 years

METHOD OF MEASUREMENT:
Activity determined gravimetrically based on earlier measured values for the solutions used. Measurements against a calibrated pressurised ionisation chamber confirmed these values. Additionally ^{60}Co cross checked by a new absolute measurement using 4πβ-γ liquid scintillation coincidence counting, with agreement to better than 1%. The final volume source was measured by gamma spectroscopy with a NaI detector to corroborate the relative activities.

PREPARED BY: *W M Morris* **CHECKED BY:** *B R S Simpson*
W M Morris B R S Simpson

CERTIFICATE VOID IF SOURCE OPENED

Figure B.1: Certificate of 1L solution of ^{152}Eu , ^{137}Cs and ^{60}Co in 0.1 M HCL in a 1L Marinelli beaker received at iThemba LABS from CSIR.

PREPARATION OF A 1 LITRE MIXED RADIONUCLIDE VOLUME SOURCE

1. METHOD OF PREPARATION

An acid solution of 0.07 M HCl was prepared to which a small quantity of sodium benzoate was added as an anti-bacterial agent. Aliquots of available standardized stock solutions of ¹⁵²Eu, ¹³⁷Cs and ⁶⁰Co were each dispensed into the acidic solution and the activity was determined gravimetrically. The mixed radionuclide solution was solidified by adding HySorb 7150M from BASF Aktiengesellschaft. The mixed radionuclide solid source was packed into the Marinelli beaker up to the 1 litre mark.

The results of the measurements are traceable to the relevant national measurement standards.

2. DESCRIPTION

One litre of polymer-based material (acidity 0.07 M HCl) containing absorbed solutions of ¹⁵²Eu, ¹³⁷Cs and ⁶⁰Co in a 1.3 litre Marinelli beaker.

The Marinelli beaker had the following number written on it: S06A-19

Radionuclide	Activity	Uncertainty (1σ)	Reference Date
¹⁵² Eu	6.470 kBq (0.175 μCi)	± 0.181 kBq	20 Oct. 2010, 12h00 SAST
¹³⁷ Cs	0.817 kBq (0.017 μCi)	± 0.018 kBq	20 Oct. 2010, 12h00 SAST
⁶⁰ Co	1.859 kBq (0.050 μCi)	± 0.052 kBq	20 Oct. 2010, 12h00 SAST

3. REMARKS

- 3.1 The reported uncertainties of measurement were calculated and expressed in accordance with the BIPM, IEC, ISO, IUPAP, OIML document entitled 'A Guide to the Expression of Uncertainty in Measurement' (International Organisation for Standardisation, Geneva, Switzerland, 1993).
- 3.2 The reported uncertainty of measurement is stated as the standard uncertainty of measurement multiplied by a coverage factor of k = 1, which for a normal distribution approximates a level of confidence of 68.27 %.
- 3.3 Certain of the NMISA certificates are consistent with the capabilities that are included in appendix C of the MRA (Mutual Recognition Arrangement) drawn up by the CIPM. Under the MRA, all participating institutes recognise the validity of each other's calibration and measurement certificates for the quantities and ranges and measurement uncertainties specified in Appendix C. For details see <http://www.bipm.org>.
- 3.4 Measurements were carried out at an ambient temperature of 19 °C ± 3 °C and relative humidity of 57 %RH ± 15 %RH.

-----end of certificate-----

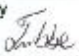


Measured by  J. Lubbe (Technical Signatory) Metrologist (Radioactivity)	Checked by  M. van Staden (Technical Signatory) Metrologist (Radioactivity)	For Chief Executive Officer 
Date of issue 22 October 2010	Page 2 of 2	Certificate number RS10-08

Figure B.2: Certificate of 1L polymer-based material of ¹⁵²Eu, ¹³⁷Cs and ⁶⁰Co in 0.07 M HCL in a 1.3L Marinelli beaker received at iThemba LABS from NMISA.

C. Spectrum analysis

The spectra observed from background and sample measurements were acquired using the Atomki-Palmtop program. The regions and centroids for all gamma-ray peaks in each spectrum were analysed using this program. The currently existing background spectrum was subtracted from the radionuclides available in the measured sample spectrum. To minimize variation, the effect in the background level was measured as close as possible to the time of the sample measurements. The counting spectra of the HPGe detector are shown in the Figure C.1 and C.2. According to the results of the experiments, the obtained counts in the NG detection spectrum were higher than those in the SC detection spectrum. Figure C.1 shows the high count rate spectrum of NG and Figure C.2 shows the low count rate spectrum of SC. In addition, the obvious difference between the spectra of NG and SC in the figures below implies that the activity levels of the two samples should be different.

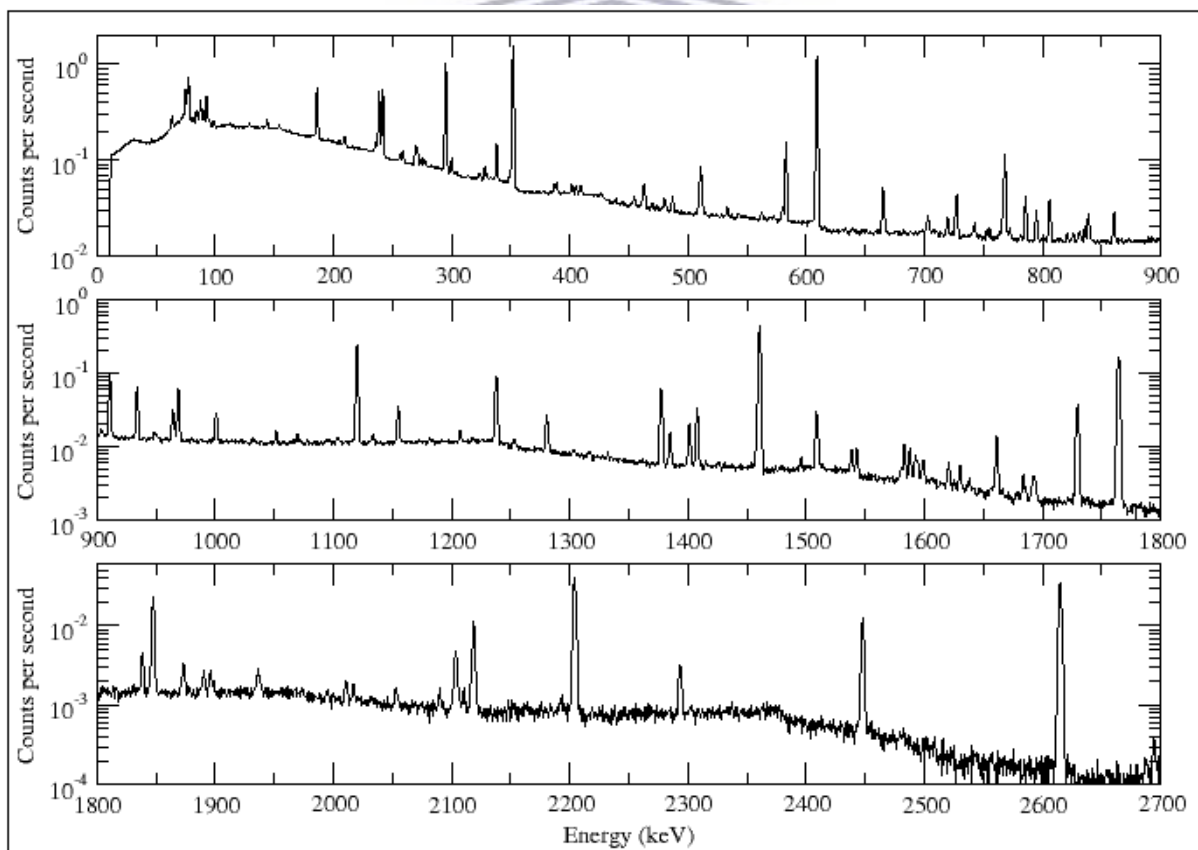


Figure C.1: Detail of spectrum obtained from sample NG, a mixture of ^{238}U , ^{232}Th and ^{40}K in the energy range of 0 to 2700 keV.

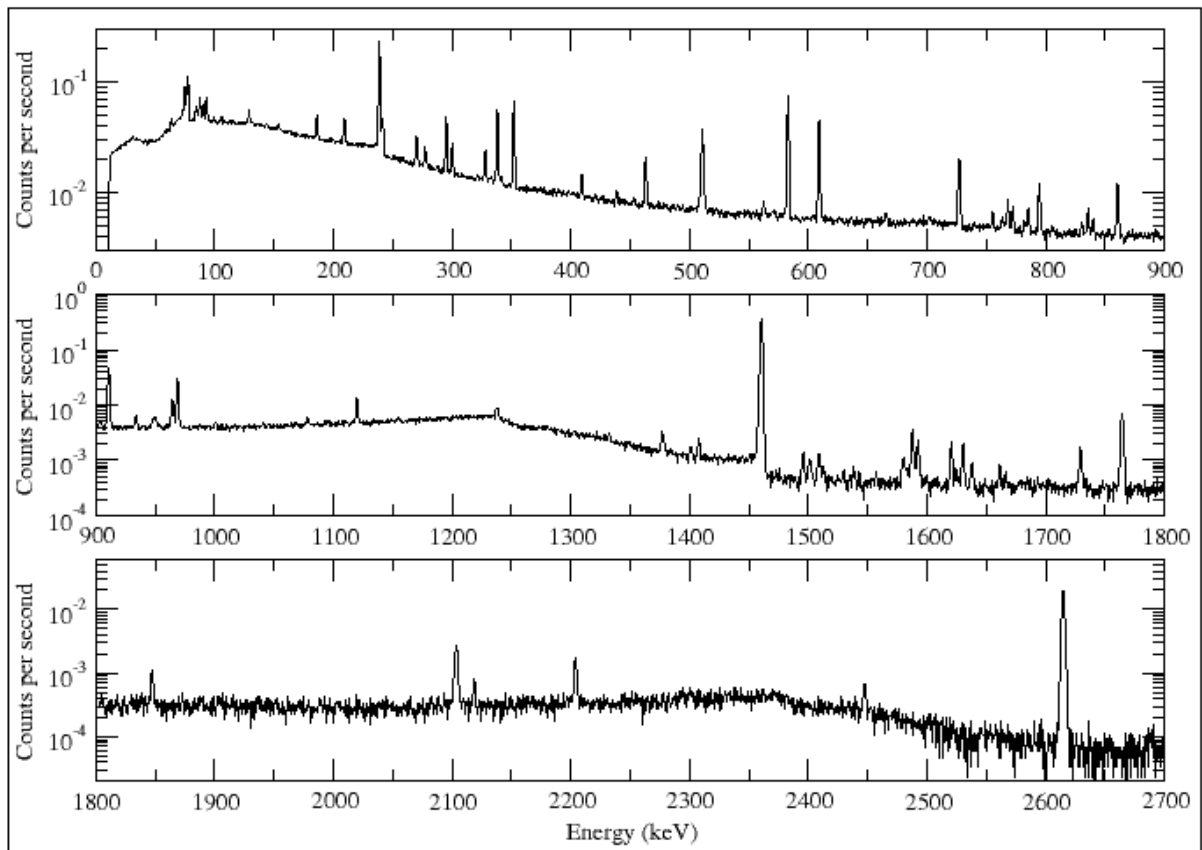
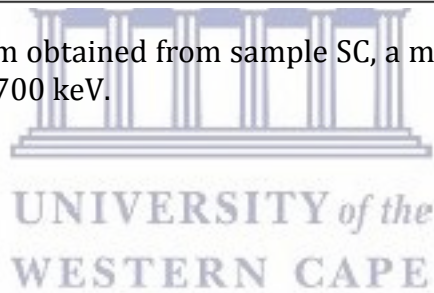


Figure C.2: Detail of spectrum obtained from sample SC, a mixture of ^{238}U , ^{232}Th and ^{40}K in the energy range of 0 to 2700 keV.



D. List of symbols

Symbol	Name	Unit
A	Radioactivity	Bq
A_c	Activity concentration	Bq/kg or Bq/l
E	Energy	eV
m	Mass	kg
I	Number of transmitted γ -ray	—
I_0	Original beam intensity	—
N	Number of decays	—
r_0	Classical electron radius	m
t	Time	s
V	Volume	m ³
x	Thickness	m
Z	Atomic number	—
λ	Decay constant	s ⁻¹
ρ	Density	kg/m ³
μ	Linear attenuation coefficient	m ⁻¹
σ_c	Cross-section for Compton scattering	m ² /kg
σ_k	Cross-section for pair production	m ² /kg
σ_τ	Cross-section for photoelectric absorption	m ² /kg
θ	Scattering angle	Degrees (°)

UNIVERSITY of the
WESTERN CAPE